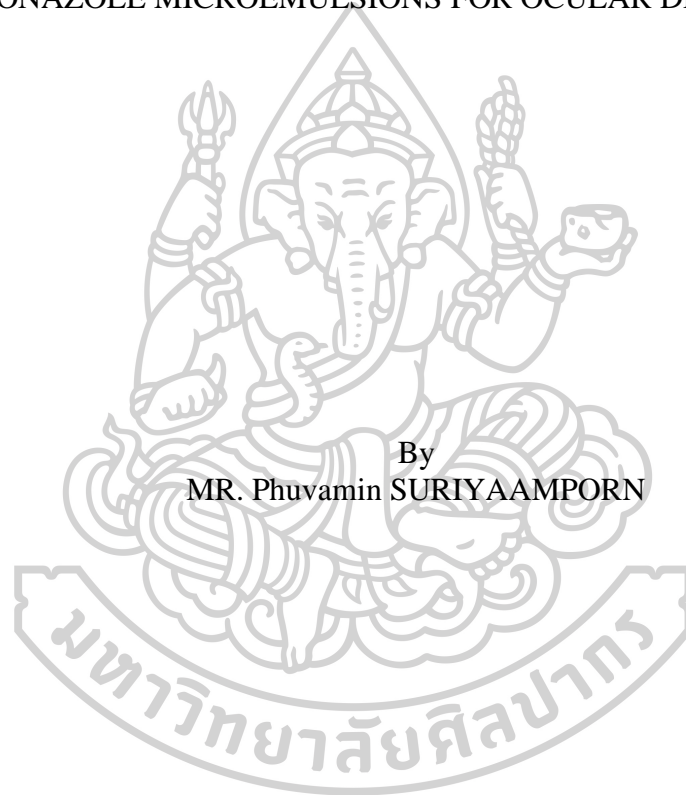DEVELOPMENT OF TWO-LAYER DISSOLVING MICRONEEDLES LOADING
FLUCONAZOLE MICROEMULSIONS FOR OCULAR DRUG DELIVERY

By

MR. Phuvamin SURIYAAMPORN

A Thesis Submitted in Partial Fulfillment of the Requirements
for Doctor of Philosophy PHARMACEUTICAL TECHNOLOGY
(INTERNATIONAL PROGRAM)
Department of PHARMACEUTICAL TECHNOLOGY
Silpakorn University
Academic Year 2022
Copyright of Silpakorn University

การพัฒนาไมโครนีเดิลส์ชนิดละลายแบบสองชั้นบรรจุยาฟลูโคนาโซลไมโครอิมัลชัน
สำหรับการนำส่งยาผ่านดวงตา

โดย
นายภูวมินทร์ สุริยาอัมพร

วิทยานิพนธ์นี้เป็นส่วนหนึ่งของการศึกษาตามหลักสูตรปรัชญาดุษฎีบัณฑิต
สาขาวิชาเทคโนโลยีเภสัชกรรม (หลักสูตรนานาชาติ) แบบ 1.2 ปรัชญาดุษฎีบัณฑิต
ภาควิชาเทคโนโลยีเภสัชกรรม
มหาวิทยาลัยศิลปากร
ปีการศึกษา 2565

DEVELOPMENT OF TWO-LAYER DISSOLVING MICRONEEDLES LOADING FLUCONAZOLE MICROEMULSIONS FOR OCULAR DRUG DELIVERY

By

MR. Phuvamin SURIYAAMPORN

A Thesis Submitted in Partial Fulfillment of the Requirements
for Doctor of Philosophy PHARMACEUTICAL TECHNOLOGY
(INTERNATIONAL PROGRAM)
Department of PHARMACEUTICAL TECHNOLOGY
Silpakorn University
Academic Year 2022
Copyright of Silpakorn University

Title	Development of two-layer dissolving microneedles loading fluconazole microemulsions for ocular drug delivery
By	MR. Phuvamin SURIYAAMPORN
Field of Study	PHARMACEUTICAL TECHNOLOGY (INTERNATIONAL PROGRAM)
Advisor	Professor TANASAIT NGAWHIRUNPAT, Ph.D.
Co advisor	Professor Praneet Opanasopit, Ph.D.

Faculty of Pharmacy, Silpakorn University in Partial Fulfillment of the Requirements for the Doctor of Philosophy

.... Dean of Faculty of
(Assistant Professor Surasit Lochidamnuay, Ph.D.)   Pharmacy

Approved by

.... Chair person
(Assistant Professor Worranan Rangsimawong, Ph.D.)

.... Advisor
(Professor TANASAIT NGAWHIRUNPAT, Ph.D.)

.... Co advisor
(Professor Praneet Opanasopit, Ph.D.)

.... Committee
(Associate Professor SUWANNEE PANOMSUK, Ph.D.)

.... Committee
(Assistant Professor Boonnada Pamornpathomkul, Ph.D.)

61353801 : Major PHARMACEUTICAL TECHNOLOGY (INTERNATIONAL PROGRAM)
Keyword : Two-layered dissolving microneedles, Microemulsion, Optimal mixture design, Fungal keratitis, Fluconazole

MR. Phuvamin SURIYAAMPORN : Development of two-layer dissolving microneedles loading fluconazole microemulsions for ocular drug delivery Thesis advisor : Professor TANASAIT NGAWHIRUNPAT, Ph.D.

Fungal keratitis is a serious issue that can lead to eye problems if not treated properly. Topical fluconazole (FLUZ) is commonly used for treating fungal infections in the eyes, but its limited solubility in water makes it difficult to treat deeper infections. Microemulsions (MEs) and microneedles (MNs) were used to enhance the solubility and bioavailability of FLUZ in order to improve its effectiveness. The study aimed to develop and evaluate the potential of MEs-FLUZ-loaded two-layered dissolving MNs for treating fungal keratitis. The optimal mixture of oil, surfactant, cosurfactant, and water was used to create MEs-FLUZ, which were then loaded into two-layered dissolving MNs. The MNs were evaluated for physical appearance, mechanical properties, penetration ability, dissolution time, *in vitro/ex vivo* ocular drug delivery, antifungal activity, and stability. The results showed that the MEs-FLUZ-loaded two-layered dissolving MNs effectively treated fungal keratitis with good physical properties, mechanical strength, insertion force, and penetration depth. The MNs formulation completely dissolved in corneal tissue within 3 min and demonstrated a significant permeation profile in MEs-FLUZ-loaded two-layered dissolving MNs higher than others. Furthermore, the antifungal activity of these MNs significantly inhibited fungal growth more than others. The MNs formulations were also found to be stable at 4-25 °C over 6 months. Therefore, the MEs-FLUZ-loaded two-layered dissolving MNs can be a minimally invasive treatment for fungal corneal infection.

ACKNOWLEDGEMENTS

TABLE OF CONTENTS

Page

LIST OF TABLES

LIST OF FIGURES

Page

LIST OF ABBREVIATIONS

2^k	Two-level full factorial design
3^k	Three-level full factorial design
ANOVA	Analysis of variance
BAB	Blood aqueous barrier
BC	Bruch's-choroid
°C	Degree Celsius
CCD	Central composite design
CFU	Colony forming unit
C_d	Donor concentration of the formulations
C_r	Receptor concentration of the formulations
CLSM	Confocal laser scanning microscope
cm^3	Cubic centimeter(s)
CO_2	Carbon dioxide
Da	Dalton
DAB	Droplet-born air blowing
DF	Dilution factor(s)
DOEs	Design of experiments
DMSO	Dimethyl sulfoxide
DLS	Dynamic light scattering
Eq.	Equation
et al.	*et alia* (Latin abbreviation of "andothers"; For references with more than two authors)
FDA	Food and Drug Administration
FLUZ	Fluconazole
h	Hour(s)
HCl	Hydrochloric acid
HA	Hyaluronic acid
i.e.	*id est* (Latin abbreviation); that is
J	Steady-state flux
KCl	Potassium chloride

kDa	Kilodalton
kg	Kilogram(s)
KH_2PO_4	Potassium dihydrogen orthophosphate
K_p	Permeability coefficient
K_d	Diffusion coefficient
log P	Log partition-coefficient
m^2	Square centimeter(s)
mg	Milligram(s)
min	Minute(s)
mL	Milliliter(s)
mm	Millimeter(s)
MNs	Microneedle(s)
MEs	Microemulsion(s)
MW	Molecular weight
N	Newton
NaCl	Sodium chloride
$NaHCO_3$	Sodium bicarbonate
NaOH	Sodium hydroxide
nm	Nanometer(s)
OD	Optical density
PBS	Phosphate buffered saline
PDMS	Polydimethylsiloxane
pH	Potential of hydrogen
Ph. Eur.	European Pharmacopoeia
PVP	Polyvinylpyrrolidone
PVA	Polyvinyl alcohol
RCE	Retinal capillary endothelial
rpm	Revolutions per minute
s	Second
SDA	Sabouraud dextrose agar
S_{mix}	Surfactant mixed with co-surfactant
SANS	Small angle neutron scattering

SAXS	Small angle X-ray scattering
USP	United States Pharmacopeia
WHO	World Health Organization
v/v	Volume by volume
w/w	Weight by weight
w/v	Weight by volume
w/o	water in oil
o/w	oil in water
μg	Microgram(s)
μL	Microliter(s)
μm	Micrometer(s)
%	Percentage(s)
®	Registered trademark
™	Trademark
T_{lag}	Lag time
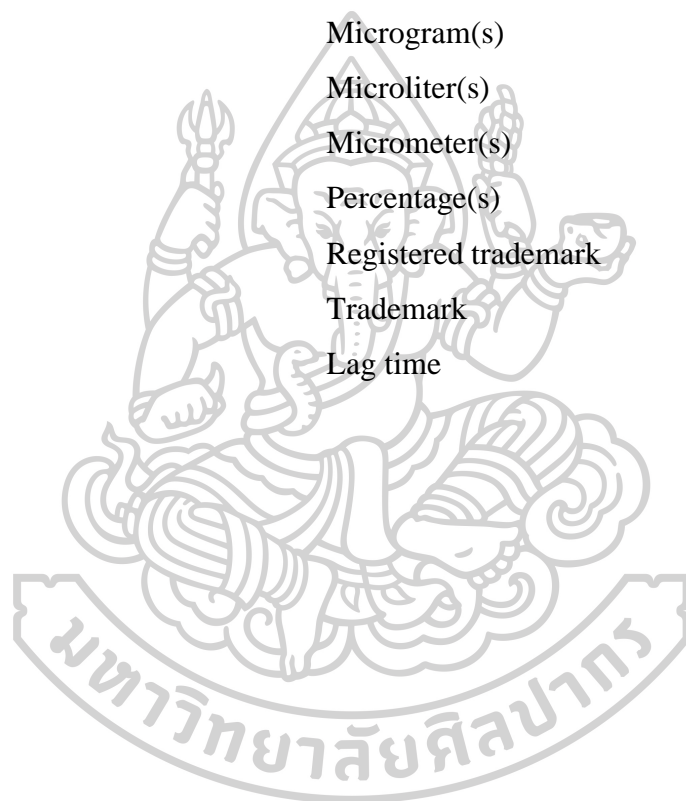
CHAPTER 1

INTRODUCTION

1.1 Statement and significance of the research problem

Fungal keratitis or fungal eye infections are a significant cause of ocular morbidity that can result in blindness if not properly treated. The United States healthcare system costs approximately $175 million annually to treat around 30,000 new cases (1). Risk factors for ocular fungal infections include ocular trauma, overuse or contamination of ocular products, immunocompromised diseases, and systemic fungal infections. Common sources of fungal keratitis are *Candida, Fusarium, Aspergillus, and Curvularia* (2). Pharmacological treatments for ocular fungal infections typically involve using antifungal drugs, such as natamycin, amphotericin B, econazole, fluconazole, itraconazole, miconazole, ketoconazole, and voriconazole. These drugs can be administered via ocular instillation, subconjunctival injection, or oral therapy (3).

Fluconazole (FLUZ) belongs to the azole group of antifungal drugs and is known as 2-(2,4-difluorophenyl)-1,3-bis(1H-1,2,4-triazol-1-yl)-2-propanol, is a lipophilic compound that has limited solubility in water. It has been widely used in clinical practice to treat fungal infections in the eye due to its favorable safety profile, high bioavailability, and broad-spectrum antifungal activity. Its mode of action involves disrupting the synthesis of ergosterol, which is critical for the fluidity and integrity of the fungal membrane and proliferation. The concentration of FLUZ typically used for topical treatment ranges from 0.18 to 0.9 %w/w (4-6), while the effective therapeutic dose for subconjunctival and intracorneal injection is approximately 0.2 %w/w (7, 8). However, antifungal drugs for the treatment of fungal eye infections or fungal keratitis have limitations, such as poor water solubility, poor water-lipid partition into the ocular barrier, and fungal depth infiltrations (9).

Diseases affecting the front part of the eye, such as fungal keratitis, are typically treated using eye drops. However, the effectiveness of medication administered through eye drops is limited by the corneal barrier, which reduces its bioavailability. The lipophilic corneal epithelium, which has tight junctions, is the first barrier that restricts the delivery of drugs to the eye (10). Additionally, the bioavailability of eye drops is further limited by the rapid turnover of lacrimal fluid, the blinking reflex, and the nasolacrimal drainage, resulting in a contact time with the eye surface of less than 5% (11, 12). To address this limitation, techniques such as frequent instillation, increasing drug concentration, improving contact time, or intracorneal injection can be employed, although these may decrease patient compliance and increase the risk of systemic or local side effects (13).

According to the solubility classification defined by USP and Ph. Eur., FLUZ has limited solubility in water but is highly soluble in oils and surfactants, suggesting that it could be formulated as a lipid-based delivery system (14). Lipid-based formulations, especially microemulsions, are a well-established alternative approach for the delivery of hydrophobic drugs. Microemulsions are isotropic systems composed of oils, surfactants, co-surfactants, and water. Oil-in-water microemulsions can be quickly and easily formed with gentle stirring. Microemulsions offer several benefits, including improved drug loading, increased bioavailability, and thermodynamic stability. Furthermore, microemulsions are suitable for ocular drug delivery because the small droplet size of the emulsion can enhance ocular drug bioavailability by prolonging drug release and/or improving drug penetration through the ocular tissues. Microemulsions are safe and biocompatible and have been successfully used to prepare formulations containing antifungal drugs, such as econazole, ofloxacin, prednisolone, timolol, and voriconazole, which exhibit better penetrability and provide effective pharmaceutical effects for the treatment of ocular diseases (15-20).

Microneedles (MNs) are the micron-scale technology (60 to 2000 μm in height) with minimally invasive ocular tissue. The mechanism of MNs on the ocular application can create aqueous conduits on the cornea and bypass the corneal barrier, improving the bioavailability of ophthalmic drugs. The MNs used in the ocular

application can be categorized into 5 types following their mechanism: [1] Solid MNs can create micropores on the ocular surface. After removal, the applied drug formulations can diffuse through the microchannels (21). [2] Drug-coated MNs are dissolved and diffused into the drug coating into the eye after MNs insertion (22). [3] Hollow MNs, the liquid drug formulations are infused by pressure-driven flow through a conduit into the target tissue, similar to hypodermic needles (23). [4] Dissolving MNs - the drugs are encapsulated into the polymeric MNs matrix and released the drug-polymer matrix into the target tissue, depending on the rate of polymer dissolution or degradation (24). [5] Hydrogel-forming MNs allow drug diffusion from a drug reservoir during the swollen polymeric matrix of the MNs (25). Moreover, the MNs can be divided following their material, including polymeric MNs (dissolving MNs) and non-polymeric MNs (solid, coated, and hollowed MNs) fabricated from steel, glass, and silicon.

Some disadvantages of non-polymeric MNs in the ocular application are difficulties in fabrication, lack of drug accuracy, applicability, and complication. Polymeric microneedles are fabricated from biocompatible or biodegradable polymers that are increasingly interesting in ocular drug delivery. Dissolving polymeric microneedles is safe, with minimal damage to ocular tissue, ocular damage healing within 24 h, and provided non-medical waste after complete dissolution (24). Furthermore, the dissolving MNs were completely dissolved faster than hydrogel-forming MNs. Specifically, several micro- or nanoparticle formulations have been used to incorporate into polymeric MNs to improve drug delivery, including liposome-amphotericin B loaded dissolving MNs (26), cubosome-rapamycin loaded dissolving MNs (27), nanosuspension-curcumin loaded dissolving MNs (28) and nanocrystals-itraconazole loaded dissolving MNs (29). The benefits of this combination could improve ocular disease therapy and enhance the drug's solubility and penetrability. Therefore, this study is to design and develop ME-FLUZ-loaded dissolving MNs for improving the treatment of fungal eye infections.

1.2 Aims and objectives

1.   To fabricate MEs-FLUZ-loaded two-layer dissolving MNs for ocular drug delivery

2.   To evaluate the physicochemical properties of MEs-FLUZ-loaded two-layer dissolving MNs and the ability to deliver the drug into and through the ocular tissue

3.   To determine the antifungal activity of MEs-FLUZ-loaded two-layer dissolving MNs for the treatment of fungal eye infection

1.3 The research hypothesis

1.   The optimal MEs-FLUZ formulation with appropriate size, size distribution, drug content, and ocular permeation can be used as the inner layer of two-layer dissolving MNs.

2.   The optimization of dissolving MNs successfully fabricated can provide the appropriate physical appearance and mechanical strength to use as the outer layer of two-layer dissolving MNs for ocular delivery.

3.   The fabrication of MEs-FLUZ-loaded two-layer dissolving MNs can improve the drug loading capacity, stability, and antifungal activity for treating fungal eye infections.

CHAPTER 2

LITERATURE REVIEW

2.1 Common ocular diseases and ocular drug delivery

Ocular drug delivery has been a major challenge for pharmaceutical scientists and ophthalmologists because the unique anatomy and physiology structure of the eye restricts the permeation of the drug. Visual impairment and blindness from ocular diseases are the most important concern to public health problems worldwide. The World Health Organization (WHO) reported visual problems in about 285 million people globally, which include 39 million vision blindness and 246 million decreased vision (30). The eye lens can divide the ocular disease into anterior segment disease and posterior disease. The most serious vision impairment affects the quality of life. Anterior segment diseases include corneal neovascularization (CNZ), bacterial keratitis, fungal keratitis, herpes simplex keratitis, uveitis, blepharitis, and glaucoma. While age-related macular degeneration (AMD), diabetic macular edema (DME), and cytomegalovirus retinitis (CMV) lead to permanent vision loss in the posterior segment of the eyes (31). The summary of ocular diseases, signs and symptoms, and current treatment is represented in Table 1 (32). Recently, ocular drug delivery systems can be generally classified into topical, injection, and systemic routes. Conventional ocular drug delivery systems (e.g., topical and systemic routes) have long been widely used for treating anterior segment diseases due to their non-invasive, painless, and convenient use. Nonetheless, these routes have low ocular drug bioavailability or sub-therapeutic drug level because of numerous anatomical and physiological of the eyes, such as multi-layer of ocular barrier, tear turnover, nasolachrymal drainage, and reflex blinking. That is necessarily required for high drug concentration and frequent use to reach therapeutic treatment; however, this is related to high side effects and toxicity. To improve the ocular drug bioavailability, injection routes that bypass the ocular barrier are applied either directly into the eye (intravitreal injection, IVT), the surrounding outer surface of the eye (periocular or transscleral route), or within the ocular tissues (intracorneal and intrascleral). The

global standard treatments for anterior and posterior segment diseases are intracorneal and intravitreal injections. Periocular that are less invasive than the above injection routes are still limited because of transient drug diffusion across the sclera-retinal barrier. The solubility of the drug, molecular weight/radius, charge, and polarity are important factors for the diffusion of drugs into the sclera-retinal barrier (33). Nevertheless, the injection method into the eyes using hypodermic needles causes patients discomfort and pain and requires a specialist for treatment. Moreover, the injection routes need a frequency and a long time for treatment that may increase severe ocular complications. Therefore, microneedles (MNs) that are minimally invasive techniques are used as a device for ocular drug delivery systems with appropriate precision and accuracy. MNs can delivery drug into the eye at local target specific site by bypassing ocular barriers. MNs are patient friendly because it is painless and patients can apply by themselves. The MNs for ocular drug delivery is a relatively new concept. However, to date, this MNs technology still has been limited in this area, unlike transdermal MN studies.

Table 1: Major ocular diseases, signs and symptoms, and current treatment.

Diseases	Classification	Sign and symptom	Treatment
Anterior segment			
- CNZ	-	Invasion of new blood vessels into the cornea	Anti-VEGF agents (Bevacizumab, Ranibizumab, and Aflibercept)
- Conjunctivitis - Keratitis - Uveitis	- Based on the structures and infection	Bacterial/ Fungal/ Viral infected conjunctiva, cornea, and uvea lead to redness, irritation, grittiness and watering of the eyes	Antibiotic/ Antifungal, Anti-inflammatory, Anti-histamine agents
- Glaucoma	- Primary open-angle	Ocular pressure increased from the	Prostaglandin analogs, Beta-adrenergic

glaucoma (POAG)		obstruction outflow of aqueous humor.	receptor antagonists, Alpha-2 adrenergic agonists, Parasympathomimetics, Carbonic anhydrase inhibitors
- Angle-closure glaucoma (ACG)			

Posterior segment

- AMD	- Dry AMD (non-exudative)	Breakdown of photoreceptors, retinal pigment epithelium (RPE)	High-dose formulation containing antioxidants, zinc, and vitamin supplements
	- Wet AMD (exudative)	Growth of abnormal blood vessels behind the retina and macula. Degeneration of RPE	Anti-VEGF agents (Ranibizumab, Pegaptanib sodium, and Bevacizumab)
- DME	- Focal or non-cystoid DME	Small aberrations in retinal blood vessels	Focal or grid lasers and steroids
	- Diffuse or cystoids DME	Formation of microcysts and dilation of retinal capillaries	-
- CMV	-	Viral infection leads to inflammation of the retina.	Antiviral agents (Cidofovir, Ganciclovir and Foscarnet)

2.2 Structure and barrier of eyes affected ocular drug delivery

The human eye is an important organ for the perception of vision. The dimension of the eye is about 23-24 mm with a volume of about 4-4.5 mL. The

human eye can be divided into anterior and posterior segments by the human lens, as represented in Figure 1.
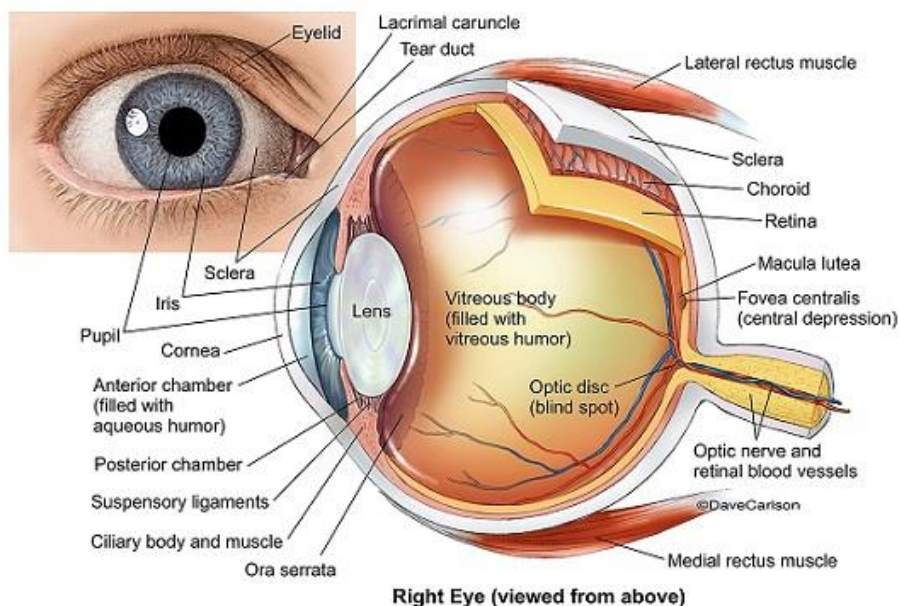
Figure 1: The structure of the human eye divided into anterior and posterior segments by the human's lens (34)

2.2.1 The anterior segment and important barrier function

2.2.1.1 Tear film: The outer surface of the eye is covered by a thin layer of tear film that reservoirs ocular tissue nourishment and protects foreign matter entered into the eye. The lacrimal fluid turnover that is the first obstacle to ocular drug delivery is about 1 μL/min *via* the nasolacrimal duct. Therefore, instillation eye drop formulations cleared from the eye's surface within minutes affected the drug's low bioavailability (< 1%). The thickness of this layer is about 3-10 μm (35).

2.2.1.2 Conjunctiva: The conjunctiva, a thin transparent mucous layer with a highly vascularized layer and mucous-secreting tissue, covers the cornea, the anterior surface of the sclera extended to the border of the corneal limbus and the inner surface of the eyelids. This layer generates the mucous to facilitate the movement of the eye and tear film adhesion. A highly vascularized layer and lymphatic system significantly affects drug loss into the systemic circulation, decreasing ocular drug bioavailability and increasing

unwanted systemic side effects. Moreover, a molecular weight of a drug >10 kDa is able to across this layer.

      2.2.1.3 Cornea: The human cornea, clear and transparent, is the first route for drug delivery into the eye. Moreover, it protects the entry of exogenous substances into the eye. The cornea represents the eyeball about 7% (1.3 cm^2) of the total surface area with 10.50-11.55 mm in dimension. The thickness at the middle region is about 0.52 mm and the limbus (the junction between the cornea and sclera) is about 0.67 mm (36). The cornea is not reached by blood vessels or nerve supply; therefore, it receives oxygen and nourishment from the tear film and aqueous humor. Typically, the human cornea is composed of importance five tissue layers such as epithelium, Bowman's membrane, stroma, Descemet's membrane, and endothelium, which affect the delivery of drug molecules into the eye, as shown in Figure 2.
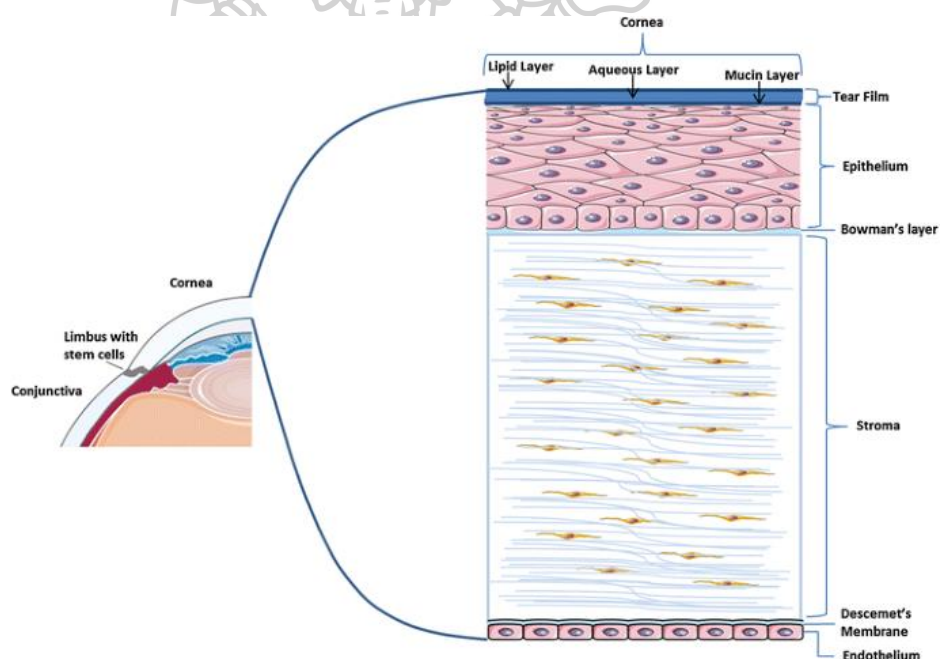
Figure 2: The structure of human corneal tissue that consists of five layers, namely epithelium, Bowman's membrane, stroma, Descemet's membrane, and endothelium (37)

- *Epithelium:* The corneal epithelium tissue is a non-keratinized stratified squamous epithelium with a thickness of about 50 µm. This layer forms 5-7 layers of flattened superficial cells, wing cells, and

single columnar basal cells. Zonula occludens (the tight junctions between the epithelium cell) prevent the permeation of low lipophilicity drugs and macromolecular properties. The paracellular pore diameter of epithelium is about 2.0 nm, resulting in difficulty in drug permeating into an anterior chamber (38). Suitable permeation drugs should have partition coefficients that are more than 1, a molecular weight less than 60-100 Da, or a molecular radius of 5.5 Å. The corneal permeability is also affected by the charge of the drug. Generally, the corneal surface is negatively charged with a 3.2 isoelectric point, so the anionic compound is easily entrapped in this layered (39). Therefore, the corneal epithelium is an important rate-limiting barrier (40, 41).

- *Bowman's membrane:* A thin acellular basement layer mainly composed of collagen fibrils. It is not a rate-limiting barrier for drug compounds.

- *Stroma:* The thickness of this layer is >90% of the cornea, which is about 500 µm. This layer mainly consists of an extracellular matrix such as collagen, keratocytes, and glycosaminoglycans. The biophysical of the stroma is a hydrophilic nature that affects lipophilic compounds in restricting the drug's permeation across this layer. Moreover, a molecular weight >50,000 Da is difficult to permeate this layer (42, 43).

- *Descemet's membrane:* A thin acellular collagen layer between the stroma and endothelium layers.

- *Endothelium:* It is a monolayer squamous epithelium that is the last membrane of the cornea with a thickness of about 5 µm. The biophysical of the endothelium are similar epithelium layer (lipophilicity nature), providing a hydrophilic compound across the endothelium. However, the junction between the cell of this layer is looser than epithelium, which affects a molecular weight <50,000 Da able to cross this layer. As a result, the permeation of endothelium is more than epithelium approximately 2.7 times (44).

2.2.1.4 Blood aqueous barrier (BAB): This barrier controls the conduit of aqueous humor between the anterior and posterior eye segments. Generally, the BAB presented the tight junction prevents the plasma protein or hydrophilic drug from systemic circulation into the aqueous humor. Furthermore, this barrier restricts the movement of drugs from the anterior to the posterior segment. Therefore, the efficient drug concentrations that reach the posterior segment are failed to treat ocular diseases by conventional topical and systemic formulation.

2.2.2 The posterior segment and important barrier function

2.2.2.1 Sclera: The sclera, called "white of the eye" is mechanical support and strength to the eye. The human sclera covers the outer surface of the eyeball approximately 80% or 16.3 cm^2, mainly consisting of extracellular matrix such as glycoproteins, elastin fibrils, and collagen fibrils (45). The sclera consists of four layers: Tenon's capsule, episclera, stroma, and lamina fusca from the outer to the inner side. The average thickness of the sclera is approximately 0.53 mm. The scleral tissue has an arrangement of collagen fibers and a concentration of proteoglycans less than the cornea tissues that affect the water content in tissues (i.e., 68% in the scleral tissue and 78% in the corneal tissue). Moreover, the scleral permeability is higher than corneal tissue due to a lack of the epithelium and endothelium layers. According to the high water content structure of the sclera, hydrophilic compounds with a high molecular weight of about 150 kDa can cross this layer. However, positively charged compounds have low permeability across sclera tissue because the negative charge of proteoglycans can attach to the compound and hinder their transport across sclera tissue. Figure 3 shows the structure of scleral tissue.
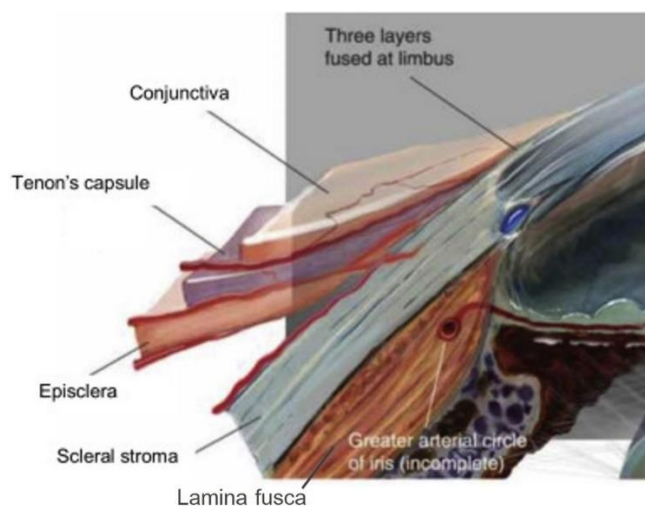
Figure 3: The structure of human scleral tissue that consists of four layers, namely Tenon`s capsule, episclera, stroma, and lamina fusca from the outer side into the inner side (46)

2.2.2.2 Choroid: The choroid that is the next layer beneath the sclera is a significant barrier for decreased drug bioavailability because it is composed of highly vascularized choroid tissue that plays a major role in supplying blood, oxygen, and nutrients to the retina. Bruch's membrane also functions as a barrier-like choroid with a thickness of about 2-4 µm. Therefore, Bruch's choroid (BC) complex located between the sclera and retinal pigment epithelium is the critical barrier to sclera drug delivery, decreasing drug bioavailability before reaching virtuous humor or retina. The lipophilic drugs with positively charged are entrapped and slowly released in the BC complex (47).

2.2.2.3 Retina and blood-retinal barrier (BRB): The retina is considered a site of action in the posterior segment of the eye. It is a thin and transparent tissue located next to the choroid. The inner limiting membrane of the retina, which is between the vitreous humor and the retina, acts as a significant barrier to drug penetration (48). The BRB is the main barrier of drug diffusion from the systemic circulation into the retina. This barrier comprises retinal capillary endothelial (RCE) cells that are tight junctions and

protect foreign substances from blood circulation into the retina. Therefore, the macromolecules with hydrophilic substances are unable to cross this layer.

As shown in Table 2, the physicochemical properties of ocular tissue caused the limitation of ocular drug delivery.

Table 2: Summary of physicochemical properties affecting permeation of ocular tissue.

Ocular tissue	Molecular size	Lipophilicity	Charge
Anterior segment			
- Cornea	Radius <5.5 Å or <MW 500Da	lipophilic molecules (log P 2 to 3)	(+) molecules
- Conjunctiva	Radius <5.5 Å or <MW 500Da	lipophilic molecules	No studied
- BAB	Radius <5.5 Å or <MW 500Da	lipophilic molecules	No studied
Posterior segment			
- Sclera	MW <150 kDa	hydrophilic molecules	(-) molecules
- BC complex	Radius <5.5 Å or <MW 500Da	hydrophilic molecules	(-) molecules
- BRB	Radius <5.5 Å or <MW 500Da	lipophilic molecules	No studied

2.3 Fungal keratitis

Fungal eye infections or fungal keratitis are the important problems that cause ocular morbidity. It is an infection of the cornea that may lead to blindness if it is not cured properly. The symptoms of fungal keratitis include eye redness, blurred vision, sensitivity to light, excessive tearing, and eye discharge. The important causes of fungal keratitis are ocular trauma, overuse and/or contamination of ocular products,

immunocompromised disease, and systemic fungal infections. In the United Kingdom, the important causative organisms are yeast species such as *Candida spp.* (57%) and filamentous fungal species such as *Aspergillus spp.* (17%) and *Fusarium spp.* (26%) (49, 50). The fungal infection probably starts when the epithelial integrity is broken due to trauma or ocular surface disease, and the organism gains access to the corneal tissue and proliferates. Proteolytic enzymes, fungal antigens, and toxins are released into the cornea, resulting in necrosis and damage to the integrity and function of the eye. Antifungal agents for fungal keratitis are ocular instillation, oral therapy, or subconjunctival injection. The common antifungal drugs are natamycin, amphotericin B, miconazole, econazole, ketoconazole, fluconazole, itraconazole, voriconazole and posaconazole (51).

2.4 Current ocular antifungal pharmacotherapy

2.4.1 Polyene antifungals

The mechanism of action of polyene antifungals is binding to ergosterol, an essential structural component of the fungal cell membrane, leading to a loss in the fungal cell integrity, increased cell permeability, and promoted oxidative action on the fungal cells (52). The mechanism of action is shown in Figure 4.
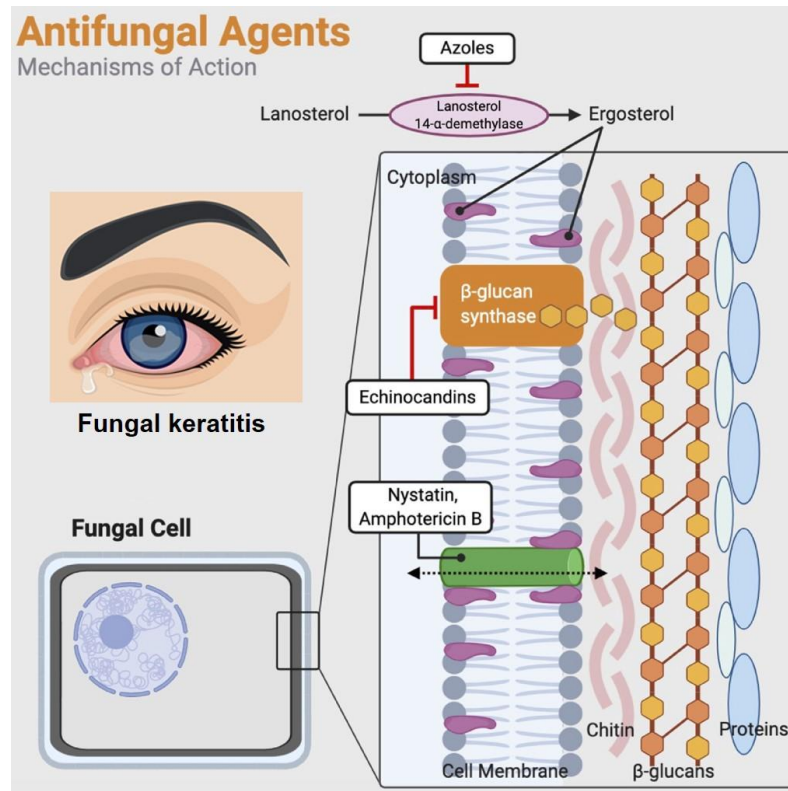
Figure 4: The mechanisms of action of antifungal drugs (53)

2.4.1.1 Natamycin

Natamycin is a long molecule with low water solubility, represented in Figure 5. In treating fungal keratitis, natamycin is the only US FDA-approved drug. However, the other polyene (amphotericin B), azole, and echinocandin antifungals have been routinely used in clinical treatment because of their potent and broad-spectrum antifungal activity. Moreover, fewer cases of resistance and cross-resistance are reported (3). However, natamycin is low bioavailability and not widely available in developing countries.
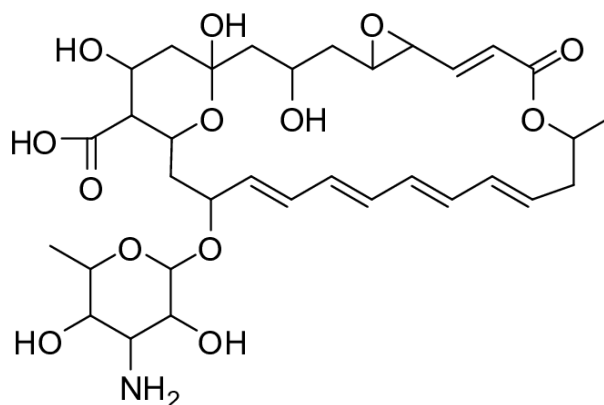
Figure 5: The structure of natamycin

2.4.1.2 Amphotericin B

Amphotericin B is used to treat systemic and localized fungal infections. It has a broad-spectrum antifungal agent; therefore, it has been used to treat ocular fungal infections as an off-label. However, the molecular weight of amphotericin B is high (924.08 g/mol), caused unable to penetrate the cornea resulting ineffective treatment, as represented in Figure 6. (54). Thus, intracorneal or intravenous administrations are recommended, which require a higher dose of the drug to reach the therapeutic dose resulting systemic toxicity such as nephrotoxicity (55).
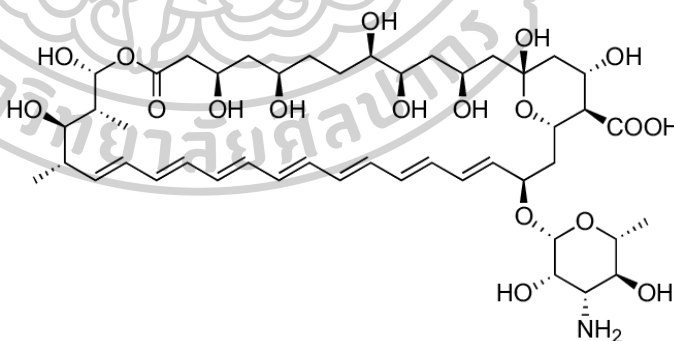
Figure 6: The structure of amphotericin B

2.4.2 Azole antifungals

The mechanism of action of azole antifungals blocks the fungal cytochrome P450 enzymes, affecting the synthesis of ergosterol in the cell membrane and inhibiting fungal growth. Azoles antifungal group is divided into two major classes such as imidazole (miconazole, econazole and

ketoconazole) and triazoles (fluconazole, itraconazole and voriconazole). The triazole group has the advantage in the slow metabolism of the drug less than the imidazole group (56). The mechanism of action is shown in Figure 4.

2.4.2.1 Fluconazole

FLUZ is the first generation of triazole. FLUZ is lipophilic and slightly soluble in water, effectively penetrating corneal tissue and reaching aqueous humor concentration (57), represented in Figure 7. It has found off-label clinical applications in ocular fungal infections. Moreover, FLUZ is less toxic than amphotericin B when used in single intracorneal or subconjunctival applications (58). Therefore, FLUZ, such as amphotericin B, has also found favor as an off-label agent in ocular antifungal pharmacotherapy.
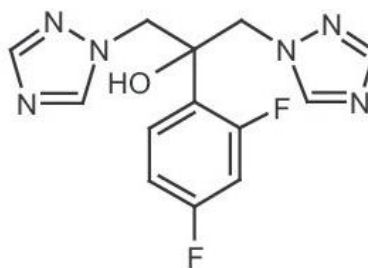
Figure 7: The structure of fluconazole (59)

2.4.2.2 Itraconazole

Itraconazole is the first generation of triazole. Itraconazole has been used to treat ocular keratitis in some countries because it has various side effects, such as convulsions, dry mouth, nausea, vomiting, dizziness, and irregular heartbeat. It has not been approved for ocular use by FDA due to clinically inconsistent data and low ocular effectiveness (60). Therefore, it is used only as an adjuvant of ocular antifungal pharmacotherapy in some rare cases (61). The structure is represented in Figure 8.
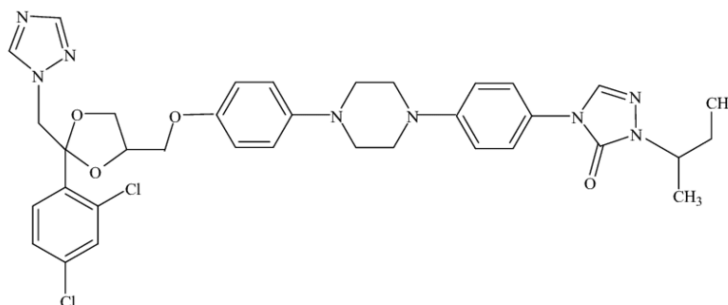
Figure 8: The structure of itraconazole (62)

2.4.2.3 Voriconazole

Voriconazole is a second generation of triazole that has been widely used off-label in treating fungal keratitis. It is more effective than the first generation due to selectively blocking the ergosterol synthesis (63). Voriconazole is developed from FLUZ and shows better efficacy than the first generation of triazole, with lower toxicity than amphotericin B. It is currently the drug of choice for treating fungal keratitis resistant to polyenes due to the high cost of drug therapy (64). The structure is represented in Figure 9.
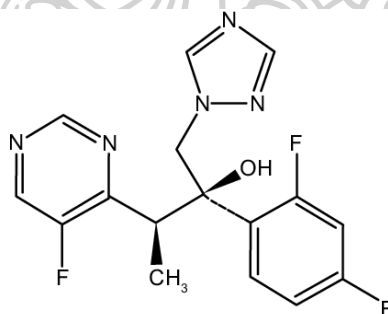
Figure 9: The structure of voriconazole (65)

2.4.2.4 Posaconazole

Similar to voriconazole, posaconazole is a second generation of triazole. It is developed from itraconazole and is only available as an oral solution. The data on posaconazole use in fungal keratitis is still limited (66, 67). The structure is represented in Figure 10.
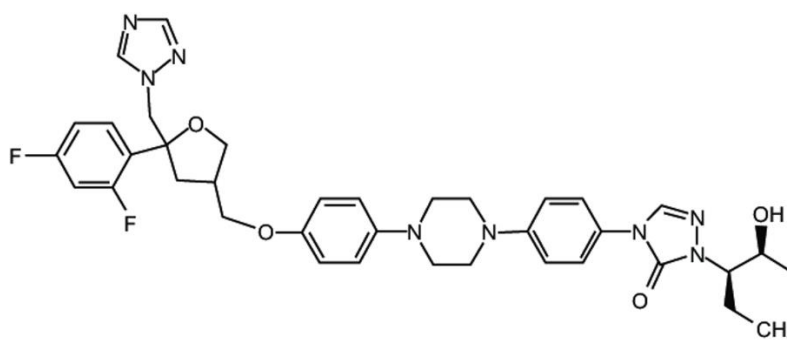
Figure 10: The structure of posaconazole (68)

2.4.3 Echinocandin antifungals

Echinocandin is a high molecular weight of semisynthetic lipopeptides antifungal drugs. The mechanism of action of echinocandin antifungals is inhibition of the β-(1,3)-D-glucan synthesis in the cell membrane, causing osmotic imbalance and cell lysis (69). The mechanism of action is shown in Figure 4.

2.4.3.1 Caspofungin

Caspofungin is the first to be approved to treat fungal keratitis. In a preclinical study, the efficacy of topical caspofungin drug for treating *Candida* keratitis was equivalent to amphotericin B (70). Moreover, intravitreal caspofungin treatment is effective and safe for deep ocular fungal infection (71). However, caspofungin has been used as an adjuvant individually due to the high cost of drug therapy. The structure is represented in Figure 11.
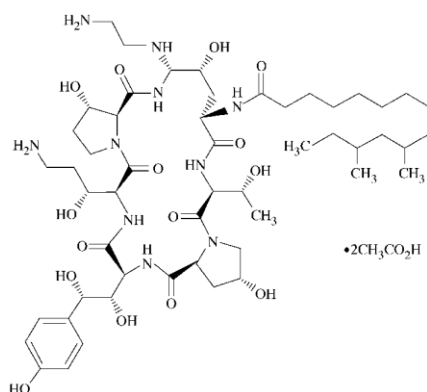
Figure 11: The structure of caspofungin (72)

2.4.3.2 Micafungin

Micafungin was also tested in the preclinical study as an alternative ocular antifungal drug. Topical micafungin showed efficacy and safety similar to topical natamycin in fungal keratitis treatment. Also, voriconazole and amphotericin B intravitreal injection effectively treated fungal keratitis. However, micafungin has still been evaluated in preclinical studies. The structure is represented in Figure 12.
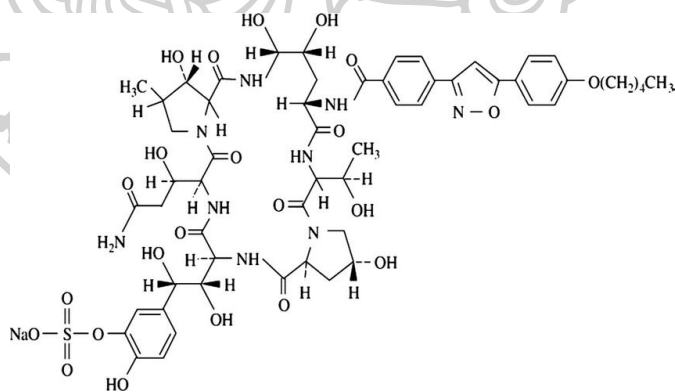
Figure 12: The structure of micafungin (73)

Table 3: Summary of the recent updates in ocular antifungal pharmacotherapy for the treatment of fungal keratitis

Drugs	Routes of administration	Dosing	Major limitations	Indications
Polyene antifungals				
- Natamycin	Topical	50 mg/mL	- Poor penetration - Low bioavailability	- First choice in the treatment of filamentous fungi
- Amphotericin B	Topical Intracorneal Intravitreal	1.5-5 mg/mL 5-10 µg/mL 1-10 µg/0.1mL	- Preparation and stability - Systemic toxicity	- First choice in the treatment of keratitis by yeasts
Azole antifungals				
- Fluconazole	Topical Subconjunctival Oral	2 mg/mL 2 mg/mL 200–400mg/day	- Narrow antifungal spectrum (Effective *Candida* species)	- Alternative to polyenes in the treatment of fungal keratitis
- Itraconazole	Oral	400mg/day	- Topical application low efficacy	- Deep fungal keratitis by yeasts
- Voriconazole	Topical Intracorneal	1 mg/mL 50 µg/0.1mL	- High cost - Topical application low efficacy than natamycin	- First-line of triazoles for fungal keratitis resistant to polyenes

Drugs	Routes of administration	Dosing	Major limitations	Indications
	Intravitreal	50 µg/0,1mL		
	Oral	200 mg q12h		
- Posaconazole	Topical	100 mg/mL	- High cost	- Adjunctive therapy in deep keratitis and resistance to polyenes
	Oral	400 mg q12h	- Limited data (preclinical study)	
Echinocandin antifungals				
- Caspofungin	Topical	1.5-5 mg/mL	Limited data (preclinical study)	- Fungal keratitis by yeasts resistant to polyenes
- Micafungin	Topical	1 mg/mL	Limited data (preclinical study)	- Fungal keratitis by yeasts resistant to polyenes

2.5 Current ocular drug delivery systems and administration routes

2.5.1 Topical routes

Topical applications, such as eye drops solutions, suspensions, emulsions, ointments, and gels, have been widely used for a long time because it is easy to self-administration to treat anterior segment disease with good patient compliance. However, the lacrimation, tear flow, blood flow, and ocular barrier can decrease drug bioavailability (<5%); therefore, frequent application of topical ophthalmic formulations is necessary to increase the bioavailability of the drug. Moreover, conventional topical ophthalmic formulations are still inefficient in treating posterior segment diseases due to ocular barriers (74). Therefore, novel micro-/nanotechnology for topical ophthalmic formulations have been developed in the last few decades, such as micro-/nanoemulsion, nanoparticles, nanosuspensions, nanomicelles, liposomes, and dendrimers can improve ocular bioavailability by changing the structure of ocular barrier or bypassed the ocular barrier through the cell junction with appropriate particle size. However, these novel ophthalmic formulations still have lower bioavailability than invasive methods (75).

2.5.2 Contact lenses

The drug-loaded contact lenses, thin and curved plastic disks designed to cover the cornea, have been developed to improve ocular drug delivery (76). Generally, the drug is loaded in contact lenses by soaking in the drug solution. After application, the drug in the contact lens is diffused for a long residence time on the cornea; therefore, it can improve the drug's permeation and reduce the drug's degradation into the nasolacrimal duct. As a result, the drug-loaded contact lenses showed higher delivery of drug efficacy into the eye than topical ophthalmic formulations (77).

2.5.3 Ocular implants

This ocular device is specifically designed to treat localized ocular disease. Moreover, this device can control or sustain drug release into specific ocular target sites due to the type of polymers fabricated from both

biodegradable and non-biodegradable polymers. The implantations of this device are invasive methods that need minor surgery for placing the device into intravitreous. Mostly, implantable devices have been used to treat chronic vitreoretinal diseases (78, 79).

2.5.4 Oral/Systemic route

The oral formulation is convenient and acceptable to patients; however, it is not the first choice to treat ocular disease because the BAB or BRB, the important ocular barrier, hinders the drug from getting into the anterior and posterior segments, respectively. Therefore, a large systemic dose is required to achieve therapeutic efficacy, which can affect significant systemic side effects. Moreover, the systemic route may decrease the drug bioavailability or therapeutic effect due to systemic first-pass metabolism (80).

2.5.5 Ocular injection route

The ocular injection routes directly inject the drug into the eye by bypassing the ocular barrier function of the eye. The injection routes can be divided into anterior and posterior injections according to injection techniques. Figure 13 shows anterior segment injections, such as subconjunctival, intrastromal, intracorneal, and intrascleral injections, and posterior segment injections, such as intravitreal injections (IVTs), and transscleral delivery (subtenon, peribulbar and retrobulbar). Each injection route of drug delivery facilitates a high concentration of drug within the injected tissue. The benefits of the ocular injection route are found in the emergency management of acute conditions, such as corneal neovascularization (CNZ), age-related macular degeneration (AMD), diabetic macular edema (DME), and cytomegalovirus retinitis (CMV). However, these methods may not be precise in dosing and are associated with numerous side effects, such as increased intraocular pressure (IOP), hemorrhage in the eye, pain after injection, and systemic adverse effects.

The summary of current ocular drug delivery systems and administration routes is represented in Figure 13 and Table 4.
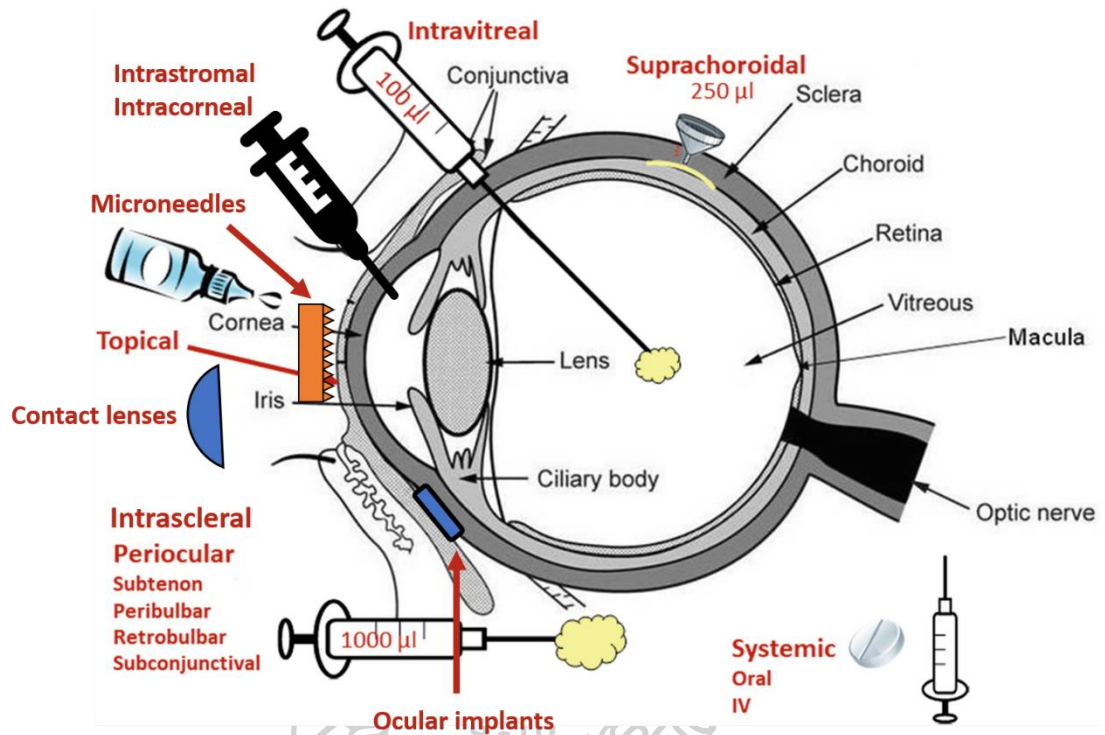
Figure 13: The routes of ocular drug delivery systems at an anterior segment and posterior segment of the eyes (81)
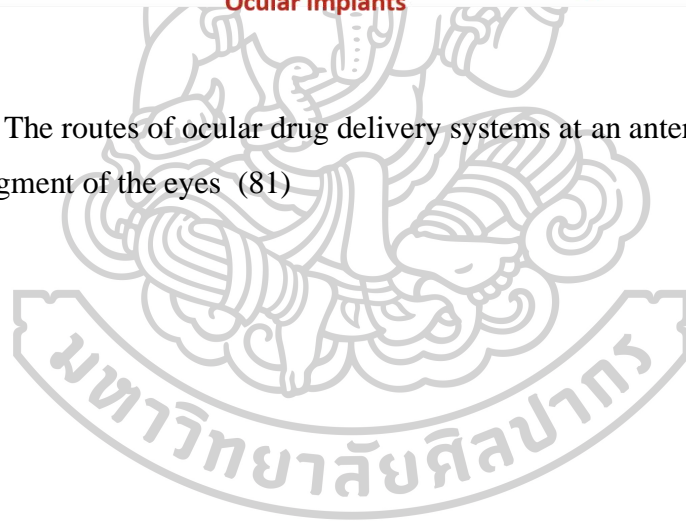
Table 4: Summary of current ocular drug delivery systems and administration routes

Lists	Topical	Contact lenses	Ocular implants	Oral/Systemic	Ocular injection	Microneedles
Description	Solutions, Suspensions, Emulsions, Ointments, Gels	Soaked drug plastic curved shape to cover the cornea	Implantations of the device in the eye	Oral dosage formulations	Stainless steel injection needle with shape tip	Micron-scale needle sizes are aligned on a small patch
Onset of action	Slow	Slow	Slow	Slow	Faster	Faster
Pain	Painless	Painless	Painful	Painless	Painful	Painless
Bioavailability	Poor	Poor	Insufficient	Insufficient	Sufficient	Sufficient
Patient compliance	Less	Less	Less	Better	Less	Better
Self-administration	Yes	Yes	No	Yes	No	Yes
Mechanism of drug delivery	Permeation through the ocular tissue barrier	Permeation through ocular tissue barrier with high contact time	Control release from polymer	Drug in blood circulation across through BAB or BRB	Drug injects directly into the ocular target site	Bypass ocular barrier and drug directly into the ocular target site, enhancing permeability.

2.6 Fundamental and principles of mathematical ocular permeation

Mathematical models of ocular permeability are important in many fields, such as predicting ocular drug delivery and assessing ocular membrane exposure to the environment. All drug compounds are across to the ocular membrane by a passive diffusion mechanism. This passive diffusion through the ocular membrane can be explained by Fick's laws of diffusion when the passive diffusion is in a steady state, which means independent with time. Therefore, Flux (J), the amount of drug that can diffuse through the membrane per time, can be calculated following Eq. 1.

$$J = -K_d \frac{dC}{dx} = \frac{dM}{Sdt} \qquad \text{Eq.1}$$

Where K_d is the diffusion coefficient, dC/dx is the concentration gradient, C is the concentration of drug compounds, x is the diffusion distance, M is the amount of drug in grams or mole, S is the surface area, and t is the time. The concentration gradient is a negative sign because the concentration of drug compounds diffuses from high to low concentration when the distance is increased, as shown in Figure 14.
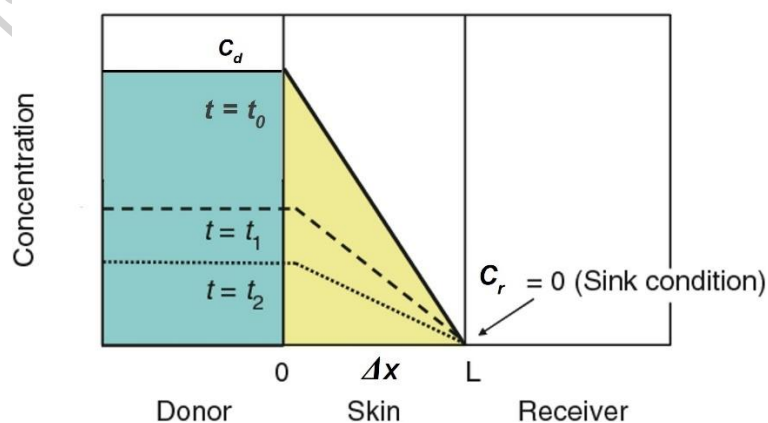
Figure 14: Concentration-distance profile of chemical compound in the barrier (82)

In pharmaceutics, the concentration in the receptor compartment (C_r) is very less and near zero compared to the donor compartment (C_d). Therefore, the

concentration in C_r is called sink condition. The permeability coefficient (K_p) can be calculated from Fick's laws of diffusion, following Eq. 2.

$$K_p = \frac{J}{\text{Area x } C_d} \qquad \text{Eq. 2}$$

The linear graph called the zero-order process is the relationship between the amount of drug that can diffuse through the membrane and time. This zero-order process represents the steady state of rate passive diffusion when the C_d not changed the concentration. However, due to the lag time effect, the graph is not a complete zero-order process in the early diffusion stage. The lag time is caused by the unsaturated membrane, calculated following Eq. 3.

$$t_{lag} = \frac{h^2}{6 \text{ x } K_d} \qquad \text{Eq. 3}$$

In real situations, the concentration of C_d is changed following the diffusion distance that affects steady-state conditions. Therefore, Fick's second law of diffusion is used to explain the flux and concentration gradient of the drug, following Eq. 4.

$$\frac{dc}{dt} = K_d \frac{d^2c}{dx^2} \qquad \text{Eq. 4}$$

The accumulation (or depletion) rate of concentration within the volume is proportional to the local curvature of the concentration gradient (83, 84).

2.7 Microemulsions for ocular drug delivery

Microemulsions are isotropic and thermodynamically stable phase transition systems with the dispersion of small droplet size (5-200 nm) that are composed of oil, water, and surfactant(s). In 1943, Hoar and Schulman discovered the microemulsion, a clear and transparent single-phase solution (85). Ocular microemulsions are interesting formulations because of various advantages such as high thermodynamical stability, ocular bioavailability, and prolonged drug effect in ocular tissue. Pharmaceutically, microemulsions are colloidal micro/nanodispersions of oil in water (o/w) or water in oil (w/o) types that are

stabilized by a surfactant film. The formulations or types of the microemulsion and various colloidal phases are illustrated by phase diagrams, as shown in Figure 15. The microemulsions can be categorized into 4 groups following the Winsor I-IV phase: Winsor I: o/w phase, Winsor II: w/o phase, Winsor III: bi-continuous phase and Winsor IV: homogeneous mixture phase (86, 87), represented in Figure 16. The advantages of microemulsions over emulsions are described in Table 5.
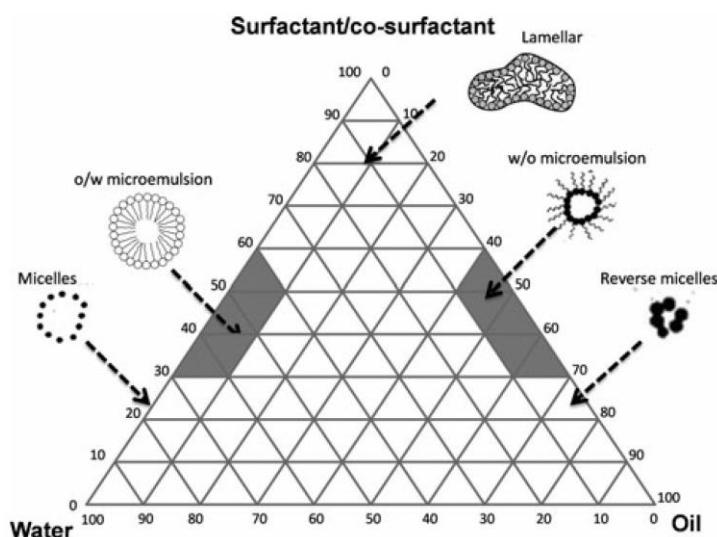
Figure 15: Quaternary phase diagrams or pseudo-ternary phase diagrams that are four component systems, including oil, water, surfactant, and co-surfactant (88)
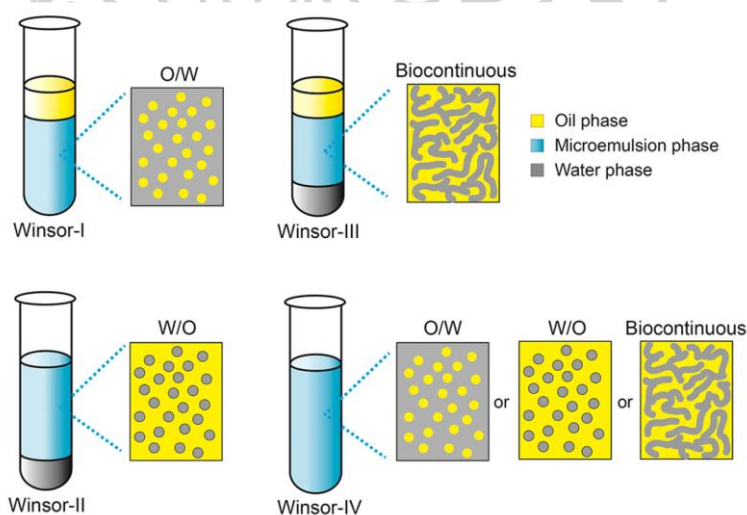
Figure 16: Winsor I-IV phase, including Winsor I: o/w phase, Winsor II: w/o phase, Winsor III: bi-continuous phase, and Winsor IV: homogeneous mixture phase (89)

Table 5: Characterizations between emulsion, microemulsion, and nanoemulsions

Parameters	Emulsions	Microemulsions	Nanoemulsions
Appearance	Turbid	Clear	Clear
Particle size	1 - 20 mm	5 - 200 nm	1 - 100 nm
Formulation	Mechanical shear	Spontaneous	Mechanical shear
Stability	Kinetically stable	Thermodynamically Stable	Kinetically stable
Phase	Biphasic	Monophasic	Monophasic
Viscosity	High	Low	Low
Interfacial tension	High	Ultra-low	Low
Optical isotropic	Anisotropic	Isotropic	Isotropic
Light scattering	Less scattering	Multiple scattering of visible light hence white	Multiple scattering of visible light hence white
Formulation methods	Wet/Dry Gum method Bottle method	Water titration method Phase inversion method	High-pressure homogenization Microfluidization Ultrasonication Phase-inversion composition Phase-inversion temperature Self-nanoemulsification
Preparation cost	Higher cost	Lower cost	Higher cost

2.7.1 Theories of microemulsion formulation

2.7.1.1 Thermodynamic theory

The formulation and stability of microemulsions are mainly based on simplified thermodynamic theory, following Eq. 5.

$$\Delta G = \gamma \, \Delta A - T \, \Delta S \qquad \text{Eq. 5}$$

Where ΔG is the Gibbs free energy of microemulsions that can be expanded by lowering the surface tension (γ) of the oil/water interface and the change in entropy (ΔS). ΔA is the change in the interfacial area on microemulsification, and T is the temperature. The microemulsion formulation is affected by a large change of ΔA due to a large amount of very small droplets. Therefore, γ, a very small positive value, is offset by ΔA and ΔS. The very large dispersion of entropy (ΔS) is increased from mixing one phase in the other phase that forms the numerous small droplets. When the large reduction in surface tension is expanded by mainly entropic change, a negative ΔG of the microemulsion is achieved. Hence, microemulsification is spontaneous, and the dispersion of microemulsion is thermodynamically stable (87, 90).

2.7.1.2 Solubilization theory

The formulation of microemulsions is oil and water-soluble phase by micelles and reverse micelles from surfactant or co-surfactant. The size range of microemulsions can affect the theory of swollen micellar systems (91, 92).

2.7.1.3 Interfacial theory

Normally, microemulsion can be formed spontaneously without any energy input by mixing the oil phase with the water phase containing surfactant and co-surfactant. During the mixing, the surfactant is formed between the oil and water interface. Co-surfactant is assisted in creating complex curvature film to reduce interfacial tension and generate microemulsion droplets in oil and water interface. According to this theory, the microemulsions have a low value of interfacial tension (γ) (92, 93).

2.7.2 Components of microemulsion

2.7.2.1 Oil phase

The oil phase is the most important component that influences the solubility and penetration of lipophilic drugs. It is low polarity and low miscibility with water due to low hydrophilic-lipophilic balance (HLB) (94). The physicochemical properties of the lipids such as saturated fatty acid, unsaturated fatty acid, and fatty acid have been studied about the long-chain fatty acids and high molecular weight affected to penetrate the interfacial film forming of surfactant/ co-surfactant to assist microemulsion curvature formulation. For this reason, the small molecular weight or medium chain of fatty acid is most frequently selected to form ophthalmic microemulsions. Moreover, lipophilic drugs should preferably be solubilized in o/ w microemulsion; therefore, the selected oil phase should have high solubility (95, 96).

2.7.2.2 Surfactant

The selected surfactant system is the most critical step in designing a microemulsion system that should reduce the interfacial tension to a very small value (nearly zero), facilitate the dispersion process and provide a flexible film. The concentration of surfactant should be high sufficient (10%-40%) to stabilize the droplets of microemulsion and greater than the critical micelle concentration (CMC) of the investigated surfactant (97). Generally, the acceptable HLB surfactants of o/w microemulsion formulation are 8-16, whereas surfactants with low HLB (3-6) are preferred for the w/o microemulsion formulation. The high HLB of surfactants greater than 20 often requires the co-surfactant to reduce its HLB value within the range of microemulsion formulations (98). The surfactant can be categorized into 4 groups following their charge of surfactants, including cationic, anionic, non-ionic, and zwitterionic surfactants. The selected surfactants should be no ocular toxicity, non-irritant,

biocompatibility, and biodegradability. Among the various types of surfactants, non-ionic surfactants such as polysorbate and sorbitan are selected with prolonged precorneal retention and improved permeability (99).

2.7.2.3 Co-surfactant

Typically, co-surfactants are combined with a surfactant to sufficiently reduce the o/w interfacial tension to form flexible microemulsions (100). The low molecular weight alcohols and glycols with medium chain lengths about C3-C8 are commonly used to form stable microemulsions due to easily increasing the interface's fluidity. However, the increasing chain length of alcohol is increasingly proportional to the ocular irritation, whereas the short carbon chain is performed as a mild irritant (101).

2.7.2.4 Aqueous phase

Generally, the aqueous phase solubilizes hydrophilic compounds and preservatives. In addition, buffer solutions are added in this aqueous phase to control the appropriate pH in the eyes (pH 7.0-7.4) (102). Commonly, water is used in this phase (93).

2.7.3 Method of microemulsions preparation

2.7.3.1 Water titration method

Quaternary phase diagrams or pseudo-ternary phase diagrams, which are four components system such as oil, water, surfactant, and co-surfactant, are usefully formulated microemulsions by spontaneous emulsification is low energy method and expanded microemulsion structure, illustrated in Figure 15. In this method, the mixture of oil, surfactant, and co-surfactant at different suitable proportions from 0 to 100% are homogenized, represented in the quaternary phase diagrams. To obtain a clear microemulsion, the mixture is titrated with distilled

water under a magnetic stirrer. Subsequently, the clearest phase of the quaternary phase diagrams region is the most stable microemulsion (103).

2.7.3.2 Phase inversion method

Phase inversion of the microemulsion can be occurred by adding an excess of the dispersed phase or increasing temperature when using a non-ionic surfactant. During the phase inversion, the physical of the microemulsion is drastically changed in particle sizes, which can affect the drug release from the microemulsion. However, the phase inversion method has not been reported on microemulsion for ocular drug delivery (104, 105).

2.7.4 Characterization of microemulsions

Microemulsion characterization can be mainly evaluated in three majors, including physical evaluation, electrochemical evaluation, and microscopic evaluation. Firstly, the physical microemulsion is observed in appearance, optical clarity, pH, and viscosity. The physical appearance of the microemulsion should be clear with the optical clarity due to the small droplet size evaluated by the light scattering method. Secondly, conductivity measurements can be used to determine the structure phase and dynamic of the microemulsion. Lastly, microscopic evaluation is assessed in their properties, such as particle size, size distribution, interactions, and dynamics. Many technologies have been used to evaluate particle size characterization, e.g., dynamic light scattering (DLS), small angle neutron scattering (SANS), and small angle X-ray scattering (SAXS), as well as cryo-transmission electron microscopy and pulsed-field gradient spin echo (self-diffusion) NMR. Moreover, the phase stability of microemulsion should be a concern (106, 107). Generally, microemulsions are thermodynamically stable; however, their microstructure continuously changes into biphasic regions during long-

term storage. Figure 17 shows the physical instabilities of the microemulsion, such as flocculation, coalescence, creaming, and phase separation (88, 108).
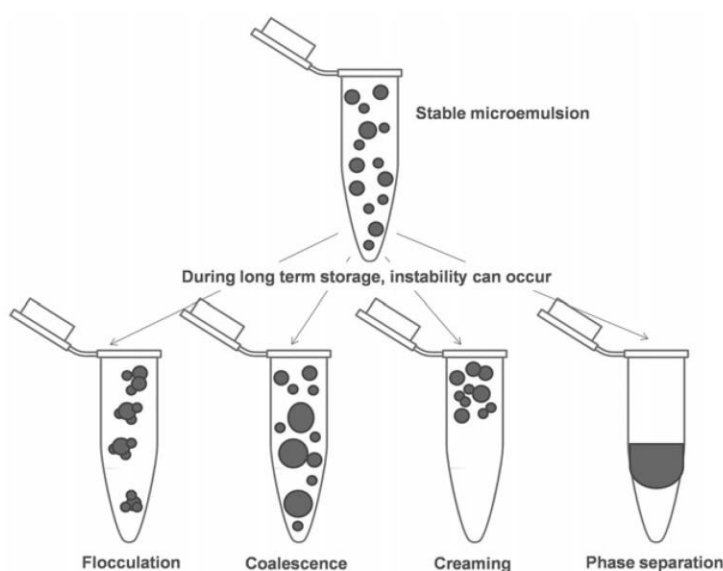
Figure 17: The physical instabilities of microemulsions after long-term storage (88)

2.7.5 Mechanism of drug release from microemulsions into the eyes

Generally, the drug loaded in the microemulsion exists in the internal phase (dispersion phase). The release of drugs in microemulsion can be explained by the drug diffusion and mass transfer constants through an ocular membrane. The principle of drug release from microemulsions through ocular membranes depends on partition coefficient, droplet sizes, and drug distribution in the microemulsion. The drug releases from the dispersion phase into a continuous phase of the microemulsion and then diffuses from a continuous phase through the ocular membrane. The surfactant and co-surfactant in microemulsion may enhance ocular permeation activity by acting as penetration enhancers by partitioning and disrupting the structural organization of the ocular lipid barrier (epithelium) (109, 110). Moreover, the small droplet size, high density of droplets, and

large amount of droplets in microemulsion formulations are increasing the surface area of drug formulations. Therefore, the drug in microemulsion droplets is in close contact with the ocular membrane providing a high concentration gradient and increasing ocular drug permeation (86, 111).

2.8 Microneedles for ocular drug delivery

Microneedles (MNs) are minimally invasive micron-scale technology for ocular drug delivery, typically around 25-1000 μm in height. MNs are the physical enhancement method similar to iontophoresis (112), electroporation (113), and sonophoresis (Ultrasound) (114) that change the structure of the barrier to increase the drug bioavailability. The advantages of MNs over other techniques are lower adverse effects, not using thermal heat, patients friendly, convenience, and high drug stability (38). Therefore, this technology is increasingly interesting for ocular drug delivery, such as amphotericin B (26, 115), bevacizumab (116), besifloxacin (117), anti-angiogenic monoclonal antibody with diclofenac (118), pilocarpine (119), methotrexate (120), triamcinolone acetonide (121, 122), sunitinib malate (123), sulforhodamine (22), sulprostone and brimonidine (124), that has been useful for ocular diseases treatment. MNs application to the eye has several advantages, such as minimally invasive ocular tissue, overcoming ocular tissue barrier, increasing ocular drug bioavailability, increasing patient compliance, and localized drug depot in ocular tissue. Moreover, the MNs avoid causing pain, tissue damage, and risk of infection because they do not puncture reach into the deep nerve ending and blood vessels under the corneal or sclera tissue barrier (31, 125). Using MNs in ocular drug delivery is a new concept; therefore, very little research has been published in this field. MNs for ocular drug delivery can be categorized into five types by mechanism and strategies, presented below in Figure 18. The advantages and disadvantages of each type of MNs are explained in Table 6.
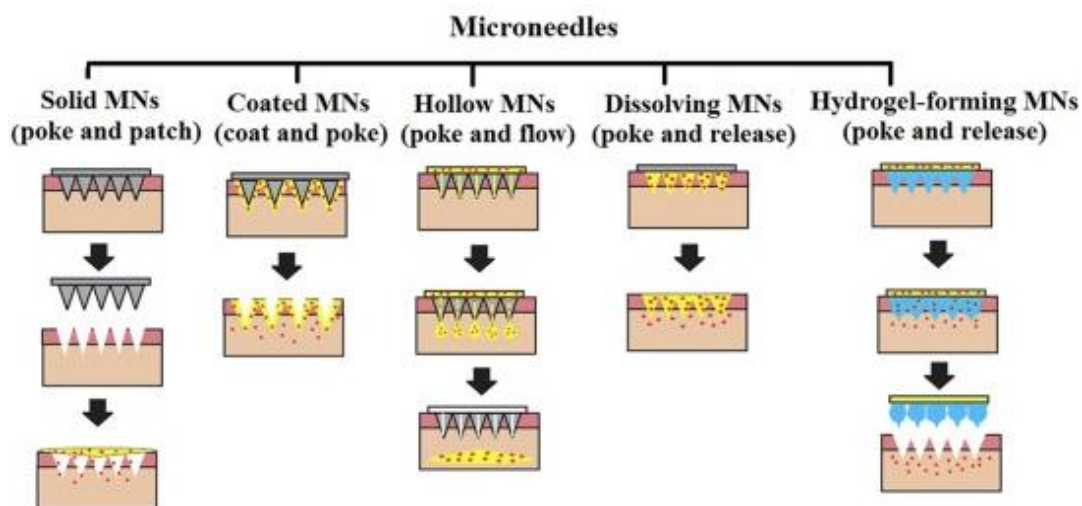
Figure 18: The types of MNs following the drug delivery mechanism of the solid MNs, coated MNs, hollow MNs, dissolving MNs, and hydrogel-forming MNs (126)

Table 6: The advantages and disadvantages of each type of MNs (127)

Types	Advantages	Disadvantages
Solid MNs	- High mechanical strength	- Poor dose accuracy
	- High physical stability	- Poor biocompatibility
		- Need retraction
Coated MNs	- High mechanical strength	- Dose limitation
	- Increasing dose accuracy	- Poor biocompatibility
		- Need retraction
Hollow MNs	- Increasing dose accuracy	- Clogging
	- Reasonable drug loading	- Requirement of a prefilled syringe
	- Constant flow rate	- Poor biocompatibility
		- Need retraction
Dissolving MNs	- Low-cost manufacturing	- Poor mechanical strength and physical stability
	- Easy to manufacture	
	- One-step application	
	- Biocompatibility	

Hydrogel-forming MNs	- Low-cost manufacturing	- Poor mechanical strength and physical stability
	- Easy to manufacture	
	- One-step application	
	- Biocompatibility	
	- Controlled drug release profile	

2.8.1 Types of MNs

2.8.1.1 Solid MNs

This strategy, also called "poke with patch" is fabricated from various materials such as silicon, stainless steel, aluminum, and glass. These solid MNs have two-step processes. In the first step, solid MNs is applied to the ocular tissue and removed to create microchannels, followed by the administration of drug formulation such as solution, suspension, ointment, and gel. Consequently, increasing drug permeation bypasses the ocular barrier. The movement of drug molecules in the formulations through the microchannels occurs *via* passive diffusion (31, 128).

2.8.1.2 Coated MNs

This method, called "coated and poke", is fabricated from the same materials of solid MNs (normally fabricated from stainless steel). The drug formulations are coated on MNs and insertion into the ocular tissue. Subsequently, the drug is deposited within the ocular tissue and diffused into the target site after being removed MNs. This strategy can reduce the step of administration when compared with solid MNs. However, the amount of drug-coated in MNs is limited (22, 129).

2.8.1.3 Hollow MNs

The third strategy of MNs for ocular drug delivery is hollow MNs or "poke and flow". This type is similar to hypodermic needles

containing a hollow bore; however, the needle size is reduced to a micron scale. The drug molecules can be transported into the ocular tissue *via* application through hollow MNs. The advantage of hollow MNs over solid MNs is adjustable fluid flow rate resulting in increased ocular drug delivery. However, this strategy can be limited only to liquid formulations (130, 131).

2.8.1.4 Dissolving polymeric MNs

This "poke and release" type is fabricated from a biodegradable and biocompatible polymer. The drug is incorporated into the polymeric MNs and subsequent insertion into the ocular tissue. When drug-loaded polymeric MNs come into contact with fluid in ocular tissue, thus, the polymer matrix dissolves and releases the drug into the target site. The advantage of this type over solid, coated, and hollow MNs is completely dissolved with no remaining biohazardous sharp waste and accurate dosing that reduces side effects from high doses (128, 132).

2.8.1.5 Hydrogel-forming MNs

The last type of MNs is hydrogel-forming MNs as an alternative approach called "poke and patch". After insertion, the MNs absorb the fluid in ocular tissue and allow drug release and diffusion into the tissue fluid from the drug reservoir during swollen polymeric matrix. The advantages of this type are constant drug release and suitability for sustained-release drugs. However, the study of hydrogel or swelling MNs has still been limited for ocular drug delivery (133, 134).

2.8.2 Method of MNs fabrication

In the last few decades, MNs fabrication methods have been widely explored, including conventional and modern techniques. The solid, coated, and hollow MNs are fabricated using conventional techniques such as laser

cutting, laser ablation, electrodeposition, etching, and lithography. Mostly, ocular MNs application is fabricated from dissolvable polymeric materials. The first choice of a fabrication technique for polymeric MNs is micromolding due to its high reproducibility, convenient fabrication, low-temperature process, and cost-effectiveness (135). Generally, hot embossing, injection molding, and investment molding methods are relatively high-temperature processing to fabricate insoluble and degradable polymeric MNs. Due to high-temperature processing that can affect to activity and stability of drugs (136, 137), the other MNs fabrications are drawing lithography, droplet-born air blowing (DAB), electro-drawing, and 3D printing that can rapidly achieve product within 10 min. DAB is a modern technique of fabrication in which the droplet of polymer is formed into MNs shape during air blowing. This technique avoids UV irradiation and high temperature. Moreover, the drug in MNs formulation can be controlled by a droplet dispenser (138, 139). Cyclic contact and drying are other methods like DAB which pillars are repeatedly contacted with a polymer-drug solution, lifted, and dried with air blowing (140). Drawing lithography is creating microstructures which are two-dimensional materials, into three-dimensional MNs. This method avoids UV irradiation and high temperature but has worse reproducibility (141). Electro-drawing is an alternative fast and mild temperature technique to fabricate biodegradable MNs by pyroelectric crystal, generating an electric field that drives the MNs drawing (140). Importantly, the above conventional technique can only fabricate flat MNs; consequently, the physical anatomy of the ocular surface is the curvature that is difficult to complete penetration of MNs into the eyes. According to the limitation, 3D printing technology has been attributed to versatility and tunability, designing geometric MNs shapes with computer-aided design (142). This technique provides high accuracy and good reproducibility (143). The selected method of MNs fabrication should be accurate, precise, reproducible, and robust. The process of each MNs fabrication technique is illustrated in Figure 19.
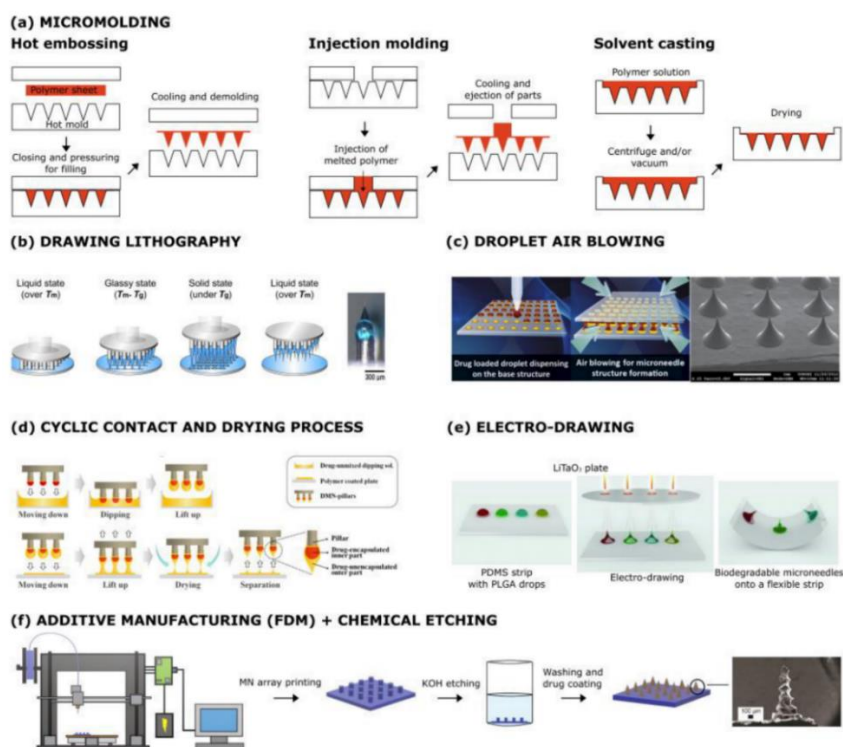
Figure 19: Methods of MNs fabrication: (a) micromolding, (b) drawing lithography, (c) droplet air blowing (DAB), (d) cyclic contact and drying, (e) electro-drawing, and (f) 3D printing by fused deposition modeling (FDM) (140)

2.8.3 Material for MNs fabrication

Recently, the materials are fabricated MNs for ocular drug delivery with different materials, such as metals, silicones, glass, and polymers. The materials for fabrication should be inert, biocompatible, and have appropriate mechanical strength and stability (144).

2.8.3.1 Metals

Typically, biocompatibility metals, including stainless steel, tantalum, titanium, and nickel, are used to fabricate solid, coated, or hollow MNs. The stainless steel has been approved the safety for MNs fabrication and ocular application by FDA (22, 145). Moreover, this material has many advantages, such as appropriate mechanical strength, easy to fabricate using laser cutting, and biocompatibility.

2.8.3.2 Silicones

This material is the simplest form to fabricate solid, coated, or hollow MNs. They can generally be fabricated by photolithography. The efficacy, biocompatibility, and safety of silicon have been studied (21). However, this material has hard and brittle properties that are easy to break into ocular tissue because of its fragile nature.
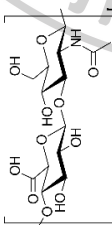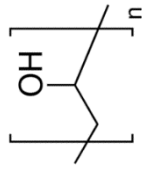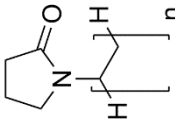
2.8.3.3 Glass
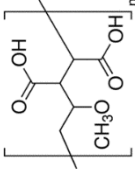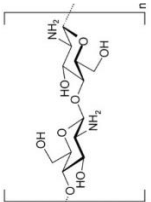
Mostly, glass type of MNs is an alternative to hollow metal MNs (131, 146). The glass MNs are generally fabricated by pulling a borosilicate glass pipette. The advantages of this material are resisted high temperatures and are easy to sterilize by moist or dry heat sterilization. Nonetheless, the limitations are easy to fragile and may remain in the body, time-consuming for fabrication, and specific for each experimentation; therefore, it is unsuitable.

2.8.3.4 Polymers

These materials are biodegradable, biocompatible, low toxicity, appropriate strength/toughness, and low cost to fabricate suitable MNs. However, the mechanical strength of polymers may not be as good as metal, silicone, and glass. The examples of polymers used to fabricate MNs for ocular drug delivery are represented in Table 7. These polymers are selected as the first choice for the fabrication of MNs for ocular use due to their strength/toughness, water-soluble polymer, quick disintegration/ dissolvability, and compatibility with ocular tissues. Polymeric MNs can be further divided into two categories following types of polymers, including dissolving MNs and swellable or hydrogel-forming MNs.

Table 7: Summary of different polymers currently studied for ocular drug delivery (144)

Materials	Structure	Biodegradable/ Biocompatible/ Dissolving (in ocular tissue)	Benefits	Limitations	Cost	Manufacture techniques
Hyaluronic acid (HA) (115, 118, 147)		Yes	- Rapid dissolution - Component similar to the eyes	- High material cost - Low hardness	◉◉◉ (> $100/kg)	Micromolding
Polyvinyl alcohol (PVA) (26, 115, 117, 148)		Yes	- Low cost - Different molecular weights available - Good plasticity and dissolvability	- Crosslink may reduce biocompatibility - Absorbs water quickly	◉ (< $20/kg)	Micromolding, 3D printed; Fused deposition modeling (FDM)
Polyvinyl pyrrolidone (PVP) (26, 115, 117, 148)		Yes	- Low cost - Different molecular weight	Difficulty scaling up the efficient process	◉◉ ($20–100/kg)	Micromolding, photopolymerization

Materials	Structure	Biodegradable/ Biocompatible/ Dissolving (in ocular tissue)	Benefits	Limitations	Cost	Manufacture techniques
			available			
			- Good plasticity and dissolvability			
Poly(methyl vinyl ether-comaleic anhydride) (PMVE/ MA); Gantrez® (147)		Yes	- Good hardness and dissolvability	High material cost	◎◎◎ (> $100/kg)	Micromolding,
Chitosan (149, 150)		Yes	- Good hardness and dissolvability	Can cause ocular irritation	◉ (< $20/kg)	Micromolding,

2.8.4 Characterization of MNs

Characterizing MNs is one of the most important parts of designing and developing MNs formulations to ensure they are suitable for use. This characterization confirms the quality and assurance of efficient utilization of MNs. The main evaluation parameters studied for appropriate MNs are morphology, dimensions of MNs, mechanical strength (insertion force, insertion depth, completeness of insertion, and resistant force), drug content, *in vitro*/*in vivo* study, and stability. Moreover, dissolution ability is the most important property of ocular dissolving MNs to design the appropriate application time for the eye. Many researchers used alternative evaluation parameters to characterize MNs, such as drug release, irritation test, histology, and tissue recovery after MNs application (151, 152).

2.9 The combination of MNs with micro/nanoparticles for ocular drug delivery

Currently, the MNs technology as a physical enhancer method has provided a versatile mechanism to increase the ocular drug delivery of micro/nanoparticles in a minimally invasive pathway. As well as the micro/nanoparticles can also increase ocular drug delivery by disrupting the ocular barrier and subsequent controlled drug delivery. Therefore, the synergistic enhancement combining micro/nanoparticles and MNs can improve ocular drug delivery. However, this combination depends on the particle size of micro/nanoparticles, microchannel on ocular tissue after MNs application and ocular tissue recovery. Recently, few studies reported using micro/nanoparticles loaded in dissolving MNs for ocular drug delivery, such as liposome-amphotericin B-loaded dissolving MNs (26, 115). However, this combination has been mostly studied in transdermal drug delivery fields e.g., nano/microparticles-vitamin D3 (153), cubosome-rapamycin (27), nanosuspension-curcumin (28), micelle-curcumin (154), solid lipid nanoparticle-albendazole (155) and nanocrystals-itraconazole loaded in dissolving MNs (29). Moreover, microemulsions loaded in dissolving MNs are still limited in every application route because MNs cannot be dried from the oil phase. Microemulsions are normally used as a topical

liquid solution after solid MNs insertion (156-158). To overcome this limitation, for the first time, two-layer dissolving polymeric MNs that encapsulates microemulsion inside the structure has been developed. The double-layer structured MNs allow biphasic polymer dissolution and packaging drugs for control release into the ocular tissue (118).

2.10 Safety considerations and sterilization of MNs

The MNs must be considered in the safety aspect before being applied to the eye. Few studies of the safety of using MNs for ocular applications are reported in the literature. However, Kim *et al.* studied the safety of applied coated MNs on rabbits' cornea. They showed that the small puncture on the corneal epithelium completely disappeared within 24 h with no sign of any complications observed, such as corneal opacity, redness, and hemorrhage. Moreover, histological studies of treated MNs on the cornea were evaluated. The results revealed no significant vascularization, macrophages, or inflammatory substance presence (129). For the dissolving MNs safety evaluation, Thakur *et al.* investigated the biocompatibility of the polymer with the retinal cells. The viability of cells showed no significant change after exposure to the retinal cells (120). The MNs produce significantly less pain than a hypodermic needle because the needle tips do not reach into nervous terminations that unearth the corneal barriers. The pain of MNs application on the eye depends on the length and number of the needle tips, which should be less than 1 mm to avoid pain and adverse effects (132, 159). Therefore, inserting MNs into the cornea is a minimally invasive technique with few or no adverse effects on the eye.

Moreover, the sterilization of MNs is required to avoid microbial infections in the eye. Therefore, the sterilization methods, such as dry heat sterilization, moist heat sterilization, ultraviolet, gamma radiation, and ethylene oxide, were used depending on the material for MNs fabrication. Unlike polymeric MNs, metal, silicon, and glass are easy to sterilize with dry and moist heat sterilization (160). The reason is that the strength and efficiency of polymeric MNs can be affected by radiation, dry heat

sterilization, and moist heat sterilization (161). Therefore, alternative sterilization procedures, such as gas sterilization, incorporated silver nanoparticles, and antimicrobial agent, are preferred (162).

2.11 Design of experiment

Design of experiment (DoE) is a statistical technique that helps to optimize the formulations using a statistical and mathematical model to explain the relationships between input factors (x_i - independent variables) affecting one or more output responses (y – dependent variables), as represented in Figure 20. In the DoE approach, controlled input factors are methodically varied to determine the effects on the output responses and determination of the most significant statistical inputs factor. To optimize the formulations, the selected input factors from statistic analysis are set to study interactions between input factors and optimize output responses. The advantages of this design technique are the reduced number of experiments, time, and the usage of reagents and materials.

2.11.1 The selection of experimental design

The considerations for selecting an experimental design should be defined objectives, the number and interactions of input factors to be studied, and the statistical validity and effectiveness of each experimental design. The experimental design can be divided into 2 types, i.e., screening designs and optimization designs (163, 164). Table 8 shows the summary of screening and optimization design characteristics.

Table 8: The summary of screening and optimization design characteristics.

Applications	Designs	Experiments	Levels	Factors
Screening	2-level full factorial	2^k	2	2<k<5
	Fractionate factorial	2^{k-p}	2	k>4
	Plackett-Burman	N	2	<N-1
Optimization	3-level full factorial	3^k	3	2<k<3
	Central composite	2^k+2k+C	5	2k<5
	Box-Behnken	2k(k-1)+C	3	3<k<5
	Mixture design	(m+k-1)!/m!(k-1)!	m>3	k>3

Where k is the number of input factors to be concerned, p is the number of generators chosen to fractionate the design, N is the number of experiments, C is a center point and m is the proportion of each level factor.

2.11.1.1 Screening designs

Screening designs are often applied in the first step of designing the experiment to choose the important input factors and discard the insignificant ones (165). The 3D spatial representations of screening designs are illustrated in Figure 20.
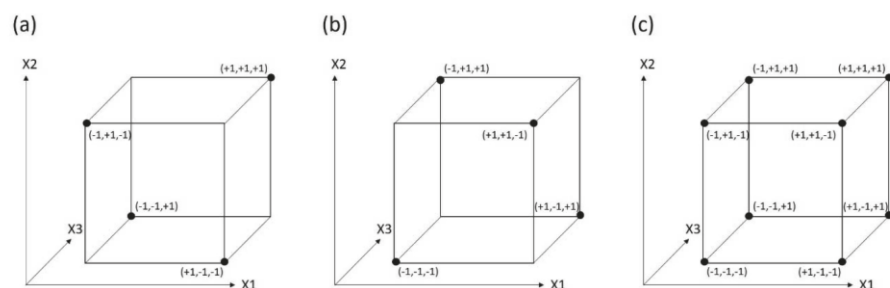
Figure 20: The 3D spatial representations of (a) fractionate 2-level factorial design (2^{3-1}), (b) its complementary matrix, and (c) 2-level full factorial design (2^3) (166)

- *Two-level full factorial designs:* This design is the most useful for screening, in which the design allows the estimation of main effects and the interactions of input factors affected output responses. The main limitation of this design is the large number of experiments required. The number of experiments needed for design can be calculated as 2^k, which k is the number of input factors to be concerned.

- *Fractionate factorial designs:* This design is more widely used for screening than two-level full factorial designs in case a large number of input factors are required because it reduces the number of experiments required. This design can be calculated by the adaptation of 2^k design into a 2^{k-p} design, in which p is the number of generators chosen to fractionate the design. However, the main effects and interaction of fractionating factorial designs that are aliased or confounded should have resided. Therefore, this design may not be appropriate for assessing the interactions of factors. The level of resolution of fractionating factorial designs is set according to the selection of generators.

- *Placket -Burman designs:* This design is a special type of two-level fractionate factorial designs. That allows one to estimate up to N-1 input factors with N experiments $(N \geq 4)$. This design is already set up for screening.

2.11.1.2 Optimization designs

The optimization designs are the most used to generate complex response surfaces, considering the trend of input factors impacting output responses. According to the limitation of screening designs, they only allow modeling linear response surfaces, which have only 2 levels for each input factor. Therefore, optimization

designs apply 3 to 5 levels for input factors; as a result, a model is generated quadratic response surfaces (163, 164). The 3D spatial representations of optimization designs are illustrated in Figure 21.
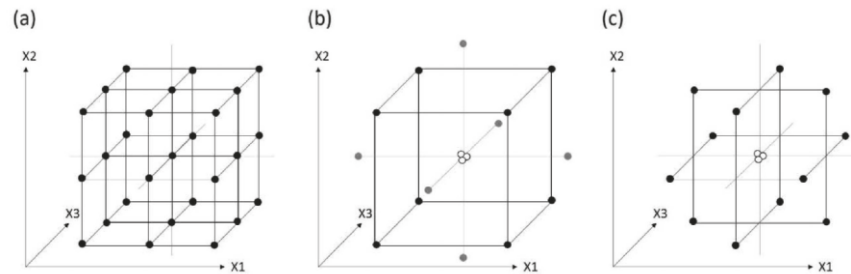
Figure 21: The 3D spatial representations of (a) three-level full factorial design (3^3), (b) central composite design (CCD), and (C) Box-Behnken design (166)

- *Three-level full factorial designs:* This design often applied only 2 or 3 input factors that needed to be studied due to the increasing number of experiments. The three-level full factorial design can be calculated as 3^k, in which k is the number of input factors concerned.

- *Central composite designs:* This design is one of the most applied optimizations due to using 5 levels of input factors with a reduced number of experiments, compared with a three-level full factorial design. The central composite designs compose of the factorial design points (black dots), the axial points (grey dots), and the center point (white dots).

- *Box-Behnken designs:* This design is a special type of three-level fractionate factorial designs, which allows linear response surface modeling and quadratic response surface modeling. These designs are more cost-effective than three-level full factorial designs, especially for many input factors.

- *Mixture design:* This design is a special type of response surface method (RSM). The constraint of input factors that the proportions of all ingredients must add up to 1 or 100% creates a

unique design region. The input factors must be more than 2 factors (167). The spatial representations of the mixture design are illustrated in Figure 22.
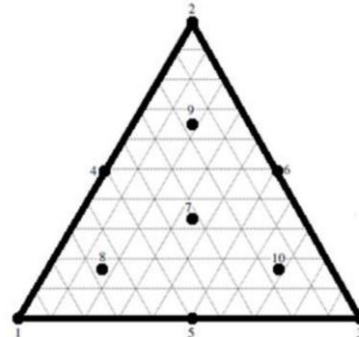
Figure 22: The spatial representations of mixture design (165).

2.11.2 The response surface methodology and the multiple regression model

Response surface methodology (RSM) is the combination of statistical and mathematical models to explain the relation of input factors affecting the output factors by 3D spatial representations (163). RSM is almost obtained using a linear, interaction, and quadratic function, as illustrated in Figure 23. The mathematical model should be selected based on analysis of variance (ANOVA) with significant value. Generally, RSM uses a regression analysis model to find the relationship of each factor, called a polynomial modal. Regression analysis aims to estimate and predict the output factors from input factors. The study of regression analysis that has factors more than 3 values (input factors > 2 and output factor = 1) is explained by a multiple regression model in Eq. 6-9 (164, 165).

Linear $\qquad y = \beta_0 + \sum_i^k \beta_i\, x_i + \varepsilon$ $\qquad$ Eq. 6

Linear+Interaction $\qquad y = \beta_0 + \sum_i^k \beta_i\, x_i + \sum_{ij}^k \beta_{ij}\, x_i x_j + \varepsilon$ $\qquad$ Eq. 7

Linear+quadratic $\qquad y = \beta_0 + \sum_i^k \beta_i\, x_i + \sum_i^k \beta i^2\, x_i^2 + \varepsilon$ $\qquad$ Eq. 8

Linear+interaction+quadratic $\quad y = \beta_0 + \sum_i^k \beta_i\, x_i + \sum_{ij}^k \beta_{ij}\, x_i x_j \sum_i^k \beta_i^2\, x_i^2 + \varepsilon$ Eq. 9

Where x_i or x_j are the input factors, y is an output factor, β is a regression coefficient, and ε is an error variable.
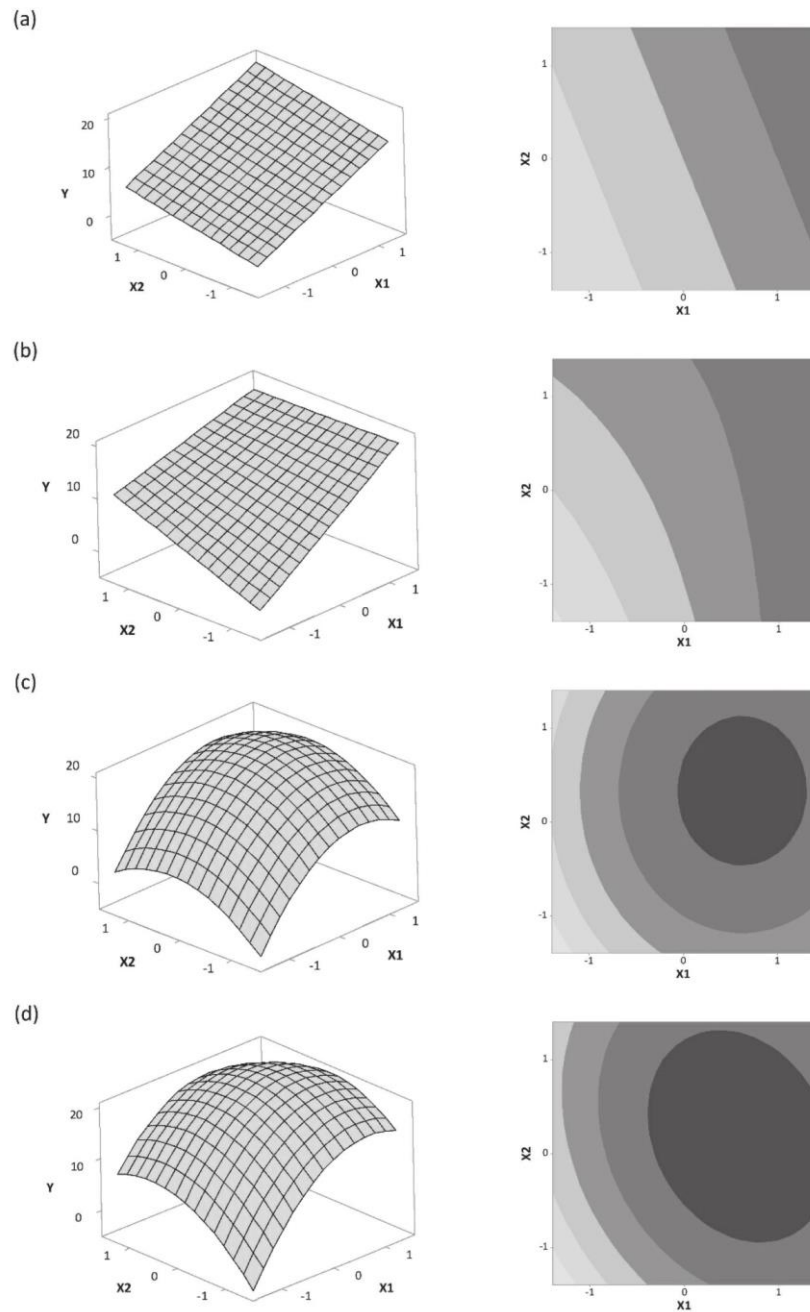
Figure 23: Response surface area and contour plots of (a) linear, (b) linear + interaction, (c) linear + quadratic, and (d) linear + interaction + quadratic model functions (166).

2.11.2.1 Regression Coefficient

   Based on ANOVA, the regression coefficient can be decided to include or exclude the terms of multiple regression models such as liner, interaction, and quadratic. The decision is based on the *p*-values of each regression coefficient term that should be less than 0.05 to be included. It can be explained that the input factor affects to output factors. Moreover, the positive and negative signs in front of the regression coefficient explain a direction or inversion of the relationship between input and output factors (165, 166).

2.11.2.2 The coefficient of determination (R^2)

   Determination coefficients (R^2, adjust R^2, and predict R^2) are used to assess the multiple regression model. Generally, the appropriate value of determination coefficients approaches 1. R^2 is the proportion of the output responses (Y) which is well predicted from input factors (X). However, R^2 can be increased value by adding new terms of the multiple regression model, which is not good for comparison with other different number terms of regression models. Therefore, the adjusted R^2, a reformed R^2 version by adjusting the number of regression model terms, can be compared with the different number of regression model terms. The predictive R^2 is used to explain how well a regression model precisely predicts output responses. Typically, the value of adjusted R^2 and predicted R^2 is lower than R^2 (165, 166).

2.11.2.3 Model adequacy checking

   Generally, model adequacy checking should be assessed in normality residues, independence of residual, constant variance, and lack of fit. The assumption of residuals (ε) from the experiment should approach zero (165, 166).

- *Normality of residuals:* This evaluation can be explained by the normal probability plot. The data should be arranged in a linear graph.
- *Independence of residuals:* The residuals should be arranged in homoscedasticity which each data is independent.
- *Constant variance:* That can be checked by a residual plot, in which the pattern of the graph should be random distribution or no pattern. If the graph trend has a curve or linear pattern, the variance is not constant.
- *Lack of fit:* The variability of the regression model can be explained by lack of fit. When the lack of fit is insignificant (p-value > 0.05), it indicates that the regression model is less pure error and well fitted. The lack of fit can increase the precision and be well-fitted by replicating the experiment, usually for the central point.
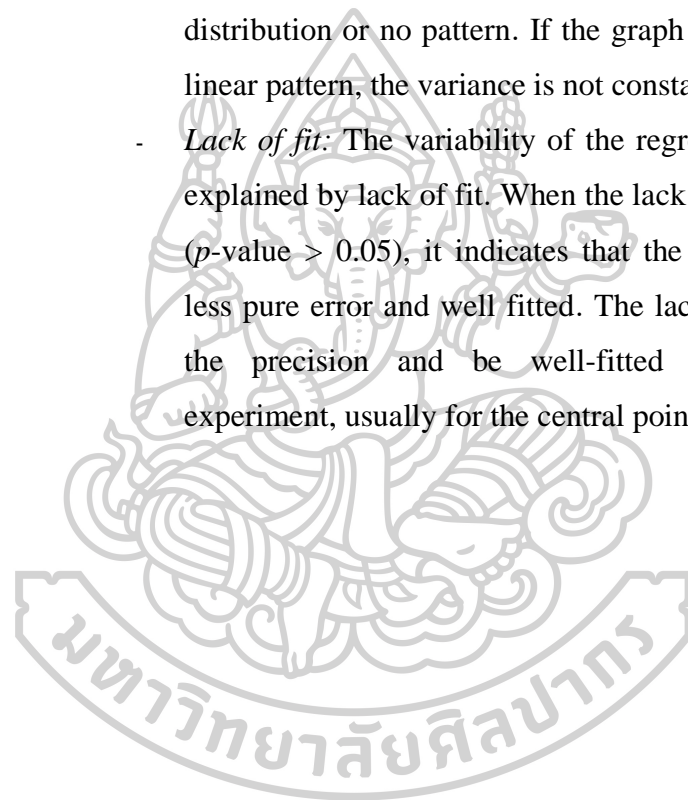
CHAPTER 3

MATERIALS AND METHODS

3.1 Materials

- Fluconazole (Tokyo Chemical Industry, Tokyo, Japan)
- Fluorescein sodium (FS; molecular weight 376. 27 Da) (Sigma-Aldrich, Dorset, United Kingdom)
- Rhodamine B (Sigma-Aldrich, Dorset, United Kingdom)
- Chitosan (low molecular weight; 50-190 kDa) (Sigma-Aldrich, Dorset, United Kingdom)
- Hyaluronic acid (HA; molecular weight 1200–1800 kDa) (P.C. Drug Center, Bangkok, Thailand)
- Polyvinyl alcohol (PVA; 99+ % hydrolyzed molecular weight 89-98 kDa) (Sigma-Aldrich, Dorset, United Kingdom)
- Gantrez® S-97 (Poly-methyl vinyl ether-alt-maleic acid; MW = 1500 Da) (Ashland Inc, Surrey, United Kingdom)
- Eugenol (Bruno Court, Grasse, France)
- Wintergreen oil (Charabot, Grasse Cedex, France)
- Orange oil (P.C. Drug Center, Bangkok, Thailand)
- Peppermint oil (P.C. Drug Center, Bangkok, Thailand)
- Oleic acid (Sigma-Aldrich, Dorset, United Kingdom)
- Limonene (Sigma-Aldrich, Dorset, United Kingdom)
- Cremophor® RH 40 (PEG-40 hydrogenated castor oil) (P.C. Drug Center, Bangkok, Thailand).
- Labrafac™ PG (Propylene glycol dicaprolate) (Gattefossé, Lyon, France)
- Labrasol® (Caprylocaproyl Polyoxyl-8 glycerides) (Gattefossé, Lyon, France).
- Tween 20 (Sigma-Aldrich, Dorset, United Kingdom)
- Tween 80 (Sigma-Aldrich, Dorset, United Kingdom)
- Span 20 (Sigma-Aldrich, Dorset, United Kingdom)

- Span 80 (Sigma-Aldrich, Dorset, United Kingdom)

- Methanol (MeOH; EMSURE®, Darmstadt, Germany)

- Ethanol (EtOH, Honeywell, Muskegon, United State)

- Isopropyl alcohol (IPA, Sigma-Aldrich, Dorset, United Kingdom)

- Polyethylene glycol 400 (PEG 400) (Sigma-Aldrich, Dorset, United Kingdom)

- Propylene glycol (PG) (Sigma-Aldrich, Dorset, United Kingdom)

- Glycerol (Sigma-Aldrich, Dorset, United Kingdom)

- Sodium bicarbonate ($NaHCO_3$) (Fisher Scientific, Leicestershire, England)

- Potassium dihydrogen orthophosphate (KH_2PO_4, Ajax Finechem, Australia)

- Sodium dihydrogen orthophosphate (NaH_2PO_4, Ajax Finechem, Australia)

- Sodium chloride (NaCl; QReC Chemical, New Zealand)

- Potassium chloride (KCl; Ajax Finechem, Australia)

- Sodium hydroxide (NaOH; Ajax Finechem, Australia)

- Calcium chloride ($CaCl_2$; Ajax Finechem, Australia)

- Magnesium sulfate anhydrous ($MgSO_4$)

- D-Glucose (anhydrous) (Scharlau Chemie, Barcelona, Spain)

- All chemical agents were analytical reagent grade.

3.2 Equipment

- Design Expert® 11 trial version (Stat Ease, USA)

- OriginPro® 2020 (OriginLab Corporation, Northampton, USA)

- SPSS® software version 19 trial version (SPSS Inc., Chicago, IL)

- Beaker (Pyrex, USA): 50 mL, 100 mL, 250 mL and 1 L

- Cylinder (Pyrex, USA): 25 mL, 50 mL and 100 mL

- Stirring rod

- Duran bottle: 500 mL, 1 L, 2 L

- Disposable syringe (Nipro, Thailand): 1 mL, 3 mL, 10 mL, 50 mL

- Needle (Nipro, Thailand): 18, 26-gauge

- Micropipette and micropipette tip: 0.5-2 µl, 2-20 µl, 20-200 µl, 100-1000 µl, 1-5 mL

- Microcentrifuge tube 1.5 mL and Centrifuge tube 15 mL, 50 mL
- Disposable Petri dishes
- Sartorius® series-CP224S analytical balance (Data Weighing Systems, Inc. , Illinois, USA)
- Rotary shaker
- Vortex mixer
- Zetasizer Nano ZS (Malver Instruments, Malver, UK)
- pH meter (LAQUAtwin-pH-22, Japan)
- Water bath (Hetofrig CB60; Heto High Technology, Florida, USA)
- Bath sonicator (Transsonic series 890/H, Singen, Germany)
- Probe sonicator (Sonics VibraCellTM, Newtown, USA)
- Polydimethylsiloxane (PDMS) micro-mold (Blueacre Technology, Ireland)
- Centrifuged (ALC, PK121R, UK)
- Vacuum chamber (TÜV Rheinland, Thailand)
- Dino-Lite Edge digital microscope (AM7915 Series, Taiwan)
- Scanning electron microscope (SEM; S-3400N, Hitachi, Japan)
- Inverted fluorescence microscope (Nikon® TE2000-U, Japan)
- Confocal Laser Scanning Microscope (CLSM; OLYMPUS FV1000, Japan)
- Cryostat (Leica 1850, Leica Instrument, Nussloch, Germany)
- Texture analyzer (TA. XT plus, Stable Micro Systems, UK)
- Nylon syringe filter 0.45 µm (Vertical®, Bangkok, Thailand)
- Peristatic pump on the suction line
- High-performance liquid chromatography (HPLC) (Model: 1260 infinitely series, Agilent Technologies Inc., California, USA)
- Zorbax Eclipse XDB-C18 reverse phase column (250 x 4.6 mm, 5 µm pore size) (Agilent, Santa Clara, USA)
- Microplate reader (VICTOR Nivo™ Multimode Plate Reader, PerkinElmer, Germany)
- Hemisphere-shaped Franz diffusion cell (volume 4 mL)
- Magnetic stirrer and magnetic bar
- Automatic autoclave (Model: LS-2D; Scientific promotion CO. , Ltd. , Thailand)

- Hot air oven

- Laminar airflow (BIO-II-A)

- Incubator culture

- Desiccator

- Refrigerator (4-8°C) and Freezer (-20°)

- Aluminum foil

- Polymeric film (Parafilm M®; Bemis NA, USA)

- Scissor, scalpel blade, and fine forceps

- Dental wax (eyeball half shape)

3.3 Methods

3.3.1 Optimization of the outer layer of the two-layer dissolving MNs using 3-level factorial design

The three-level design (3^k factorial design) was applied as a tool to design and optimize the formulation. The experimental design and analysis were performed by Design Expert® 11 (Stat Ease, USA). The independent factor was the weight ratios of the polymer mixture and the dependent factors were MNs height (Y_1) and mechanical strength (Y_2). The total of 12 experimental runs (3^2 with 3 center points) was calculated by the ANOVA statistical significance of the model (*p*-value< 0.05). The suitability of the model was determined from lack-of-fit, while the accuracy of fit used the coefficient of determination (R^2). After that, the independent factors were optimized with the highest mechanical strength and MNs height. The optimal formulation was tested for the accuracy of prediction by a two-sided *t*-test with a *p*-value < 0.05.

3.3.1.1 Fabrication of the outer layer dissolving MNs

- Chitosan and PVA

The 3%w/w chitosan was dissolved in 0.1% acetic acid solution. After that, the 20%w/w PVA was dispersed in water at 80 °C in a water bath and

mixed with the 3%w/w chitosan polymer solution in various weight ratios at room temperature. To fabricate the dissolving MNs, the 0.5 g of the mixed polymer solution was cast into the 11x11 array polydimethylsiloxane (PDMS) micro-mold (Blueacre technology, Ireland) with a base diameter of 300 μm, height of 600 μm, and interspacing of 300 μm. The molds with polymeric aqueous solutions were subsequently centrifuged (ALC, PK121R, UK) at 4000 rpm, 25 °C for 30 min and placed in a vacuum chamber (TÜV Rheinland, Thailand) for 30 min (60 psi, 25 °C) to remove air bubbles. The polymer was filled into the mold cavities. MNs were allowed to dry at 25 °C for 24 h. Finally, the dried MNs were gently removed from the micromold and kept in the desiccator.

- Gantrez® S-97 and hyaluronic acid

The 30%w/w Gantrez® S-97 was dissolved at 60 °C in a water bath. After that, the 5%w/w hyaluronic acid (HA) was dispersed in water at 25 °C and then mixed with the 30%w/w Gantrez® S-97 polymer solution in various weight ratios at room temperature. Gantrez® S-97 and hyaluronic acid MNs were fabricated using the method previously described.

- PVA and hyaluronic acid

The 5%w/w HA was dissolved at 25 °C. After that, the 20%w/w PVA was dispersed in hot water at 80 °C and then mixed with the 5%w/w hyaluronic acid polymer solution at various weight ratios at room temperature. Finally, PVA and hyaluronic acid MNs were fabricated using the method previously described.

3.3.1.2 The physical appearance and mechanical strength

The MNs height was evaluated by a digital microscope Dino-Lite Edge/5MP (Hsinchu, Taiwan). The mechanical strength was assessed using a texture analyzer (TA. XT plus, Stable Micro Systems, UK) connected with a 5 kg load cell. The MNs were mounted on the cylinder probe (P/10KSS) with

the MNs tip facing down and tested in compression mode. The displacement rate was 1 mm/s, and force was constantly increased until the displaced height of the MNs around 0.6 mm. The maximum MNs height and mechanical strength at 0.6 mm displaced the MNs height were calculated in 3^k factorial design to find the optimal first layer dissolving MNs formulation. After that, each first layer of dissolving MNs was compared to the highest MNs height and mechanical strength. The optimal formulation was then selected to fabricate the outer layer of two-layer dissolving MNs.

3.3.2 Design and formulation of optimal MEs-FLUZ

3.3.2.1 Solubility of FLUZ in various oils, surfactants, and co-surfactants

To find the suitable formulation, oil, surfactant, and co-surfactant in microemulsions were tested by observing the solubility of FLUZ in separate excipients. These are various oils, including isopropyl myristate (IPM), oleic acid, eugenol, peppermint oil, light liquid parafilm, limonene, medium chain triglyceride (MCT), orange oil, and wintergreen oil; surfactants (Tween 20, Tween 80, Span 20, Span 80, Brij® 97, Cremopher® RH 40, Labrasol® and Labrafac® PG) and co-surfactants (ethanol, isopropyl alcohol (IPA), polyethylene glycol 400 (PEG 400), propylene glycol (PG) and glycerol) were determined. In centrifuge tubes, excess amounts of FLUZ were added into 2 mL of various oils, surfactants, and co-surfactants. The centrifuge tubes were agitated at 25 ± 0.5 °C for 72 h. The equilibrated FLUZ samples were then centrifuged at 14000 rpm for 20 min to separate the insoluble FLUZ. After that, the supernatants were filtered through a cellulose filter (0.45 µm) and drug concentration in the samples was determined by HPLC (Agilent, Santa Clara, United States) after appropriate dilution with methanol. The chromatographic separation was performed using a Zorbax Eclipse XDB-C18 reverse phase column (250 x 4.6 mm, 5 µm pore size) (Agilent, Santa Clara, United States). The conditions of FLUZ analysis used isocratic elution were 45%v/v methanol: 55%v/v ultrapure water, flow rate at 1 mL/min, and the

wavelength of detection at 260 nm at a controlled temperature of 25 ± 2 °C. The retention time of FLUZ was 4.9 min.

3.3.2.2 Construction of pseudo-ternary phase diagram

Microemulsion consists of three components: oil, S_{mix} (surfactant and co-surfactant), and water. A pseudo-ternary phase diagram was developed from selected oil, surfactant, and co-surfactant based on the highest FLUZ solubility obtained. The different ratios of surfactants to co-surfactants (S_{mix}) (1:1, 1:2, 2:1, 3:1) were prepared. The mixture containing oil, surfactant, and co-surfactant was mixed with the weight ratio of the oil to the S_{mix} at 1:9, 2:8, 3:7, 4:6, 5:5, 6:4, 7:3, 8:2, and 9:1, respectively. The aqueous titration method was done to each weight ratio of oil and S_{mix} under moderate stirring. The diluted mixtures were directly observed visually for any phase separation. The mixtures with transparent, clear, or slight bluish appearance were considered to be in the microemulsion region of the pseudo-ternary phase diagram. The pseudo-ternary phase diagrams were constructed using a trial version of OriginPro® 2020, graphing and data analysis software.

3.3.2.3 Optimization of MEs-FLUZ

- *Formulation of MEs-FLUZ*

The 10%w/w of FLUZ was dissolved in selected oil using a vortex mixer. A weight ratio of S_{mix} and water selected by computer design were added to the mixtures. These mixtures were mixed and warmed under a water bath at 40 °C for 10 min to ensure complete mixing.

The mixture component of microemulsions was designed based on a three-component system: the oil (X_1), the S_{mix} (X_2), and the water (X_3). This study selected the concentrations range of three components in the microemulsion region of a pseudo-ternary phase diagram as independent factors. The dependent factors for microemulsions evaluation were droplet

size (Y_1), PDI (Y_2), drug content (Y_3), and percent drug permeation at 8 h (Y_4). The concentrations of the three components were changed by computer design simultaneously; however, they still kept their total concentration of 100%. Firstly, the Design-Expert® version 11 software trial version using I-optimal design was used to generate batches of microemulsion to evaluate the relationship between independent and dependent factors. Afterward, the independent factors were optimized with the lowest droplet size (Y_1), PDI (Y_2), and the highest drug content (Y_3), % percent drug permeation at 8 h (Y_4). The optimal formulation was tested for prediction accuracy by a two-sided *t*-test with a *p*-value < 0.05.

- *Characterization of MEs-FLUZ*
- **Droplet size, PDI, and Zeta potential Measurement**

Photon correlation spectroscopy (PCS; Zetasizer Nano Series, Malvern Instruments, United Kingdom) was used to determine the droplet size, PDI, and zeta potential of microemulsion containing FLUZ. Light scattering was observed at a 90° angle, 25°C.

- **pH value**

The pH value of microemulsions was determined using a pH meter (Laquatwin Horiba, Kyoto, Japan) to determine the formulations that were appropriate to use in the eyes.

- **Centrifugation test**

Each microemulsion formulation was centrifuged at 4000 rpm for 15 min to determine whether the system showed signs of creaming or phase separation.

- **Drug content**

The MEs-FLUZ were diluted as appropriate in methanol solvent. After that, the mixtures were filtered through a cellulose filter (0.45 µm). The FLUZ concentration in each sample was determined by HPLC, as previously described in 3.3.2.1.

3.3.3 Preparation of MEs-FLUZ-loaded two-layer dissolving MNs

Two-layer dissolving MNs were fabricated by the simple micro-molding method, as presented in Figure 1. In this study, the outer layer of MNs formulation was selected as described in section 2.1. Briefly, approximately 0.2 g of polymer mixture was cast into PDMS micro-mold as a first layer and centrifuged at 4000 rpm, 25 °C for 30 min to fulfill the polymer mixture in the mold cavities and to eliminate the bubbles. The excess of the polymer mixture on the top of the PDMS micro-mold was removed and dried at room temperature for 6 h. Then, 0.2 g of optimal MEs-FLUZ suspended in 20% Pluronic® F-127 as an inner layer was poured into the PDMS micro-mold and centrifuged as mentioned above. The excess of the MEs-FLUZ was removed. This micro-mold was kept at 4 °C for 30 min. To produce a robust supporting patch, 30% Gantrez® S-97 was added and centrifuged at 2000 rpm, 4 °C for 10 min. Finally, the two-layer dissolving MNs loading MEs-FLUZ were dried at 25°C for 24 h and gently peeled off from the PDMS micro-mold, represented in Figure 24. The two-layer dissolving MNs loading MEs-FLUZ were collected and kept in the desiccator before further characterization.
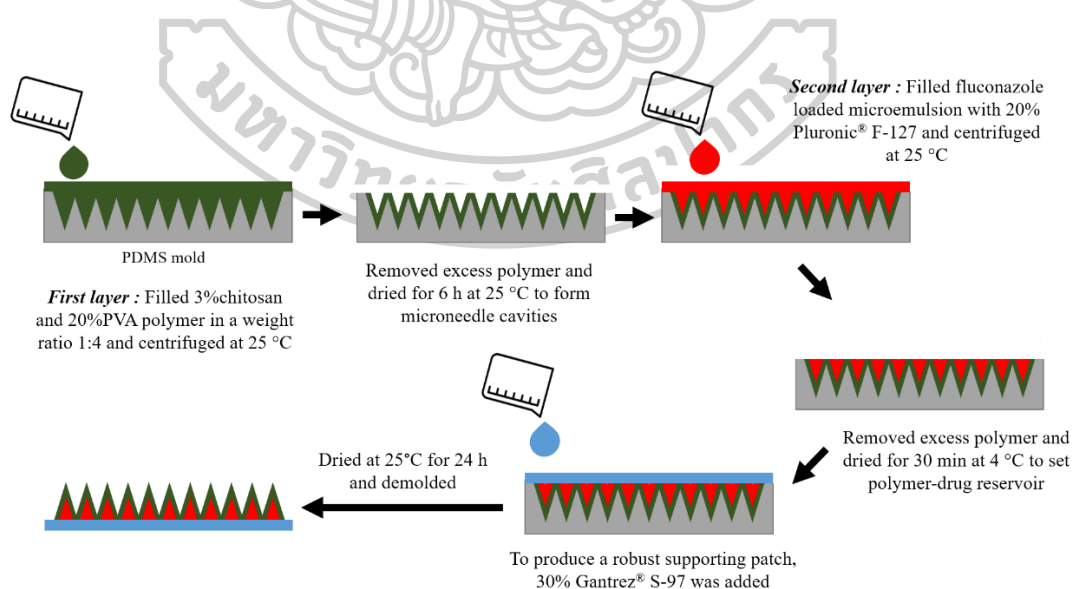
Figure 24: Schematic diagram of MEs-FLUZ-loaded two-layer dissolving MNs fabrication

3.3.4 Characterization of MEs-FLUZ-loaded two-layer dissolving MNs

3.3.4.1 The physical appearance of two-layer dissolving MNs

To assess the physical characteristics of two-layer dissolving MNs comprising MEs-FLUZ, a scanning electron microscope (SEM; Mira TC, Czech Republic) was utilized. The needles' height, width, and interspace of the MNs were measured. Additionally, to confirm the success of two-layer dissolving MNs fabrication, 1% fluorescein sodium (FS) was loaded into the outer layer as a water-soluble phase, while 0.5% rhodamine B was loaded into the inner layer as an oil phase. This two-layer dissolving characteristic was evaluated using a confocal laser scanning microscope (CLSM; OLYMPUS FV1000, Japan).

3.3.4.2 The mechanical properties of two-layer dissolving MNs

- *Mechanical strength*

To determine the mechanical strength of the micro-needles (MNs), a texture analyzer connected to a 5 kg load cell was utilized. The MNs were attached to the cylinder probe (P/10KSS) with the MNs tip facing downwards and were tested in compression mode, with a displacement rate of 1 mm/s. A constant force was applied until the MNs had been displaced to a 0.6 mm height. The one- and two-layer dissolving MNs, both with and without MEs-FLUZ, were subjected to this test. Subsequently, the mechanical strengths versus displacement curves were plotted.

- *Preparation of porcine eyeballs and corneal tissues*

Porcine eyes were commonly employed as a suitable substitute for human eyes in various studies due to their similarities in ocular histology and water content. The fresh porcine eyeballs were sourced from a local slaughterhouse (Nakhon Pathom Province, Thailand) and were either used within 24 h of receipt or stored in a sealed container with PBS pH 7.4 at -20 °C for up to 3 months. To prepare the corneal tissue, the porcine eyeballs were thawed in a water bath at 37 °C, and any adherent muscle tissue was removed. The corneal tissue located at the anterior segment of the eye was removed

circumferentially around 1 cm from the limbus and then soaked in PBS pH 7.4 at 37 °C for 30 minutes before being used in the experiment.

▪ *Insertion force*

The insertion force of one- and two-layer dissolving MNs with/without MEs-FLUZ were tested on the porcine corneal tissues fixed on a hemisphere dental wax (eyeball half shape). The compression mode condition is set to evaluate the MNs as previously described in the mechanical strength method. The insertion forces versus displacement curves were plotted.

• *The percentage of insertion completeness*

The effectiveness of the micro-needles (MNs) in achieving complete insertion into corneal tissue was evaluated using a polymeric film, specifically Parafilm M® from Bemis NA, USA, which mimics the corneal thickness of approximately 650 μm. The MNs were placed on the polymeric film's fifth layer and subjected to an insertion force for 30 s, as previously described. The number of visible dots on the surface of the fifth layer of the polymeric film was then counted using a Dino-Lite digital microscope. Both one- and two-layer dissolving MNs, with or without MEs-FLUZ, were tested. The ability of the MNs to penetrate the polymeric film was calculated using Eq. 10.

$$\text{Percentage of insertion completeness} = \frac{\text{Number of visible dots}}{\text{Number of microneedles}} \times 100 \qquad \text{Eq. 10}$$

• *Insertion depth*

In order to assess the insertion depth of MNs, the artificial membranes from the previous study were taken and each layer was removed one by one. The last remaining visible dot was then observed under a digital microscope to calculate the insertion depth. Each layer of the artificial membrane was 0.13 mm thick. Additionally, the first layer of the two-layer MNs, loaded with 1% FS, was applied to porcine corneal tissue for approximately 3 min before removal. The corneal tissue was then washed with PBS pH 7.4, and the

insertion depth was evaluated under a confocal laser scanning microscope (CLSM) using top-view confocal micrographs. For cross-sectional corneal tissue, the applied corneal tissue was fixed with a 4% formaldehyde solution for 24 h before being embedded in frozen section media and cryo-sliced (10 μm thickness each) at -35 °C using a cryostat (CM1850, Leica Biosystems, Germany). The samples were then immediately observed under a fluorescence microscope (Nikon® T-DH, Japan).

3.3.4.3 The complete dissolution times

The time required for dissolving two-layer dissolving MNs containing MEs-FLUZ was measured after being applied to the corneal tissue. The corneal tissue was fixed on a hemisphere dental wax, which mimics an eyeball shape, and then it was moistened with 0.5 mL of phosphate-buffered saline (PBS) pH 7.4. Next, the MNs formulation was inserted into the corneal tissue using the insertion force for 30 s from the previous study and then removed after certain intervals such as 0, 1, 2, 3, and 5 minutes. The complete MNs dissolution time was observed under a digital microscope.

3.3.4.4 Loading efficiency of MEs-FLUZ-loaded two-layer dissolving MNs

The MEs-FLUZ-loaded two-layer dissolving MNs was dissolved in 2 mL of methanol. To precipitate the polymer, the sample solution was centrifuged at 14000 rpm for 30 min at 25°C and the supernatant was filtrated by a nylon syringe filter 0.45 μm (Vertical®, Bangkok, Thailand) before being analyzed by HPLC. The percentage of loading efficiency (%LE) was calculated following Eq. 11.

$$\%\text{Loading efficiency} = \frac{\text{Actual amount of FLUZ } (\text{mg})}{\text{Initial amount of FLUZ } (\text{mg})} \times 100 \qquad \text{Eq. 11}$$

3.3.5 *In vitro* ocular permeation

The ocular permeation of MEs-FLUZ-two-layer dissolving MNs was performed on the porcine corneal tissues as a membrane, representing the human cornea. An adapted Franz diffusion cell that contains a hemisphere-shaped receptor and donor compartment fits for supporting the curvature of corneal tissues. The receptor compartment was filled with 4 mL of PBS pH 7.4, maintained at 37 °C, and continuously stirred by a magnetic stirrer bar. The formulations in this study were F1 - FLUZ suspension, F2 - FLUZ in eugenol, F3 – MEs-FLUZ, F4 - FLUZ suspension-loaded one-layer MNs, and F5 – MEs-FLUZ-loaded two-layer MNs. Each formulation with the same concentration of FLUZ was added to the donor chamber. The 300 μl samples were collected from the receptor compartment at predetermined time points, including 0, 0.25, 0.5, 1, 2, 4, 6, 8, 12, and 24 h. An equal volume of fresh PBS (pH 7.4) was replaced to maintain a volume in the receptor compartment. The concentrations of FLUZ were analyzed using HPLC.

The ocular permeation profiles data revealed several parameters that help to understand how the drugs behave when delivered across the corneal tissue. These parameters include Q_{24}/A (the cumulative amount of FLUZ per area), J (flux), t_{lag} (lag time), K_d (diffusion coefficient), and K_p (permeability coefficient). The values for J and t_{lag} can be obtained from the slope and interception of the time-axis graph of Q_{24}/A versus time, respectively. Similarly, the K_d and K_p can be calculated using the equations Eq. 12 and Eq. 13.

$$K_d = \frac{\text{Thickness of corneal tissue}^2 \ (h^2)}{6 \times t_{lag}} \qquad \text{Eq. 12}$$

$$K_p = \frac{J}{\text{Concentration of FLUZ in donor } (C_d)} \qquad \text{Eq. 13}$$

3.3.6 *Ex vivo* ocular permeation

In this study, a MEs-FLUZ-loaded two-layer dissolving MNs was applied to the cornea of whole porcine eyeballs, which were used within 2 h after collecting from a slaughterhouse. The effectiveness of this MNs formulation was

compared with FLUZ suspension-loaded one-layer dissolving MNs. To mimic the intraocular pressure, a catheter connected to a bottle of Hank's Balanced Salt solution was inserted into the vitreous chamber via the optic nerve, and a bottle was placed at the height of approximately 5 cm from the experimental area. After the MNs were applied, the porcine eyeballs were wrapped with tissue paper, soaked in PBS, and kept at 37 °C in an incubator. Samples (300 μL) were collected from the aqueous humor behind the cornea at 0, 0.5, 1, 2, 4, 6, and 8 hours using a 27G hypodermic needle and syringe. The amount of FLUZ was analyzed by HPLC. The data were plotted as the percent of drug permeation over 8 h versus time.

Following the ocular permeation study, the corneal tissues were cleansed using PBS (pH 7.4) and then sliced into small pieces using surgical scissors. These pieces were homogenized using a probe sonicator (60 Hz) in 5 mL of methanol for 20 min. The solution containing the small pieces of corneal tissues was then centrifuged at 4000 rpm for 20 min. The resulting supernatant was analyzed using HPLC. The percentage of FLUZ retained in the corneal tissues was calculated using Eq. 14.

$$\%FLUZ \text{ remaining in tissue} = \frac{\text{Amount of FLUZ in corneal tissue}}{\text{Amount of FLUZ-loaded}} \times 100 \quad \text{Eq. 14}$$

3.3.7 Antifungal activity

3.3.7.1 Agar disc diffusion method

The antifungal activity of the MEs-FLUZ-loaded two-layer dissolving MNs was studied against *Candida albicans* (ATCC 10231), which is associated with fungal keratitis. In the agar disc diffusion method, 1 mL of activated fungal growth (3 x 10^7 CFU/mL, 1U OD_{600}) was spread on the sabouraud dextrose agar (SDA) plate. The MEs-FLUZ-loaded two-layer dissolving MNs was placed in the SDA plate with needles punctured downward the nutrient agar. The untreated fungal lawn was used as a negative control. The FLUZ suspension, eugenol, FLUZ in eugenol, optimal microemulsions, MEs-FLUZ, and two-layer dissolving MNs were studied. The

sterile discs were immersed in each positive control solution and placed on SDA plates. The treated fungal plates were incubated at 37 °C for 24 h. The diameter of the inhibition zone was measured after 24 h of incubation. The percentage of zone inhibition was subsequently calculated.

3.3.7.2 Infection of *ex vivo* porcine corneas and FLUZ treatment

For *ex-vivo* antifungal activity, excised porcine cornea was incubated in an antibiotic-free medium overnight at 37 °C before starting the experiment. The 50 µL of *Candida albicans* (3×10^7 CFU/mL, 1U OD_{600}) was injected using a 26-gauge needle in the corneal stroma and incubated in an antibiotic-free medium at 37 °C for 24 h. After 24 h, the cornea was rinsed with PBS (pH 7.4) and treated with FLUZ suspension, FLUZ in eugenol, MEs-FLUZ, and MEs-FLUZ-loaded two-layer dissolving MNs. The infected cornea, without any treatment, was used as a negative control. A sterile metal ring was placed on the infected cornea to fill 200 μL of liquid treatment formulations. The MEs-FLUZ-loaded two-layer dissolving MNs was inserted into the infected cornea. After 5 min of application, the formulations were withdrawn, and infected corneas were further incubated at 37 °C for 24 h. Afterward, the infected corneas were homogenized using a probe sonicator. The supernatants were serially diluted and spread onto SDA plates at 37°C for 24 h. The colonies were counted and calculated colony forming units per mL (CFU/mL) as described in Eq. 15.

$$\text{CFU/mL} = \frac{\text{Number of colonies}}{\text{Volume of culture plated}} \times \text{dilution factor} \qquad \text{Eq. 15}$$

3.3.8 Stability test

To evaluate the stability of the MEs-FLUZ-loaded two-layer dissolving MNs, they were packed into aluminum zipper pouch with silica gel and stored at 5 °C ± 3 °C, 25 °C ± 2 °C/60% RH ± 5 %RH, and 40 °C ± 2 °C/75% RH ± 5% RH for 6 months according to the ICH guideline section Q1A R2. In addition, the physical

appearance, mechanical strength, and %drug content were performed at 0, 1, 2, 3, and 6 months.

3.3.9 Statistical analysis

The results of each experiment were presented as means ± standard deviation (SD) and were performed in triplicate. The normality of the data was tested using the Anderson-Darling test. For comparing two groups, an independent two-sided t-test was utilized. Statistical analysis for the mechanical properties of MNs and *in vitro* ocular drug delivery was conducted using a one-way ANOVA test with post-hoc Tukey's test. In this study, the SPSS® software version 19 (SPSS Inc., Chicago, IL) was used. *P*-values below 0.05 were considered significant.
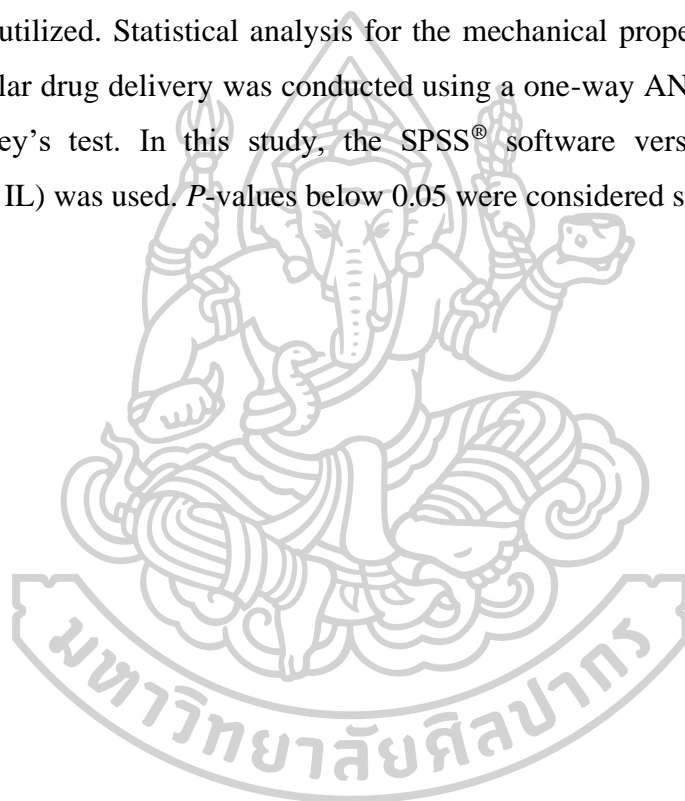
CHAPTER 4

RESULT AND DISCUSSION

4.1 Optimization of the outer layer of the two-layer dissolving MNs using 3-level factorial design

4.1.1 The physical appearance and mechanical strength of Chitosan and PVA

The relationship between the independent and dependent factors was described using a coded factors equation in significant terms, which was outlined in Eq. 16 - Eq. 17. Table 9 showed the results of ANOVA and regression analysis of the dependent factors. The linear model was used for mechanical strength, while the quadratic model was used for MNs height, with a p-value < 0.05 for optimal prediction. The suitability of the statistical model was assessed using the lack-of-fit expanding approach, which had a p-value > 0.05 for both dependent factors. The accuracy of the model was evaluated using R^2, which was found to be 0.8056 and 0.8923 for mechanical strength and MNs height, respectively.

$$\text{Mechanical strength} = 29.91 - 7.51\ X_1 + 4.15\ X_2 \qquad \text{Eq. 16}$$

$$\text{MNs height} = 587.40 - 36.57\ X_1 + 3.95\ X_2 - 26.32\ X_2^2 \qquad \text{Eq. 17}$$

Table 9: Summary of ANOVA and regression analysis

Responses	Fit Summary						
	Model	**p-value**	**Lack of fit**	**R^2**	**Adjusted R^2**	**Predicted R^2**	**Signal to noise**
Y_1	Linear	< 0.01	0.25	0.81	0.76	0.62	13.55
Y_2	Quadratic	< 0.01	0.14	0.89	0.89	0.85	14.44

Figure 25 illustrates the dependent factor and the significant impact of various mixing ratios of 3% chitosan and 20% PVA on the three-dimensional response surface area. The mechanical strength and MNs height were affected by changes in the ratio of 3% chitosan and 20% PVA. A decrease in the ratio of 3% chitosan and an increase in the ratio of 20% PVA led to a decrease in

MNs height and an increase in resistance force. However, when the ratio of 20% PVA was greater than 3, the MNs' height decreased. This phenomenon can be explained by the interaction between the positive charge of chitosan polysaccharide and the negative charge of PVA hydroxyl groups. An increase in the ratio of PVA resulted in greater polymer interaction and increased resistance force of the MNs. The MNs height was observed to decrease when the ratio of PVA in the formulation was increased, possibly due to the shrinkage of the PVA polymer caused by the non-interaction of hydroxyl groups with excess PVA.

Figure 25: The 3D response surface area of mechanical strength (A) and MNs height (B) of 3%Chitosan-20%PVA

Table 10 shows the optimization of MNs formulation, which was achieved through a combination of 3% chitosan and 20% PVA in a 1:4 ratio. The optimization criteria included desirability and *t*-test, both of which were found to be within acceptable ranges. A high desirability value between 0.8-1.0 indicated a strong correlation between predicted and actual values of dependent factors, while the *p*-value of a *t*-test of more than 0.05 was observed. The optimized MNs formulation resulted in high desirability and non-significant from the predicted value, suggesting that the regression model statistic could be used to predict output responses with appropriate input factors.

Table 10: Criteria for optimized MNs with desirability

Variables	Criteria	Predicted value	Actual value	Desirability	*t*-test
3% Chitosan	in range	1	1	0.83	-
20% PVA	in range	4	4	-	-
Mechanical strength	maximize	39.50 N	40.14±2.10 N	-	> 0.05
MNs height	maximize	619.31 µm	609.01±1.01 µm	-	> 0.05

4.1.2 The physical appearance and mechanical strength of Gantrez® S-97 and hyaluronic acid

The relationship between the independent and dependent factors was described using a coded factors equation in significant terms, which was outlined in Eq. 18. Table 11 shows the results of ANOVA and regression analysis for the dependent factors. The linear model was used for mechanical strength with a p-value < 0.05 for optimal prediction, while the mean was used for MNs' height (559.41 µm). The suitability of the statistical model was assessed using the lack-of-fit expanding approach, which had a p-value > 0.05 for mechanical strength. In the case of mechanical strength, the accuracy of the model was evaluated using R^2, which was found to be 0.7974.

$$\text{Mechanical strength} = 26.76 - 2.25\,X_1 + 3.85X_2 \qquad \text{Eq. 18}$$

Table 11: Summary of ANOVA and regression analysis

Responses	Fit Summary						
	Model	*p*-value	Lack of fit	R^2	Adjusted R^2	Predicted R^2	Signal to noise
Y_1	Linear	< 0.05	0.48	0.79	0.75	0.58	13.30
Y_2	Mean	< 0.05	-	-	-	-	-

Figure 26 illustrates the dependent factor and the significant impact of various mixing ratios of 30% Gantrez® S-97 and 5% HA on the three-dimensional response surface area. The mechanical strength was affected by changes in the ratio of 30% Gantrez® S-97 and 5% HA. An increase in the ratio of 30% Gantrez® S-97 and 5% HA led to an increase in mechanical strength. However, MNs' height not be affected by the concentration of

polymer. This phenomenon can be explained by the concentration of polymer when an increased amount of polymer affected to increase MNs hardness. Furthermore, the height of the MNs in every experiment did not show a significant change, possibly due to the absence of any shrinkage effect caused by the polymer.
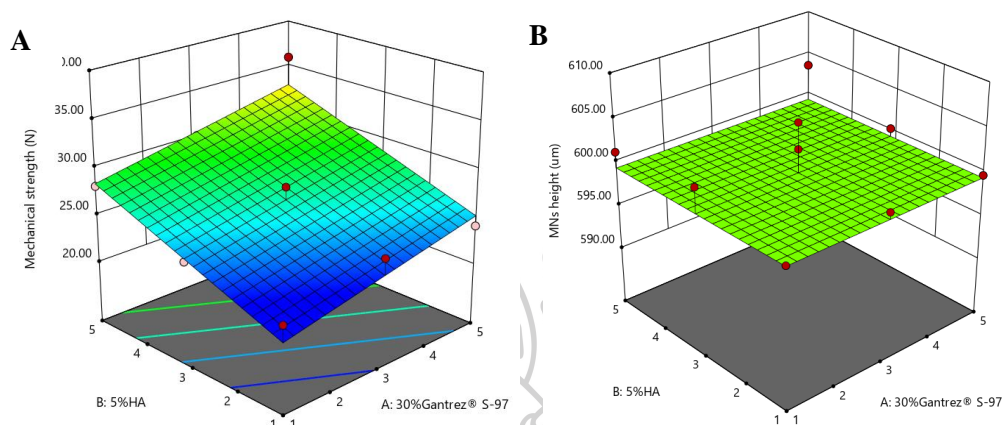
Figure 26: The 3D response surface area of mechanical strength (A) and MNs height (B) of 30% Gantrez® S-97-5% HA

Table 12 shows the optimization of MNs formulation, which was achieved through a combination of 30% Gantrez® S-97 and 5% HA in a 5:5 ratio. The optimization criteria, including desirability and t-test, were within acceptable ranges. A high desirability value between 0.8-1.0 indicated a strong correlation between predicted and actual values of dependent factors, while the p-value of a t-test of more than 0.05 was observed. The optimized MNs formulation resulted in high desirability and non-significant from the predicted value, suggesting that the regression model statistic could be used to predict output responses with appropriate input factors.

Table 12: Criteria for optimized MNs with desirability

Variables	Criteria	Predicted value	Actual value	Desirability	t-test
30% Gantrez® S-97	in range	5	5	0.69	-
5% HA	in range	5	5	-	-
Mechanical strength	maximize	32.86 N	31.11±0.91 N	-	> 0.05
MNs height	maximize	599.41 µm	600.13±0.31 µm	-	> 0.05

4.1.3 The physical appearance and mechanical strength of PVA and hyaluronic acid

The relationship between the independent and dependent factors was described using a coded factors equation in significant terms, which was outlined in Eq. 19 - Eq. 20. Table 13 shows the results of ANOVA and regression analysis for the dependent factors. The linear model was used for optimal mechanical strength and MNs height prediction with a p-value < 0.05. The suitability of the statistical model was assessed using the lack-of-fit expanding approach, which had a p-value > 0.05 for both dependent factors. The accuracy of the model was evaluated using R^2, which was found to be 0.8056 and 0.8923 for mechanical strength and MNs height, respectively.

$$\text{Mechanical strength} = 16.48 - 1.17\ X_1 + 3.91X_2 \qquad \text{Eq. 19}$$
$$\text{MNs height} = 567.00 - 24.74\ X_1 + 14.86\ X_2 \qquad \text{Eq. 20}$$

Table 13: Summary of ANOVA and regression analysis

Responses	Fit Summary						
	Model	p-value	Lack of fit	R^2	Adjusted R^2	Predicted R^2	Signal to noise
Y_1	Linear	< 0.05	0.26	0.74	0.68	0.49	10.18
Y_2	Linear	< 0.05	0.12	0.69	0.62	0.53	14.44

Figure 27 illustrates the dependent factor and the significant impact of various mixing ratios of 20% PVA and 5% HA on the three-dimensional response surface area. The mechanical strength and MNs height were affected by changes in the ratio of 20% PVA and 5% HA. A decrease in the ratio of 20% PVA and an increase in the ratio of 5% HA led to an increase in MNs height and mechanical strength. This phenomenon can be explained by the concentration of HA when an increased amount of HA affected to increase MNs hardness. Moreover, the MNs height and mechanical strength were observed to decrease when the ratio of PVA in the formulation was increased, possibly due to the shrinkage of PVA polymer caused by the non-interaction of hydroxyl groups with excess PVA.
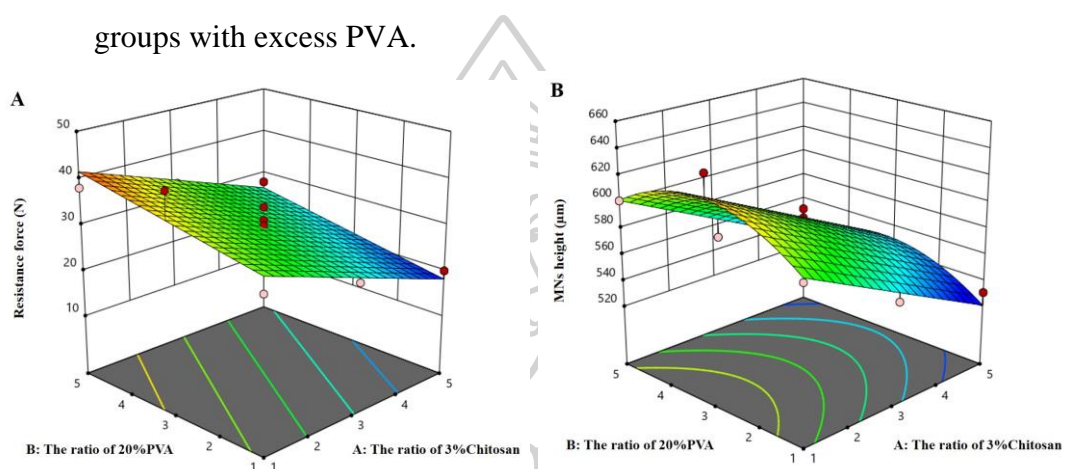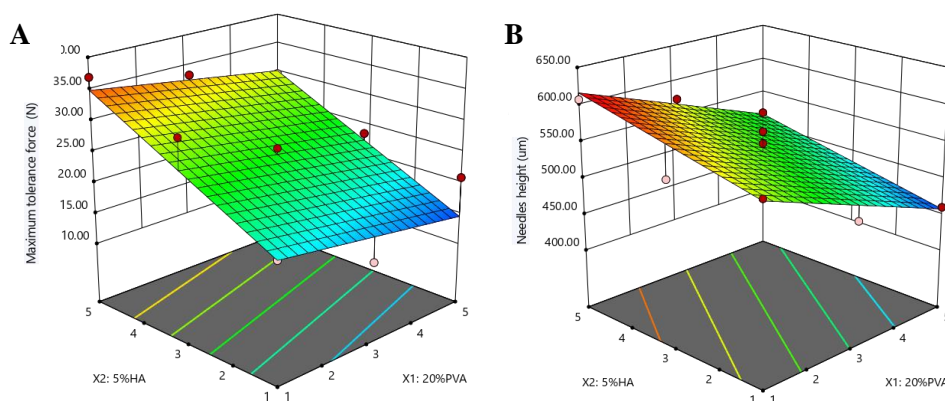
Figure   27: The 3D response surface area of mechanical strength (A) and MNs height (B) of 20%PVA-5%HA

Table 14 shows the optimization of MNs formulation, which was achieved through a combination of 20% PVA and 5% HA in a 1:5 ratio. The optimization criteria included desirability and t-test, both within acceptable ranges. A high desirability value between 0.8-1.0 indicated a strong correlation between predicted and actual values of dependent factors, while the p-value of a t-test of more than 0.05 was observed. The optimized MNs formulation resulted in high desirability and non-significant from the predicted value, suggesting that the regression model statistic could be used to predict output responses with appropriate input factors.

Table 14: Criteria for optimized MNs with desirability

Variables	Criteria	Predicted value	Actual value	Desirability	t-test
20% PVA	in range	1	1	0.95	-
5% HA	in range	5	5	-	-
Mechanical strength	maximize	34.85 N	33.70±0.30 N	-	> 0.05
MNs height	maximize	616.56 μm	601.23±1.01 μm	-	> 0.05

4.1.4 Selection of the optimal first layer of MNs

The first layer MNs optimization results showed that the optimal MNs formulation was 3%chitosan and 20%PVA at a weight ratio of 1:4. The physical appearance showed the conical shape of MNs with an average of

601.23±1.01 µm in height and the highest mechanical strength of 33.70±0.30 N was observed, as represents in Table 15.

Table 15: Selection of the optimal first layer of MNs from DoE

Formulation	Optimal weight ratio	Mechanical strength (N)	MNs height (µm)
3%Chitosan + 20%PVA	1:4	40.14±2.10	609.01±1.01
30% Gantrez® S-97 + 5%HA	5:5	31.11±0.91	600.13±0.31
20% PVA + 5% HA	1:5	33.70±0.30	601.23±1.01

4.2 Design and formulation of optimal MEs-FLUZ

4.2.1 Solubility of FLUZ in various oils, surfactants, and cosurfactants

The solubility results of FLUZ in various oils, surfactants, and co-surfactants are shown in Table 16. Oil was an important component in the microemulsion which increased the solubility and improved ocular drug delivery by increased flexibility of ocular barriers such as epithelium. FLUZ exhibited the highest solubility of 198.92 ± 11.21 mg/mL in eugenol among the various oils tested. Likewise, surfactants acted as thin films forming at the interface, decreasing the particle size and stabilizing the microemulsion. Moreover, it enhanced ocular permeation activity by partitioning into the ocular barrier and disrupted the structural organization of an ocular lipid barrier, epithelium. Among the surfactant investigated, FLUZ presented the highest solubility of 45.96 ± 2.03 mg/mL in Tween 80. Lastly, the co-surfactant increased the interfacial fluidity, enabling the spontaneous emulsion by creating void spaces between the interface for water penetration (104). The FLUZ presented the highest solubility of 88.52 ± 2.00 mg/mL in ethanol among the co-surfactant determined. Thus, creating a ternary phase diagram, eugenol, Tween 80, and ethanol were selected to formulate microemulsions based on the solubility.

Table 16: Results of solubility studies on FLUZ in various oils, surfactants, and co-surfactants

Solvent	Solubility (mg/mL)	Solvent	Solubility (mg/mL)
Types of solvent: Oils		**Types of solvent: Surfactants**	
Eugenol*	**198.92 ± 11.21**	Tween 20	20.81 ± 2.66
Oleic acid	52.17 ± 0.42	**Tween 80***	**45.96 ± 2.03**
IPM	18.76 ± 4.03	Span 20	21.07 ± 0.26
Peppermint oil	9.35 ± 2.30	Span 80	31.27 ± 0.48
Limonene	9.15 ± 5.00	Cremophor RH40	7.73 ± 1.15
MC-TG	5.00 ± 2.26	Labrasol®	34.90 ± 2.50
Orange oil	13.60 ± 0.68	Labrafac™ PG	8.27 ± 5.15
Wintergreen oil	23.47 ± 0.18		
Types of solvent: Co-Surfactants			
Ethanol*	**88.52 ± 2.00**		
PEG 400	64.29 ± 4.04		
Propylene glycol	39.85 ± 2.85		
Glycerol	39.26 ± 0.33		

4.2.2 Construction of pseudo-ternary phase diagram

To determine the translucent region of microemulsion, pseudo-ternary phase diagrams were constructed. Figure 28 illustrates four diagrams of microemulsion with different S_{mix} weight ratios. The largest region of translucent microemulsion region was found at a S_{mix} ratio of 3:1, approximately 40.48% of the total area. The four pseudo-ternary phase diagram results indicated that increasing the surfactant weight ratio could expand the translucent microemulsion region because increasing the surfactant could increase the interfacial fluidity and reduce the surface tension of oil and water.
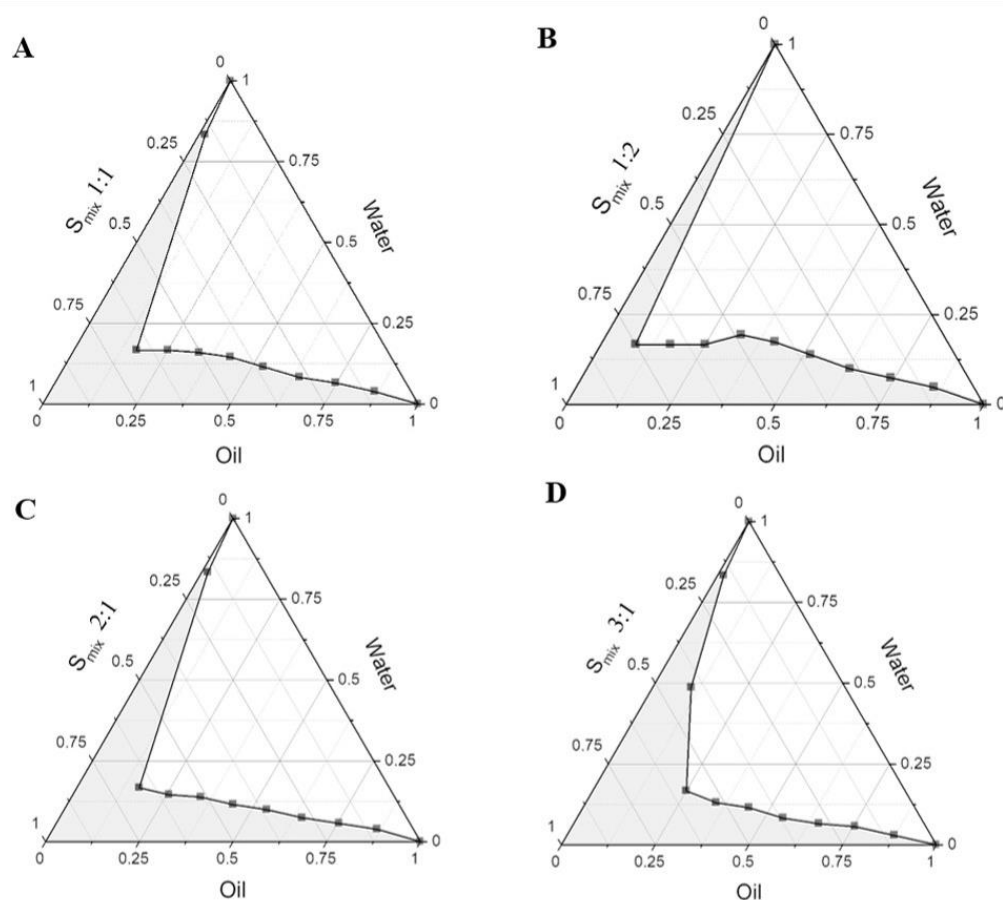
Figure 28: Pseudo-ternary phase diagram of microemulsion (eugenol, Tween 80, and PEG400) containing various S_{mix} weight ratios: (A) S_{mix} 1:1 with 33.43% of the total area; (B) S_{mix} 1:2 with area 31.98% of the total area; (C) S_{mix} 2:1 with area 34.35% of the total area, and (D) S_{mix} 3:1 with area 40.48% of the total area

4.2.3 Optimization of MEs-FLUZ

Table 17 presents the dependent factors, including droplet size (Y_1), PDI (Y_2), drug content (Y_3), and % drug permeation at 8 h (Y_4), resulting from the optimization of the component proportion of selected MEs (S_{mix} ratio 3:1). To study the statistical effects, interactions, and optimization of MEs, an I-optimal mixture design was chosen, which comprised of 14 experimental batches with varying levels of oil (6.25%-25%), S_{mix} (66.25%-87.50%), and water (6.25%-25%).

Table 17: All experimental formulations of MEs-FLUZ using I-optimal mixture design

Formulations	Independent factors				Dependent factors		
	A: Oil (%w/w)	B: S$_{mix}$ (%w/w)	C: Water (%w/w)	Size (nm)	PDI	Drug content (mg/mL)	%Permeation at 8 h
1	16.89	66.25	16.86	635.03	0.42	41.82	1.86
2	15.33	77.60	7.06	603.20	0.61	64.08	1.37
3	6.63	68.38	25.00	625.80	0.62	31.67	0.63
4	7.04	77.39	15.57	668.00	0.65	28.43	0.66
5	25.00	68.33	6.67	970.83	0.95	90.28	1.36
6	21.61	66.25	12.14	179.13	0.30	87.92	1.64
7	16.89	66.25	16.86	634.37	0.60	71.31	2.08
8	15.33	77.60	7.06	725.70	0.58	63.08	1.09
9	7.04	77.39	15.57	522.10	0.79	26.53	1.15
10	6.25	82.57	11.18	577.00	0.68	38.72	0.44
11	6.25	87.50	6.25	504.80	0.56	42.10	0.81
12	10.55	70.72	18.73	632.97	0.50	46.38	0.97
13	15.01	72.36	12.63	505.47	0.77	42.90	1.91
14	11.05	82.70	6.25	1322.67	0.72	58.55	1.28

Analysis of variance (ANOVA) was used to calculate the significance level and to validate the design model. It can expand the effects of each independent factor component on the dependent factors. The results are shown in Table 18-21. The globule size of MEs-FLUZ was around 179.13 to 1322.67 nm. The relationship between independent and dependent factors was described in significant terms of the coded equation as Eq.21. The ANOVA analysis of size showed significance with p-value < 0.05 in the cubic statistical model, as shown in Table 18. Moreover, lack-of-fit that is suitable for the statistical model represented the well-fitting statistical model with a p-value of 0.12. In the case of the regression coefficient, R^2, adjusted, and predicted R^2 values of the droplet size were reasonable at 0.85, 0.71, and 0.69, respectively, indicating the suitability of the suggested statistical model.

Droplet size = 1966.12A + 547.26B + 470.59C - 2159.85AB - 2478.86AC - 7564.57AB(A-B)-8613.86AC(A-C)   Eq. 21

The droplet size of MEs-FLUZ analysis from a 2D contour plot and 3D response surface area represented in Figures 29A and 29B illustrated the trend of globule size. When the ratio of oil increased with the decreasing ratio of Smix and water, the globule size of MEs decreased in the appropriate ratio range (dark blue color). Likewise, the mathematical coded equation (Eq. 21) was used to predict droplet size response, which showed a significant of 2 factors interaction (AB, AC, AB(A-B) and AC(A-C)) with negative signs in front of coefficient factors that referred the inversion of the relationship between independent and dependent factors. Thus, the appropriate ratio of S_{mix} and water in oil interfaces could help disrupt the transient interfacial tension and reduce MEs size (168).

Table 18: ANOVA analysis of globule size (Y_1)

Source	Sum of squares	Degree of freedom	Mean square	F-value	p-value	Inference
Cubic Model	719923.94	6	119987.32	6.44	< 0.05	Significant
Linear Mixture	88025.52	2	44012.76	2.36	0.16	
AB	116665.06	1	116665.06	6.26	< 0.05	
AC	203989.12	1	203989.12	10.95	< 0.05	
AB(A-B)	308463.92	1	308463.92	16.55	< 0.05	
AC(A-C)	371682.67	1	371682.67	19.94	< 0.05	
Residual	130451.63	7	18635.95			
Lack of Fit	112304.88	4	28076.22	4.64	0.12	Not significant
Pure Error	18146.75	3	6048.92			
Cor Total	850375.56	13				

Regression coefficient: $R^2 = 0.85$, Adjusted $R^2 = 0.71$, Predicted $R^2 = 0.69$

The PDI of MEs-FLUZ was found in a range of 0.30 to 0.95. PDI was used to measure the broadness of molecular weight distribution. The larger PDI (not more than 1) that was affected the variety of molecular weight. The appropriated PDI of MEs should not be more than 0.30 (169). The statistical model of PDI showed non any suitable model for explanation and prediction between independent and dependent factors (p-value > 0.05), as shown in Table 19. Moreover, this ANOVA analysis of PDI showed low R^2, adjusted R^2, and predicted R^2 values suggesting this model was inappropriate for the prediction of MEs optimization.

Table 19: ANOVA analysis of PDI (Y_2)

Source	Sum of squares	Degree of freedom	Mean square	F-value	p-value	Inference
Model	0.14	3	0.05	2.28	0.14	not significant
Linear Mixture	0.03	2	0.01	0.63	0.55	
AC	0.11	1	0.11	5.58	0.04	
Residual	0.20	10	0.02			
Lack of Fit	0.17	7	0.02	2.61	0.23	not significant
Pure Error	0.03	3	0.01			
Cor Total	0.34	13				
Regression coefficient: R^2 = 0.41, Adjusted R^2 = 0.23, Predicted R^2 = -0.63						

The drug content of MEs-FLUZ was found to be approximately 26.53 to 90.28 mg/mL. The relationship between independent and dependent factors was described in effective terms of the coded equation as shown in Eq. 22. The linear statistical model of drug content was significant (p-value < 0.05) with suitable lack-of-fit (p-value > 0.05), R^2 (0.81), adjusted R^2 (0.78), and predicted R^2 (0.72) values, according to the ANOVA analysis results (Table 20).

$$\text{Drug content} = 97.96A + 39.61B + 21.45C \qquad \text{Eq. 22}$$

The drug content of MEs-FLUZ analysis from a 2D contour plot and 3D response surface area are represented in Figures 29C and 29D. The result found that the drug content was increased linearly (red color) when the oil concentration was increased. On the other hand, while S_{mix} and water decreased, the drug content decreased. Moreover, the mathematical coded equation (Eq. 22), which is used to predict drug content response, showed significant factors (A, B, and C) with an increasing amount of coefficient (positive sign) that expanded the concentration of oil, S_{mix} and, water could increase the amount of FLUZ, respectively.

Table 20: ANOVA analysis of drug content (Y$_3$)

Source	Sum of squares	Degree of freedom	Mean square	F-value	*p*-value	Inference
Linear Model	4517.74	2	2258.87	24.12	< 0.0001	significant
Linear Mixture	4517.74	2	2258.87	24.12	< 0.0001	
Residual	1029.96	11	93.63			
Lack of Fit	592.81	8	74.10	0.51	0.80	not significant
Pure Error	437.14	3	145.71			
Cor Total	5547.70	13				
Regression coefficient: R^2 = 0.81, Adjusted R^2 = 0.78, Predicted R^2 = 0.72						

Finally, the percentage permeation over 8 h of MEs-FLUZ was 0.44 to 2.08%. The relationship between independent factors and dependent factors was described in significant terms of the coded equation of Eq. 23. The results of the ANOVA analysis (Table 21) revealed that a mathematical quadratic model predicting the percentage permeation over 8 h of MEs-FLUZ was statistically significant (*p*-value < 0.05) and suitable fitting statistical model (lack-of-fit, *p*-value > 0.05). Furthermore, The R^2, adjusted R^2, and predicted R^2 values that were 0.77, 0.70, and 0.63, respectively, were reasonable, indicating the statistical model's goodness

$$\%\text{Permeation at 8 h} = 1.44A + 0.92B + 0.47C + 3.81AC \qquad \text{Eq. 23}$$

The percentage permeation over 8 h of MEs-FLUZ analysis from a 2D contour plot and 3D response surface area is presented in Figures 29E and 29F. The results found that when the ratio of oil and water increased, the percentage permeation over 8 h of MEs-FLUZ was increased (red color). This effect could be expanded by the multi-layered structure of the cornea. From anterior to posterior, there is the epithelium, Bowman's layer, stroma, Descemet's membrane, and endothelium, which stroma is a hydrophilic barrier nature affects the transport of water-soluble molecules into the cornea. On the other hand, the other structures are the barriers of lipoidal nature, allowing the hydrophilic molecules can pass this structure (31). Thus, microemulsions that were composed of oil and water can undergo this multi-layered cornea structure. Moreover, surfactants and co-surfactant could improve the fluidity of the cornea barrier. The mathematical coded equation (Eq. 23), used to predict the percentage permeation over 8 h, showed significant factors (A, B, C, and AC), which increasing coefficient factor of A, B, and C could improve the percentage permeation over 8 h, respectively. Moreover, the two-factor interaction of AC could increase the percentage permeation over 8 h more than other factors (red color).

Table 21: ANOVA analysis of %Permeation at 8 h (Y_4)

Source	Sum of squares	Degree of freedom	Mean square	F-value	p-value	Inference
Quadratic Model	2.60	3	0.87	11.15	0.0016	significant
Linear Mixture	1.81	2	0.90	11.62	0.0025	
AC	0.79	1	0.79	10.20	0.0096	
Residual	0.78	10	0.08			
Lack of Fit	0.59	7	0.08	1.38	0.4305	not significant
Pure Error	0.18	3	0.06			
Cor Total	3.38	13				
Regression coefficient: $R^2 = 0.77$, Adjusted $R^2 = 0.70$, Predicted $R^2 = 0.63$						

A

A: Oil (%)
27.50

6.25 ... 66.25

87.50 ... 6.25 ... 27.50
B: Smix (%) ... C: Water (%)

Size (nm)

B

Size (nm)

C (27.50) ... (6.25) ... B (87.50)

B (66.25)

C (6.25)

A (27.50)

C

A: Oil (%)
27.50

6.25 ... 66.25

87.50 ... 6.25 ... 27.50
B: Smix (%) ... C: Water (%)

Drug content (mg/ml)

D

Drug content (mg/ml)

A (27.50)

C (6.25)

C (27.50)

A (6.25)

B (87.50)
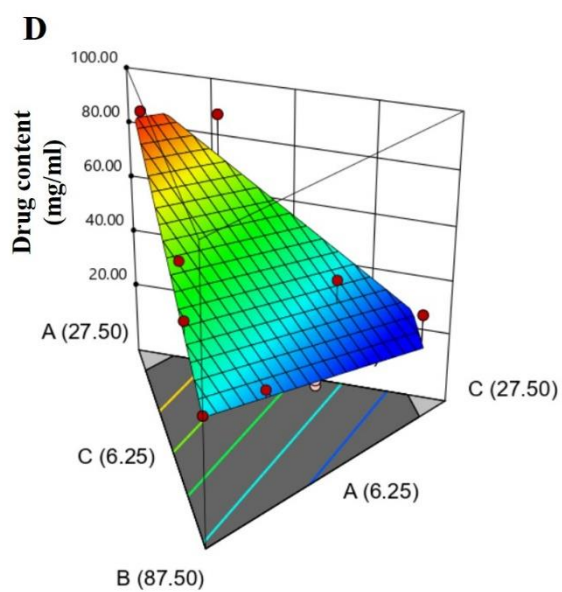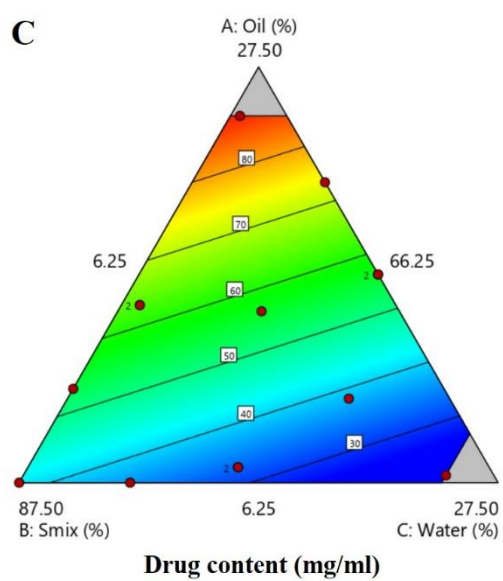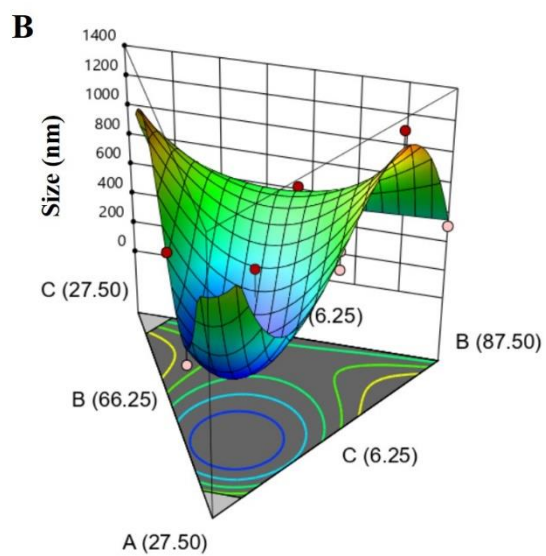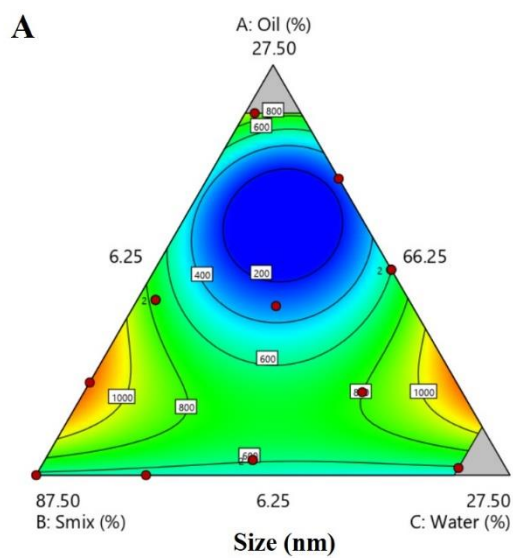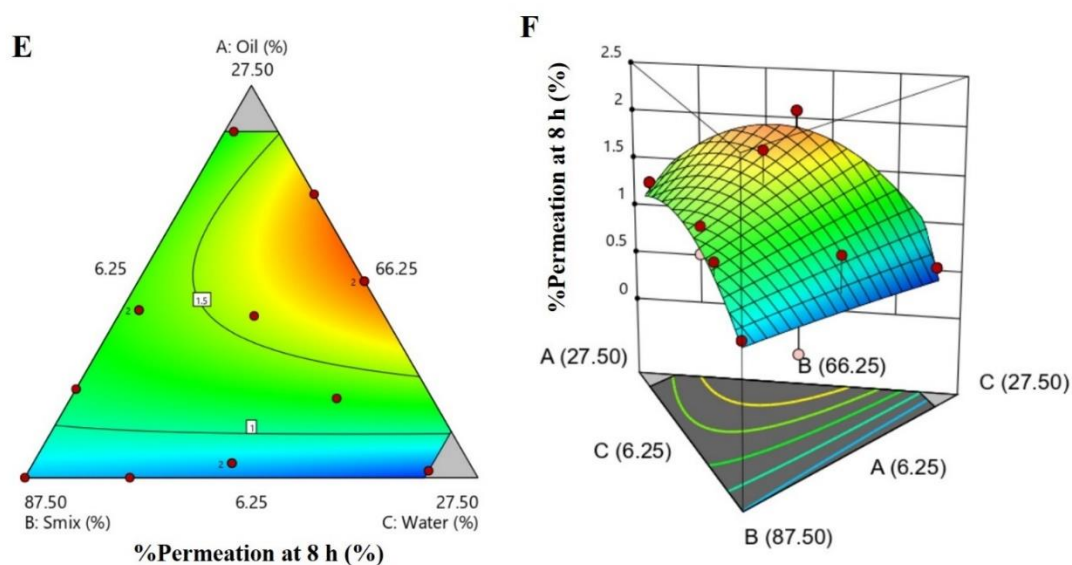
Figure 29: 2D contour plot and 3D response surface area of (A), (B): globule size; (C), (D): drug content; and (E), (F): %Permeation at 8 h of MEs-FLUZ formulations

The Design-Expert® version 11 software was used to analyze data for optimizing MEs-FLUZ formulations, as presented in Table 22. The optimal formulation consisted of 20.546% oil (eugenol), 67.70% S_{mix} (Tween80:PEG400 = 3:1), and 11.76% water, desirability 0.83. The desirability metric evaluated multi-response optimization value and ranges from 0 to 1, where 1 represented the ideal value and 0 indicated an unacceptable value. A desirability between 0.8 and 1 represented good quality. The selected model of MEs-FLUZ formulations was reliable, as shown in Table 23, with no significant difference between the predicted and actual values of dependent factors, confirmed through a *t*-test.

Table 22: Criteria for optimized MEs-FLUZ

Factors	Criteria	Optimization	Desirability
A: Oil (%w/w)	is in range	20.54 %w/w	0.83
B: S_{mix} (%w/w)	is in range	67.70 %w/w	
C: Water (%w/w)	is in range	11.76 %w/w	
Size (nm)	Minimize	119.85 nm	
PDI	none		
Drug content (mg/mL)	Maximize	74.13 mg/mL	
%Permeation at 8h (%)	Maximize	1.78%	

Table 23: Predicted value and actual value of dependent factors from optimized MEs-FLUZ

Results	Dependent factors		
	Size (nm)	Drug content (mg/mL)	%Permeation at 8h
Predicted value	119.85 ± 0.00	74.13 ± 0.00	1.78 ± 0.00
Actual value	121.22 ± 9.01	73.58 ± 0.54	1.57 ± 0.22
t-test (*p*-value)	0.81	0.15	0.17

4.3 Characterization of MEs-FLUZ

4.3.1 Globule size, PDI, and zeta potential measurement

The optimized MEs-FLUZ was characterized by globule size, PDI, and zeta potential, with a suitable size of 121.22 ± 9.01 nm, PDI of 0.30 ± 0.02, and neutral zeta potential of 0.012 ± 0.001 mV. This optimal microemulsion possessed an appropriate average globule size and PDI that could pass through the gap junction of the cornea barrier. Moreover, this optimal microemulsion might be presented high physical stability and not be entrapped in the cornea from the positive charge (31).

4.3.2 pH value

The optimized MEs-FLUZ was characterized on pH, with desirable pH of 6.91 ± 0.10. The pH of optimal microemulsion showed suitable to apply on ocular tissue was 7.11±1.5 (170).

4.3.3 Centrifugation test

Following the centrifugation test, it was observed that the optimal formulation of microemulsion remained physically stable and did not exhibit any phase separation.

4.3.4 Drug content

The amount of MEs-FLUZ was quantified to confirm the dosage accuracy and reproducibility. The drug content was 73.58 ± 0.54 mg/mL.

4.4 Characterization of MEs-FLUZ-loaded two-layer dissolving MNs

4.4.1 The physical appearance of two-layer dissolving MNs

Under the scanning electron microscope, the physical appearance of MEs-FLUZ-loaded two-layered dissolving MNs revealed sharp conical-shaped needle tips (11x11 array) with a patch size of 1x1 mm^2, as shown in Figure 30A. Individual needle measurements of MEs-FLUZ-loaded two-layered dissolving MNs were obtained at 130x magnification, with 581.83±10.58 μm needles height, 300.03±1.51 μm base width, and 300.10±0.12 μm interspacing, as shown in Figure 30B. The morphology of the MNs was suitable for minimal invasion penetration into the cornea barrier due to the approximate thickness of the cornea being 500 μm. Furthermore, as shown in Figure 31, confocal fluorescence images confirmed that the polymer mixture film of outer layer MNs loaded with FS (water phase) effectively encapsulates the MEs-FLUZ of inner layers MNs loaded with rhodamine b (oil phase).
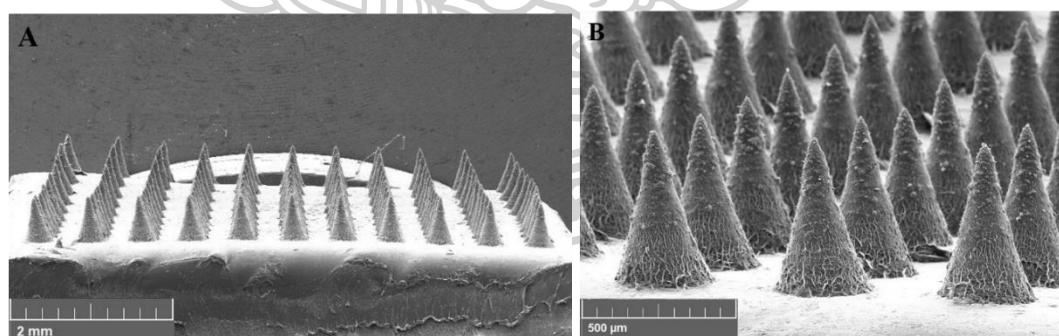
Figure 30: SEM images of the MEs-FLUZ-loaded two-layered dissolving MNs loaded with at 30x (A) and 130x (B) magnifications.

500.00 μm
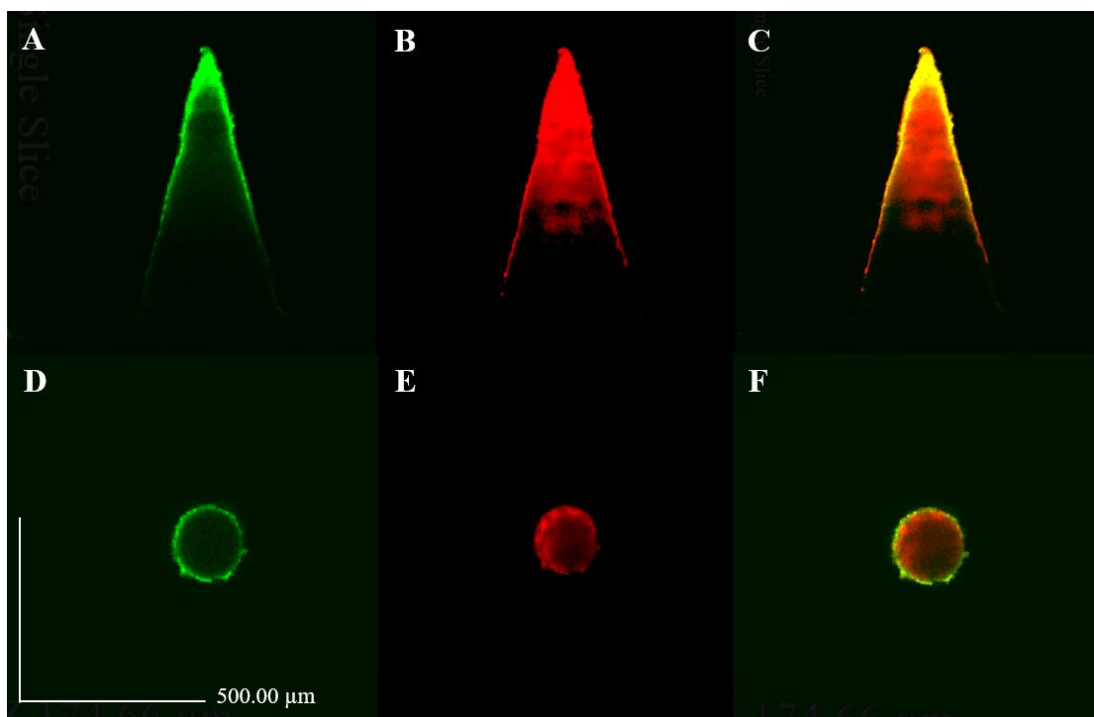
Figure 31: The confocal images of MEs-FLUZ-loaded two-layered dissolving MNs (side and top views) of (A) and (D) displayed only the outer layer loaded with FS (green color); (B) and (E) showed only the inner layer loaded with rhodamine b (red color); and (C) and (F) displayed both the outer and inner layers.

4.4.2 The mechanical properties of two-layer dissolving MNs
4.4.2.1 Mechanical strength

A compression test assessed the mechanical strength of MEs-FLUZ-loaded two-layered dissolving MNs. The ability of MNs to withstand applied forces and penetrate the cornea was a crucial characteristic. Figure 32 illustrates the mechanical strength of MNs using a texture analyzer. The polymer mixture of the first layer was 3% chitosan and 20% PVA at a weight ratio of 1:4, which covers the second layer. The two-layered dissolving MNs exhibited a mechanical strength of approximately 20.85 ± 1.09 N and 21.57 ± 1.04 N with and without MEs-FLUZ loading. The results indicated that incorporating MEs-FLUZ (1.27%w/w) into the inner layer did not

significantly change the mechanical strength of the two-layered dissolving MNs.
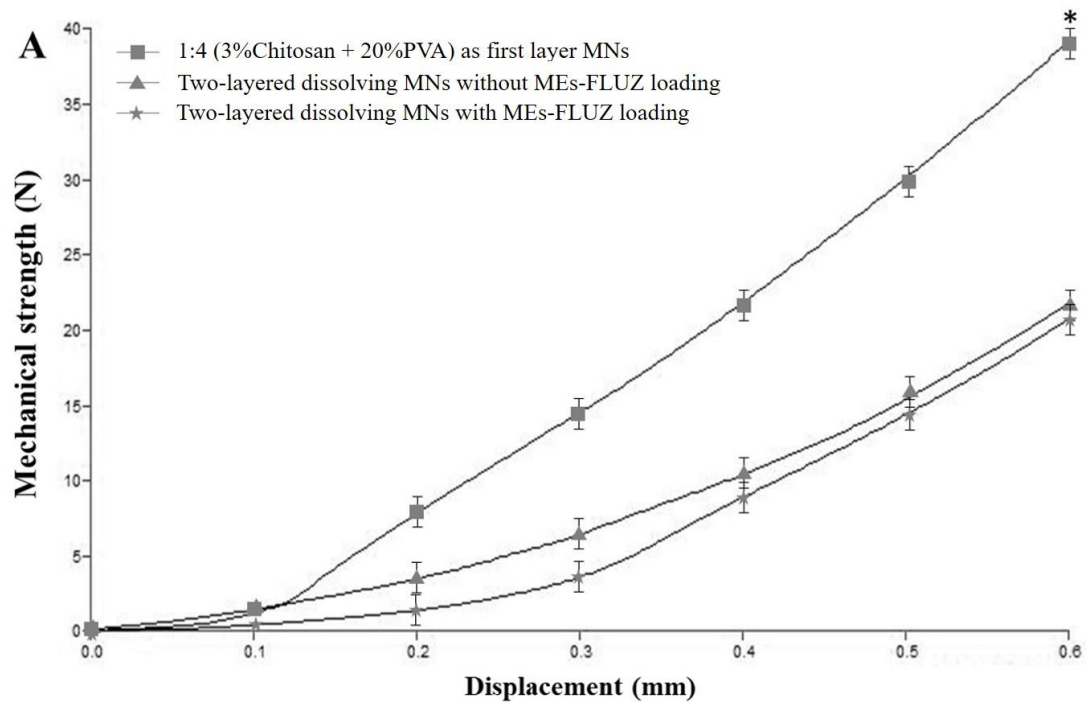
Figure 32: Mechanical strength of 1:4 (3%Chitosan + 20%PVA) as first layer MNs (■), two-layered dissolving MNs without MEs-FLUZ loading (▲) and two-layered dissolving MNs with MEs-FLUZ loading (★). * $p < 0.05$ compared to other groups

4.4.2.2 Insertion force

The estimated insertion force required for completing insertion into the cornea at around 600 µm was 5.70±0.51 N/121 array or 0.05 N per needle in the control group and 5.18±0.49 N/121 array or 0.04 N per needle in the optimal formulation, as shown in Figure 33. Other studies that examined insertion using 40% PVP dissolving MNs (115), 15% PVP/15% PVA dissolving MNs (26), and methacrylate hyaluronic acid/hyaluronic acid double layer MNs (118) found that the average insertion forces required to complete insertion into the cornea were 0.15, 1.04, and 0.05 N per needle, respectively.

Therefore, the MEs-FLUZ-loaded two-layered dissolving MNs were suitable as an ocular device patch with minimally invasive corneal tissue.
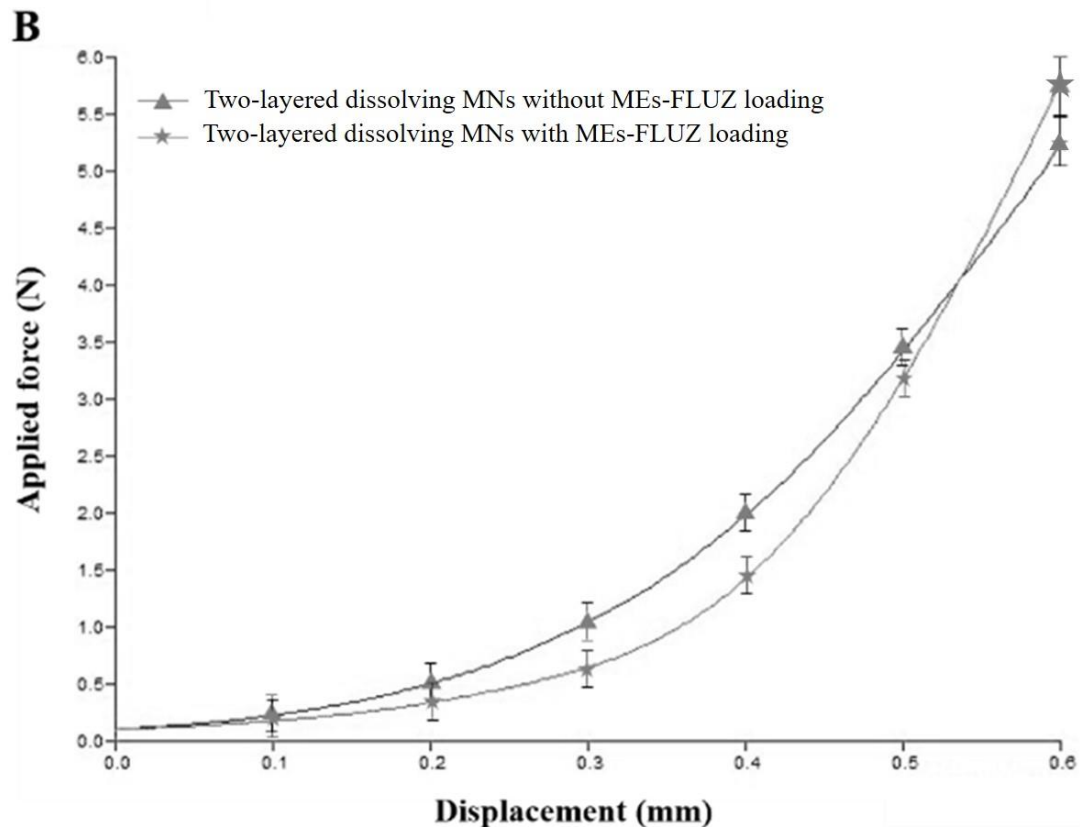
Figure 33: The insertion force of two-layered dissolving MNs without MEs-FLUZ loading (▲) and two-layered dissolving MNs with MEs-FLUZ loading (★)

4.4.2.3 Percentage of complete insertion

In order to achieve successful ocular drug delivery, the complete insertion of MNs was tested to overcome the cornea barrier. However, due to the difficulty of observing visible dots on cornea tissue, complete insertion was determined on an artificial membrane (Parafilm M®) with the same thickness as the corneal tissue. After applying MEs-FLUZ-loaded two-layered dissolving MNs with an insertion force of 5.70±0.51 N/121 array, completed insertion (100%), was observed in 5 layers of artificial membrane, which had a total thickness of 650 µm (with each thickness layer of approximately 130

µm), as shown in Figure 34A-30E. The ability of the MNs to penetrate each layer and the percentage of complete insertion is presented in Figure 34F. The first and second layers showed 100% complete insertion, while the third and fourth layers exhibited 85.00±5.00% and 28.33%±7.64% complete insertion, respectively. The last layer showed no penetration achieved. The MEs-FLUZ-loaded two-layered dissolving MNs were able to penetrate up to the four layers of an artificial membrane. Based on this result, it was estimated that the MNs could penetrate up to a depth of 520 µm in an artificial corneal membrane with a corneal thickness ranging from 500-800 µm (31).
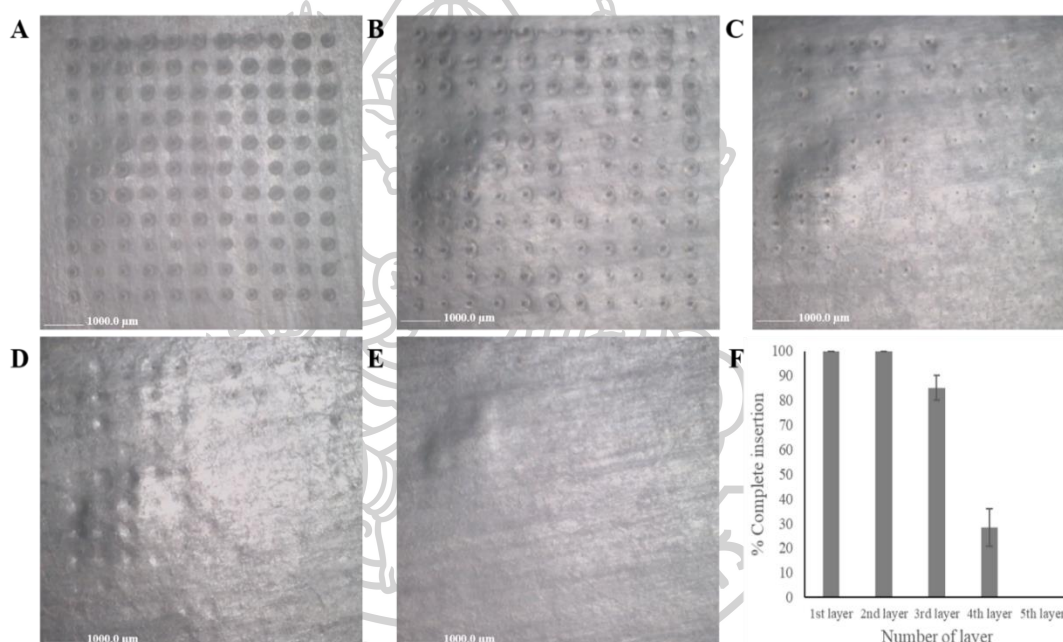
Figure 34: The images of complete insertion into Parafilm M® of MEs-FLUZ-loaded two-layered dissolving MNs; (A) first layer, (B) second layer, (C) third layer, (D) fourth layer, and (E) fifth layer (F) Percentage of complete insertion versus the number of layers by maximum applied force (5.70±0.51 N/121 array)

4.4.2.4 Insertion depth

FS-loaded two-layered MNs were applied to porcine corneal tissues to validate insertion depth, and the insertion depth was observed under a fluorescence microscope and CLSM. Figures 35 and 36 show the bright field

and fluorescence images of the damaged MNs in the corneal tissue. The insertion depth was found to be 213.70 ± 10.65 μm. The CLSM images illustrated the depth of each layer, from the surface (0 μm) to a depth of 271.10 μm after applying the MEs-FLUZ-loaded two-layered dissolving MNs. The dark areas in the corneal tissue indicated a lack of fluorescence. The result in insertion depth of the artificial membrane and the corneal tissue could be slightly different due to the corneal tissue's highly resistant and elastic structure, which may cause deformation of MNs. Nevertheless, the results indicated that the MEs-FLUZ-loaded two-layered dissolving MNs successfully penetrated the corneal tissue and created micro-channels for delivering FLUZ into the corneal tissue.
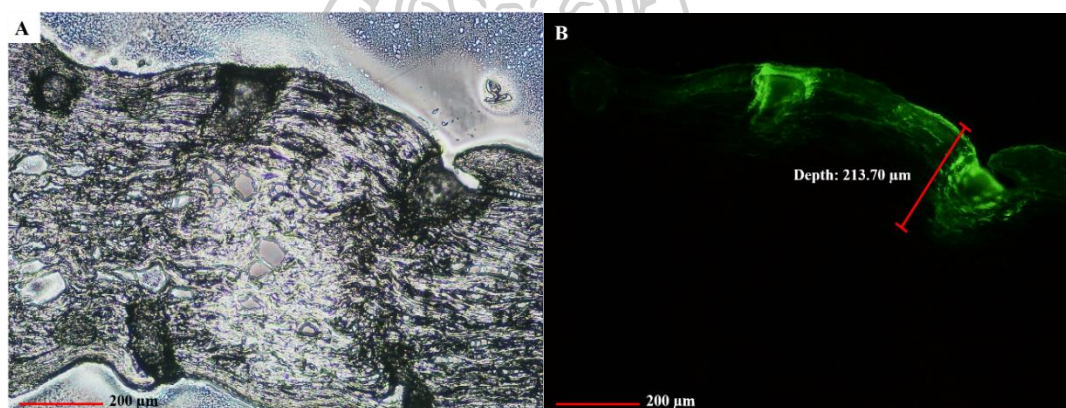
Figure 35: The corneal tissue's insertion depth of MEs-FLUZ-loaded two-layered dissolving MNs was observed through a bright field (A) and a fluorescence (B) captured using a 10x objective lens (bar = 200 μm)
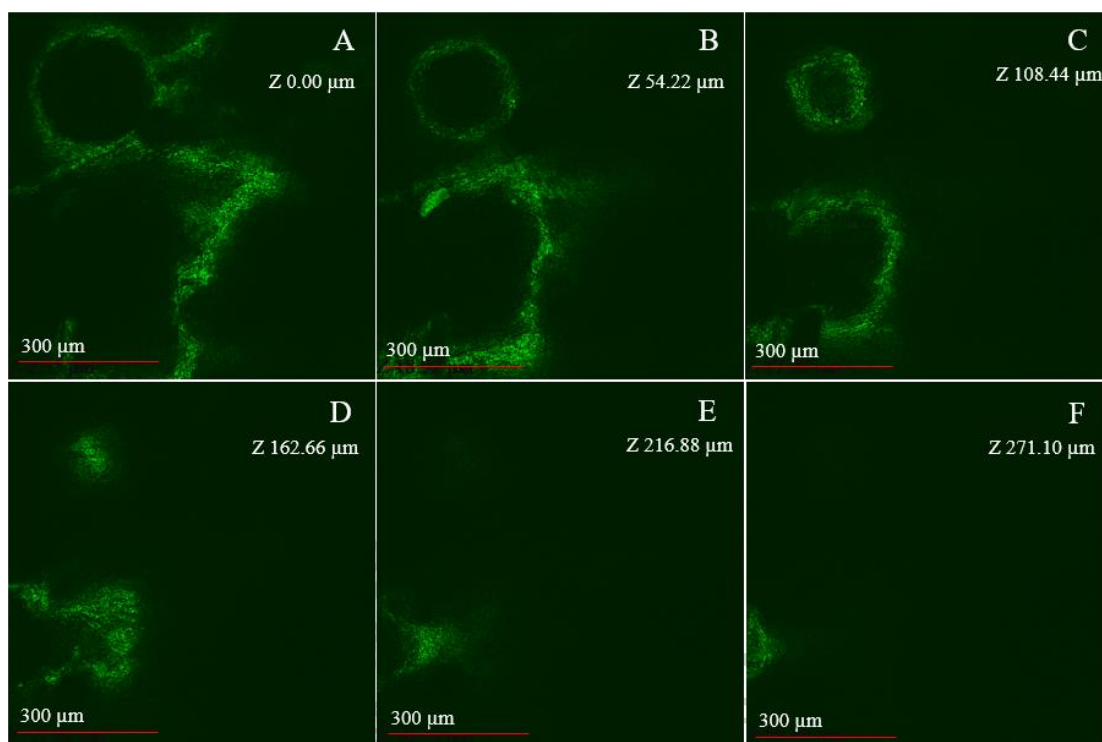
Figure 36: The CLSM images show the insertion of MEs-FLUZ-loaded two-layered dissolving MNs in corneal tissues, ranging from the cornea's surface of 0 μm (A), 54.22 μm (B), 108.44 μm (C), 162.66 μm (D), 216.88 μm (E), and 271.10 μm (F) inside the cornea tissue (bar = 300 µm)

4.4.3 Dissolution times

Design and development of dissolving MNs for the ocular application required testing their dissolution times, which were crucial to ensure optimal formulation. Fast dissolution times of dissolving MNs could potentially increase patient complaints. Figure 37 illustrates the complete dissolution of the MEs-FLUZ-loaded two-layered dissolving MNs within 3 min of application into the corneal tissue. These results demonstrated that the MNs formulation rapidly dissolved with an appropriate dissolution time upon application to the corneal tissue.
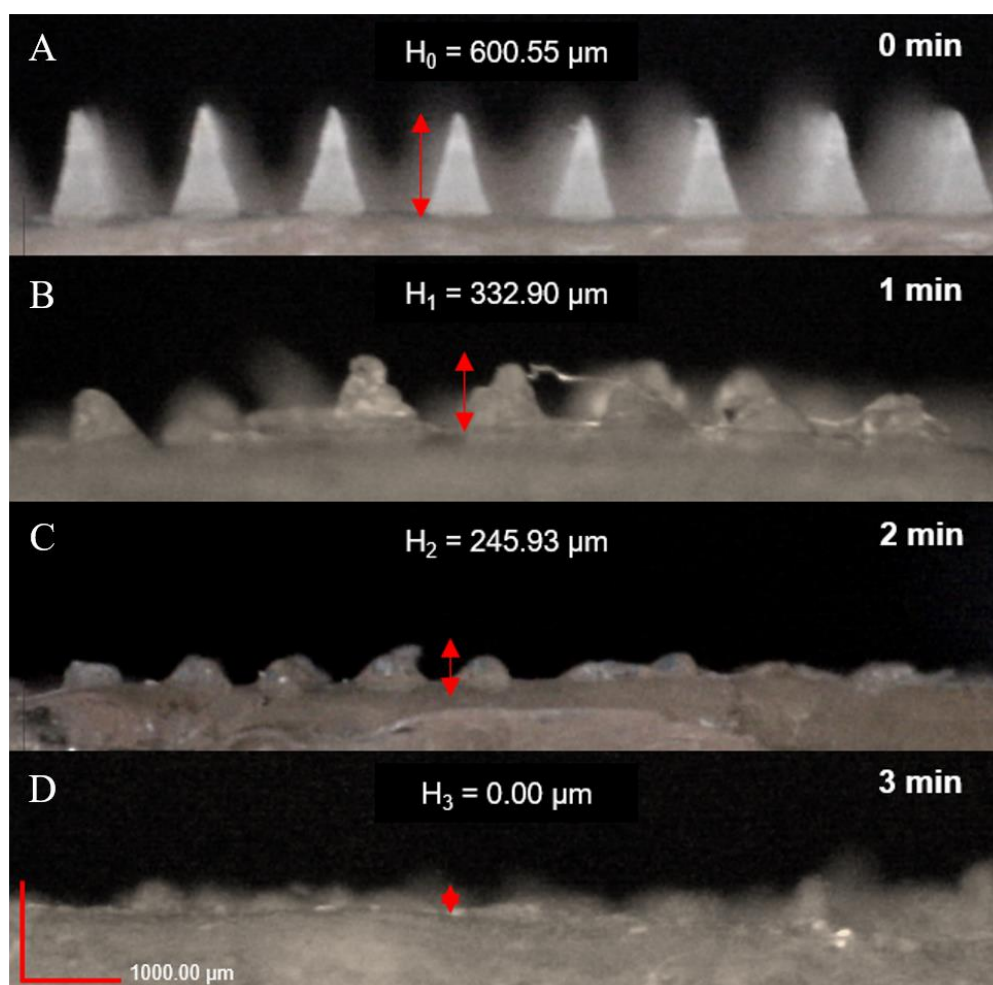
Figure 37: Digital Images of the dissolution of MEs-FLUZ-loaded two-layered dissolving MNs at different time points of (A) 0 min, (B) 1 min, (C) 2 min, and (D) 3 min after the application of MNs into and then removed from the corneal tissues

4.4.4 Loading efficiency

Quantification of the amount of FLUZ in microemulsion-loaded two-layered dissolving MNs was conducted to verify dosage accuracy and reproducibility. The drug content was determined to be 12.69 ± 0.32 mg per 121 needles or 0.10 ± 0.01 mg per needle. The loading efficiency was calculated to be $86.21 \pm 2.89\%$. These findings indicate that the outer layer of polymer film effectively encloses MEs-FLUZ within the two-layered dissolving MNs, resulting in minimal drug interaction before release.

4.5 *In vitro* ocular permeation

Figure 38 shows the percentage of FLUZ permeation through corneal tissue over 24 h after applied with different formulations, which were ranked in the following order: F5 (56.84±2.61%) > F3 (29.20±5.20%) > F2 (7.78±0.30%) > F4 (3.95±0.23%) > F1 (0.00±0.00%). The MEs-FLUZ-loaded two-layered dissolving MNs (F5) demonstrated significantly higher permeation than other formulations. The ocular permeation profile in Table 24, as measured by J and Q_{24}/A values, followed the same trend: F5 > F3 > F2 > F4 > F1. The MEs-FLUZ-loaded two-layered dissolving MNs showed significantly higher J and Q_{24}/A values than the other formulations. The short lag time (approximately 0.18 - 0.19 h) of the MNs formulations was due to the micro-channels created by the MNs in the corneal tissue, allowing the faster release of FLUZ that was entrapped in the polymer matrix than topical formulations, resulting in a high diffusion coefficient (K_d). Additionally, MEs-FLUZ-loaded two-layered dissolving MNs showed an improvement in FLUZ's permeability coefficient (Kp) into the corneal tissue. The lowest ocular permeation profile was observed with F1 formulations, likely due to the moderate lipophilicity of FLUZ (log P = 0.58), which did not allow for partitioning into the cornea. The F2 formulations dissolved in oil also had low ocular permeation profiles due to the accumulation of the drug in the cornea's epithelial barrier (Table 24). Because the corneal barrier structure was composed of hydrophilic and lipophilic structures, MEs formulation (F3) increased the ocular permeation profile by bypassing this barrier structure. On the other hand, one-layer MNs formulation (F4) showed low ocular permeation profiles due to incomplete dissolution of FLUZ in the water compartment. Consequently, the MEs-FLUZ-loaded two-layered dissolving MNs (F5) achieved high ocular permeation profiles by bypassing the corneal barrier structure using a nature of the hydrophilic-lipophilic formulation.
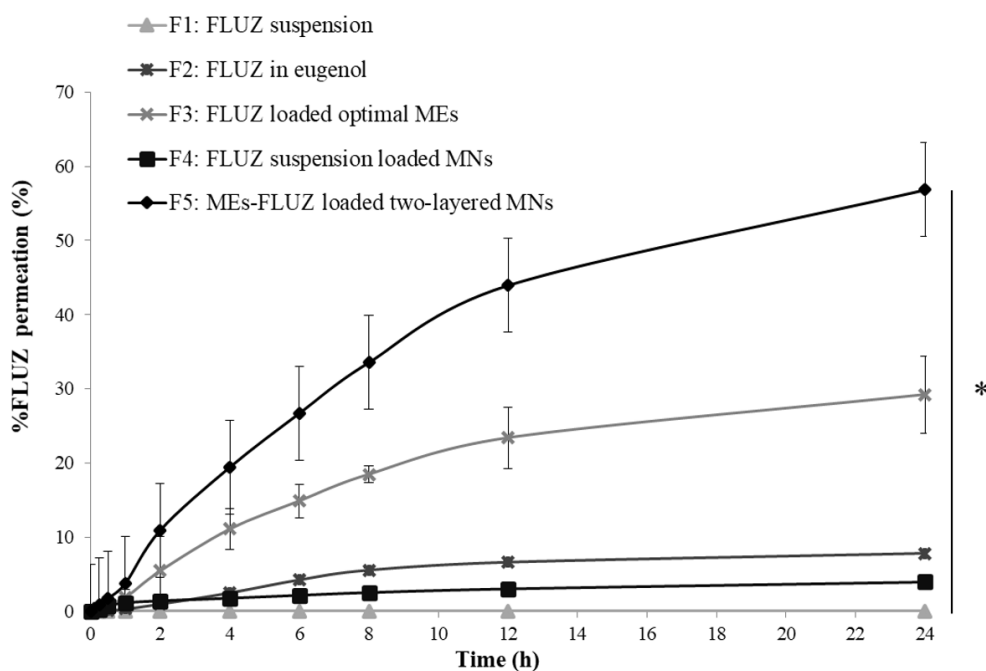
Figure 38: Percentage of FLUZ permeation through porcine corneal tissues over 24 h after applied with different formulations of F1; FLUZ suspension (▲), F2; FLUZ in eugenol (✳), F3; FLUZ loaded optimal MEs (✻), F4; FLUZ suspension loaded MNs (■) and F5; MEs-FLUZ-loaded two-layered dissolving MNs (◆), *$p < 0.05$ compared with other formulations

Table 24 shows that the percentage of FLUZ that remained in the corneal tissue after 24 h of applying MEs-FLUZ-loaded two-layered dissolving MNs was significantly greater than that of other formulations. The result suggests that the needles of the dissolving MNs carrying MEs-FLUZ could create micro-channels in the corneal tissue, resulting in a substantial FLUZ reservoir being deposited and retained prior to its release into the eye.

Table 24: Ocular permeation profile of FLUZ after applied with different formulations

Ocular permeation profile[#]	Formulations				
	F1: FLUZ suspension	F2: FLUZ in eugenol	F3: FLUZ-loaded optimal MEs	F4: FLUZ suspension loaded MNs	F5: MEs-FLUZ-loaded two-layered dissolving MNs
Lag time (h)	0.00±0.00	0.60±0.12	0.74±0.30	0.18±0.06	0.19±0.08
J (mg/cm^2/h)	0.00±0.00	0.12±0.01	0.39±0.03	0.11±0.02	0.70±0.13*
Q_{24}/A (mg/cm^2)	0.00±0.00	1.26±0.05	4.72±0.84	0.64±0.04	9.19±0.33*
K_d ($\times 10^{-3}$, cm^2/h)	0.00±0.00	1.02±0.21	0.89±0.31	3.66±1.47	3.56±1.20
K_p ($\times 10^{-3}$, cm^2/h)	0.00±0.00	9.17±0.70	30.93±2.06	8.60±1.52	55.17±10.36*
%FLUZ remained	0.00±0.00	27.72±4.33	14.94±1.34	16.90±3.28	38.45±3.27*

[#]Ocular permeation profile: J, flux; Q_{24}/A, cumulative amount of FLUZ at 24 h per area; K_d, diffusion coefficient; K_p, permeability coefficient. *$p < 0.05$ compared with other formulations

4.6 *Ex vivo* ocular permeation

Whole porcine eyeballs were used to test ex vivo ocular FLUZ delivery due to their similarity to the human eye in ocular histology and water content (171). The percentage of FLUZ permeation over 8 hours using MEs-FLUZ-loaded two-layered dissolving MNs was 11.63±4.54%, significantly higher than FLUZ suspension-loaded MNs, as presented in Figure 39. Additionally, other ocular permeation parameters such as the lag time, J, Q_{24}/A, K_d, and K_p of MEs-FLUZ-loaded two-layered dissolving MNs were reported as 0.16±0.02 h, 0.24±0.10 mg/cm^2/h, 1.88±0.58 mg/cm^3, (3.79±0.48) $\times 10^{-3}$ cm^2/h, and (19.08±8.15) $\times 10^{-3}$ cm^2/h, respectively. The *ex vivo* ocular FLUZ delivery over 8 h was lower than the *in vitro* study, possibly because the dissolving MNs could dissolve on the cornea before being fully inserted. Furthermore, FLUZ was eliminated *via* vascular endothelium after crossing the corneal barrier. However, the percentage of FLUZ retained in corneal tissue was 30.01±3.18%, indicating that the two-layered MNs formulation resulted in a highly

deposited drug within the corneal tissue, creating a large drug reservoir before being released for the treatment of fungal keratitis.
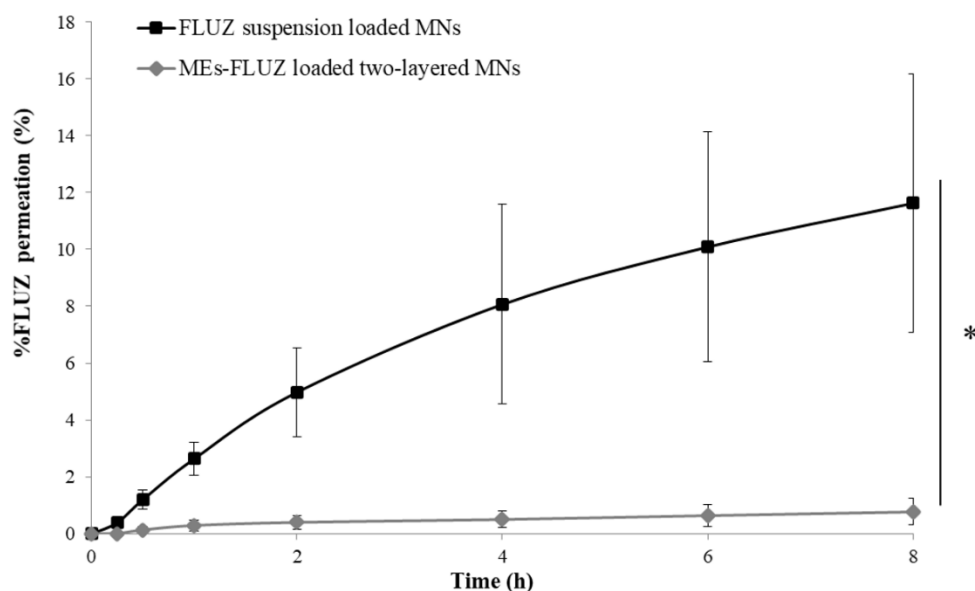
Figure 39: *Ex vivo* ocular drug delivery of MEs-FLUZ-loaded two-layered dissolving MNs (♦) compared with FLUZ suspension-loaded MNs (■). *$p < 0.05$ compared with other formulations

4.7 Antifungal activity

- Agar disc diffusion method

Figure 40 illustrates the diameter of the inhibition zone resulting from the MEs-FLUZ-loaded two-layered dissolving MNs insertion into the SDA agar plate. The result showed a similar inhibition zone following treated with FLUZ in eugenol and FLUZ-loaded optimal MEs at the same drug concentration, indicating that the MEs-FLUZ was released from the two-layer MNs after complete dissolution on the SDA plate and exhibited antifungal activity comparable to FLUZ in eugenol formulation. In contrast, FLUZ suspension showed a lower percent zone inhibition due to its insolubility in water, which reduced its ability to penetrate the *Candida albicans* plasma membrane. The mechanism of the azoles group is based on blocking the synthesis of ergosterol, a cytochrome P450-dependent enzyme, in the plasma

membrane, thereby inhibiting fungal growth (172). Additionally, eugenol's phenolic hydroxyl group had potent antifungal activity against *Candida albicans* and disrupted the plasma membrane. Therefore, eugenol had a synergistic effect with FLUZ, enhancing FLUZ solubility and antifungal activity (173).
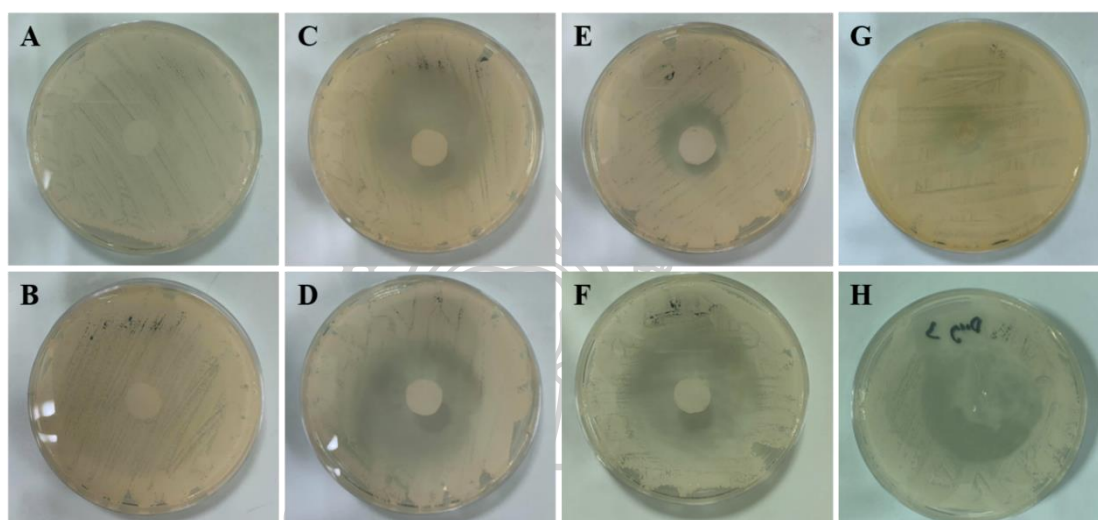
Figure 40: Antifungal activity against *C. albicans* of various formulations, including control (A), FLUZ suspension (B), eugenol (C), FLUZ in eugenol (D), optimal MEs (E), FLUZ-loaded optimal MEs (F), Two-layered MNs (G) and MEs-FLUZ-loaded two-layered dissolving MNs (H) following being analyzed by agar diffusion assay

- **Infection of *ex vivo* porcine corneas and FLUZ treatment**

Figure 41 shows the results of applying FLUZ formulations on the infected fungal cornea to evaluate antifungal activity in corneal tissue. The MEs-FLUZ-loaded two-layered dissolving MNs insertion into corneal tissue showed the least colony-forming unit (CFU) of 5.56 ± 1.92 ($\times 10^4$) CFU/ml, indicating that this formulation provided a sufficient concentration of antifungal activity when the fungal infection spread into the deeper corneal tissue. In contrast, topical formulations could not penetrate the deeper layers of the corneal tissue structure, resulting in failed treatment of fungal keratitis.
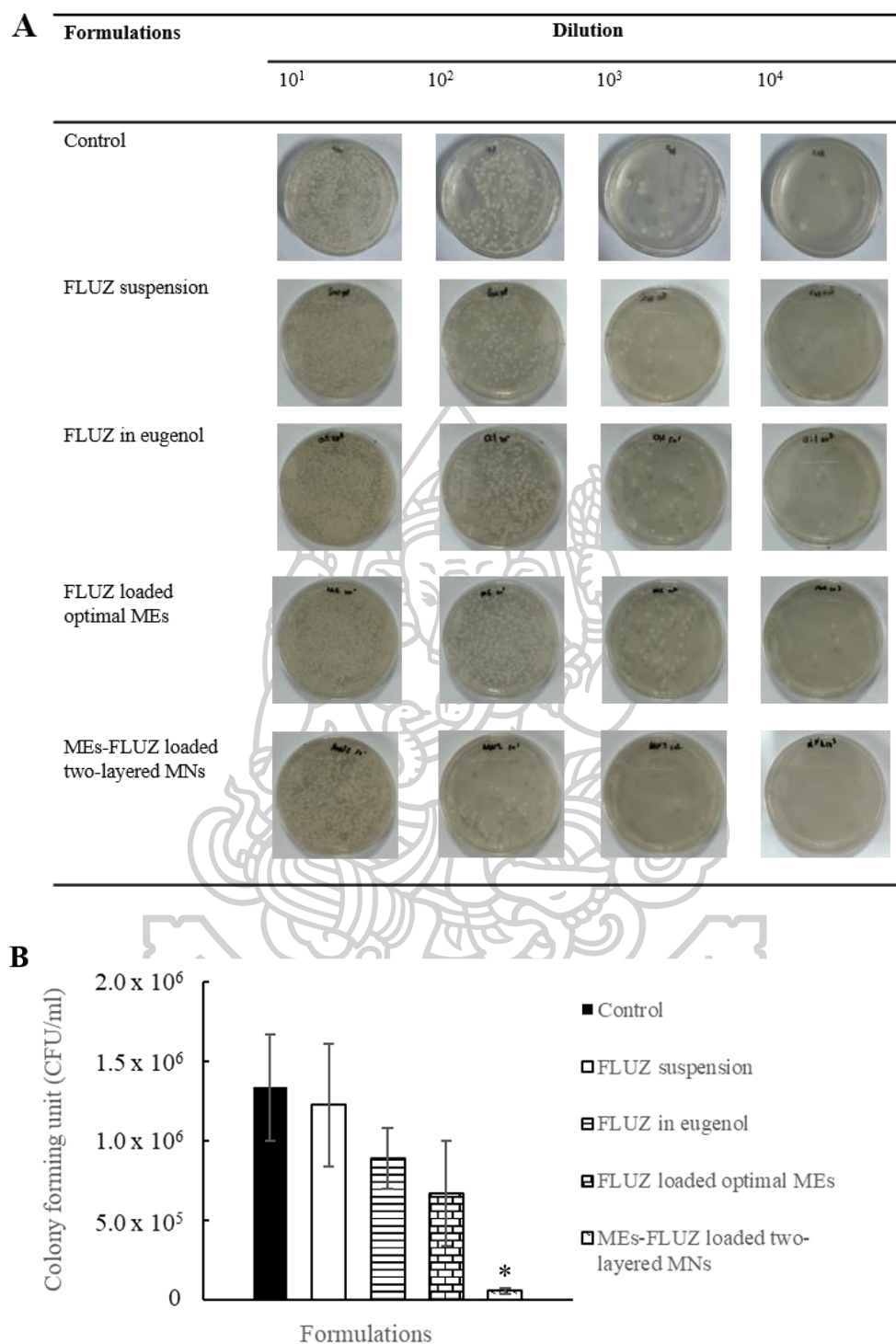
Figure 41: *Ex vivo* antifungal activity (A) Photographs of C. *albicans* colonies formed on SDA plates at 10^1-10^4 dilution and (B) Colony forming units after applying different FLUZ formulations on excised porcine corneal tissues for 24 h. *$p < 0.05$ compared with other formulations

4.8 Stability test

The study examined the stability of MEs-FLUZ-loaded two-layered dissolving MNs over 1, 2, 3, and 6 months after being stored at 4, 25, and 40 °C in an aluminum zipper pouch following ICH Q1A(R2) Drug products packaged in impermeable containers, represented in Figure 42. The physical appearance and mechanical strength remained unchanged after being kept at 4 and 25 °C. However, at 40 °C, the mechanical strength significantly decreased because of the high temperature affecting the polymer's hardness. Moreover, after being kept the MNs at 4 °C, the mechanical strength slightly increased due to polymer shrinkage. The %drug content's stability remained consistent at 92.18% to 107.07% throughout the study. The results suggest that MEs-FLUZ-loaded two-layered dissolving MNs were physically and chemically stable for up to 6 months in an aluminum zipper pouch with silica gel at temperatures not exceed than 25°C.
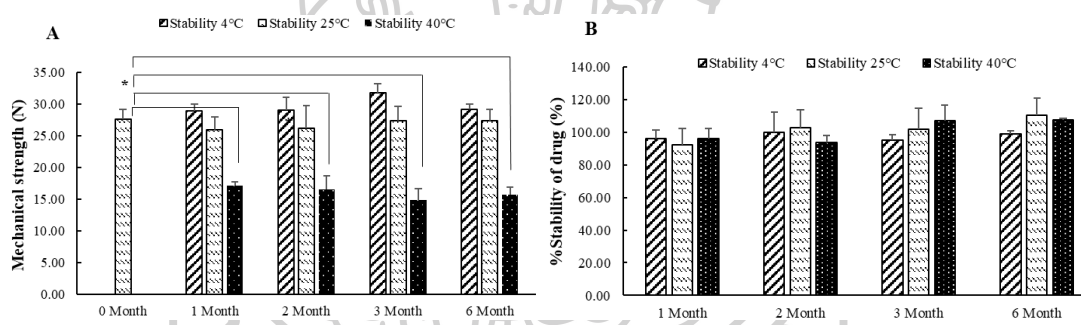
Figure 42: Stability of MEs-FLUZ-loaded two-layered dissolving MNs over 1, 2, 3, and 6 months after being stored at 4 (▨), 25 (▢), and 40 (▣) °C, mechanical strength (A) and drug content (B)

CHAPTER 5

CONCLUSION

The study introduced a newly formulated two-layered dissolving MNs loading microemulsion to improve the solubility of hydrophobic drugs, FLUZ, for ocular drug delivery. The optimal MEs-FLUZ was designed using a statistical computer program with an I-optimal mixture design. The result showed that the optimal MEs-FLUZ comprised 20.54 %w/w eugenol as an oil phase, 67.70 %w/w of the Smix (Tween 80: ethanol at a weight ratio of 3:1), and 10%w/w of the water phase. The concentration of the MEs-FLUZ components affected the globule size, drug content, and percentage of drug permeation over 8 h. The optimized MEs-FLUZ showed an appropriate globule size of 121.22±9.01 nm with an acceptable polydispersity index (PDI) of 0.30±0.02 and neutral charge (0.012 ± 0.001 mV). The pH of optimized MEs-FLUZ was 6.91±0.10. The drug content of the optimized MEs-FLUZ was 73.58 ± 0.54 mg/mL with high physical stability and no phase separation observed.

The MEs-FLUZ-loaded two-layered dissolving MNs exhibited desirable physical properties, good mechanical strength, and penetration ability with minimal invasion on corneal tissue. The polymer mixture of 3% chitosan and 20% PVA at a weight ratio of 1:4 was used to fabricate the outer layer. The MEs-FLUZ-loaded two-layered dissolving MNs were successfully fabricated with a conical-shaped array (11×11 needles in 1 cm^2 patch area) with an average of 581.83±10.58 μm in height, 300.03±1.51 μm in width, and 300.10±0.12 μm in interspace. The mechanical strength of two-layered dissolving MNs with or without MEs-FLUZ loading was 20.85±1.09 N and 21.57 ±1.04 N, respectively, which showed no significant difference in the mechanical strength. The insertion force of an optimal formulation required to complete insertion (100%) into the membrane was 5.18±0.49 N/121 arrays or 0.04 N per needle. The observed penetration depth of the MEs-FLUZ-loaded two-layered dissolving MNs was 213.70±10.65 μm. The dissolution ability showed that the MEs-FLUZ-loaded two-layered dissolving MNs was completely dissolved within 3 min.

For the first time, the study successfully demonstrated the potential of using two-layer dissolving MNs for intracorneal ME s-FLUZ delivery with high drug content of 12.69 ± 0.32 mg per patch ($86.21\pm2.89\%$ of loading efficacy). *In vitro* and *ex vivo* corneal permeation demonstrated a significant permeation profile of FLUZ delivered from MEs-FLUZ-loaded two-layered dissolving MNs ($56.84\pm2.61\%$ delivered from *in vitro* and $11.63\pm4.54\%$ delivered from *ex vivo*) higher than other groups. Therefore, the MEs-FLUZ-loaded two-layered dissolving MNs formulation had appropriate properties for the ocular delivery of FLUZ to treat fungal keratitis.

Importantly, the MEs-FLUZ-loaded two-layered dissolving MNs showed highly effective antifungal activity of *Candida albicans* in the infected corneal tissue with stability for up to 6 months at temperatures of 4 to 25 °C. In conclusion, the optimal MEs-FLUZ-loaded two-layered dissolving MNs revealed suitable minimally invasive MNs properties for an effective fungal keratitis treatment. The value to practical use seems to be considerable; evaluating the efficacy of treating fungal keratitis *in vivo* and safety is important to ensure that they are effective and do not act as a barrier to regular use and, therefore, successful commercialization.

APPENDIX

APPENDIX A
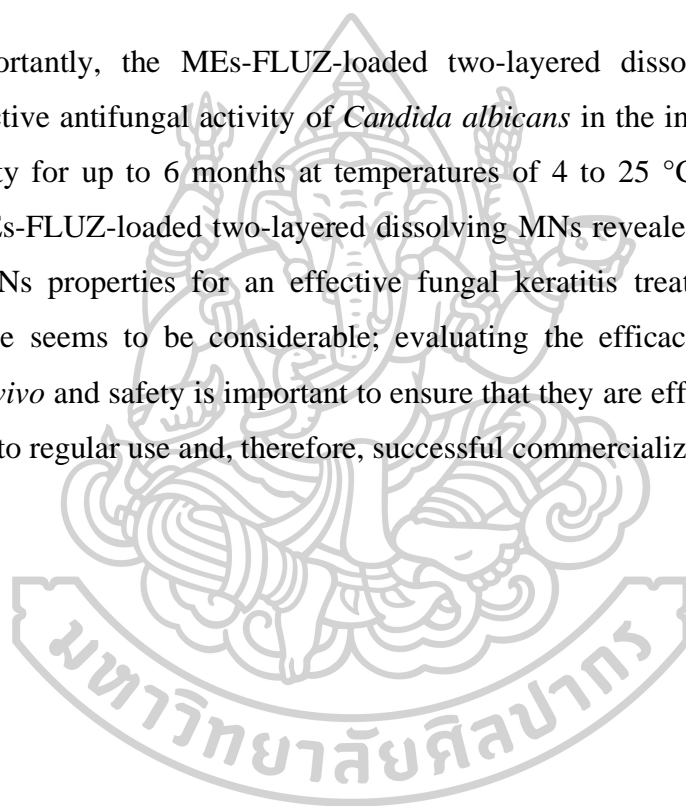
Standard curve of fluconazole

Determination of fluconazole in the sample

Standard: Fluconazole

Method: HPLC analysis

Analytic column: Zorbax Eclipse XDB-C18 reverse phase column (250 x 4.6 mm, 5 µm pore size) (Agilent, Santa Clara, United States)

Mobile phase: 45%v/v methanol: 55%v/v ultrapure water

Flow rate: 1 mL/min

UV detector: Wavelength 260 nm

Concentration (µg/mL): 0.01, 0.1, 1, 10, 100, and 1000

Figure 43: Standard curve of FLUZ at the concentration of 10-1000 µg/mL used for drug quantification of the drug content and ocular permeation study
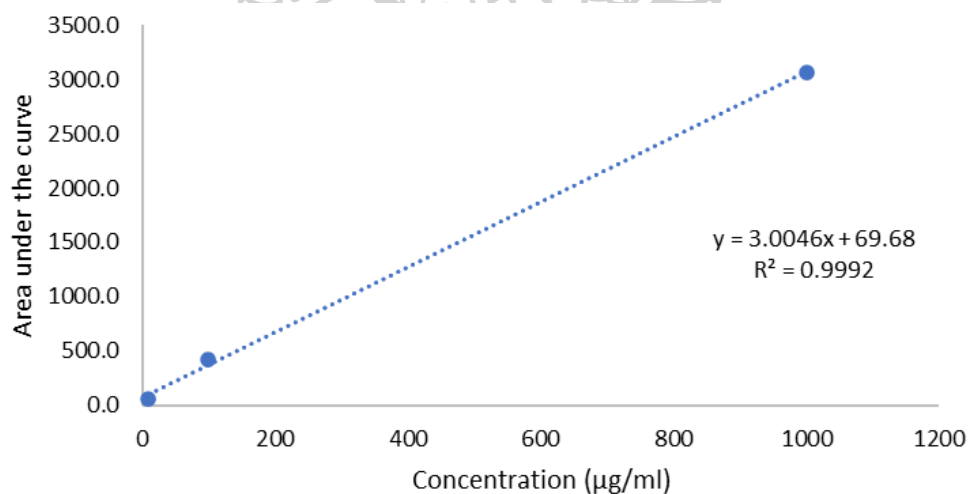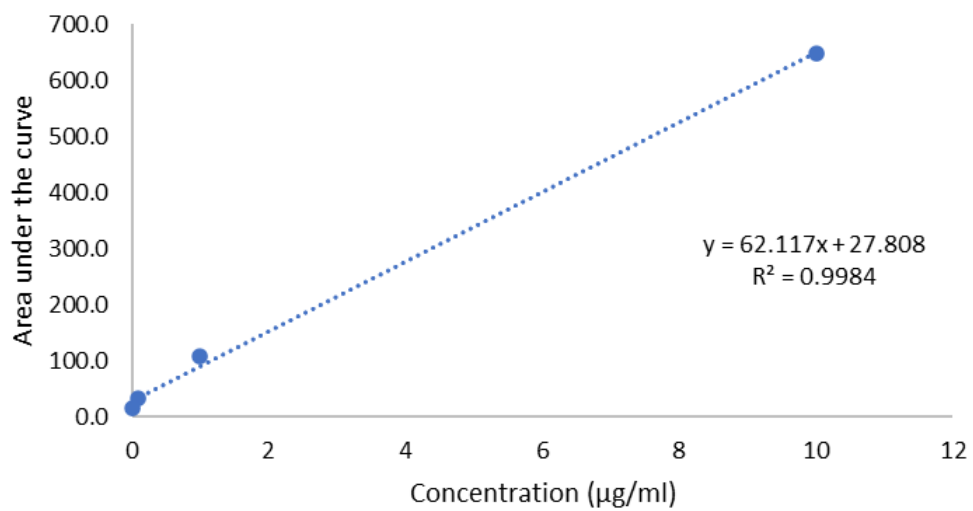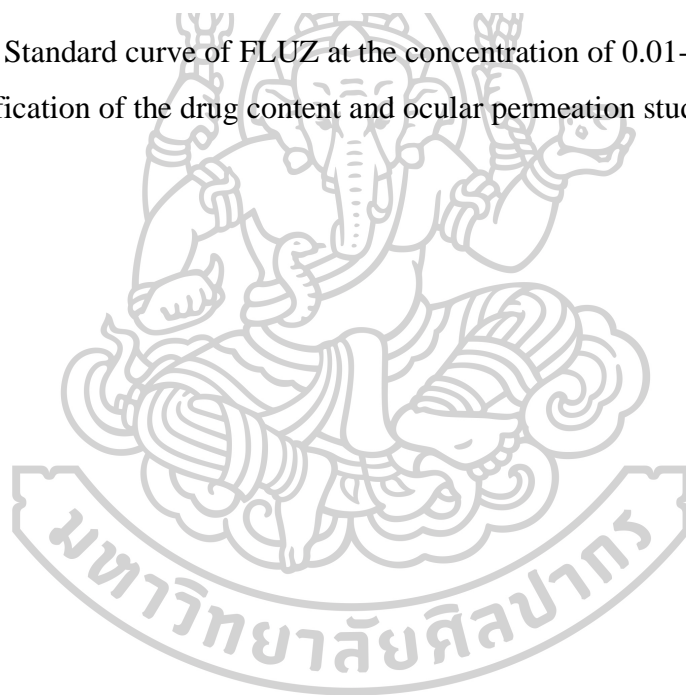
Figure 44: Standard curve of FLUZ at the concentration of 0.01-10 µg/mL used for drug quantification of the drug content and ocular permeation study
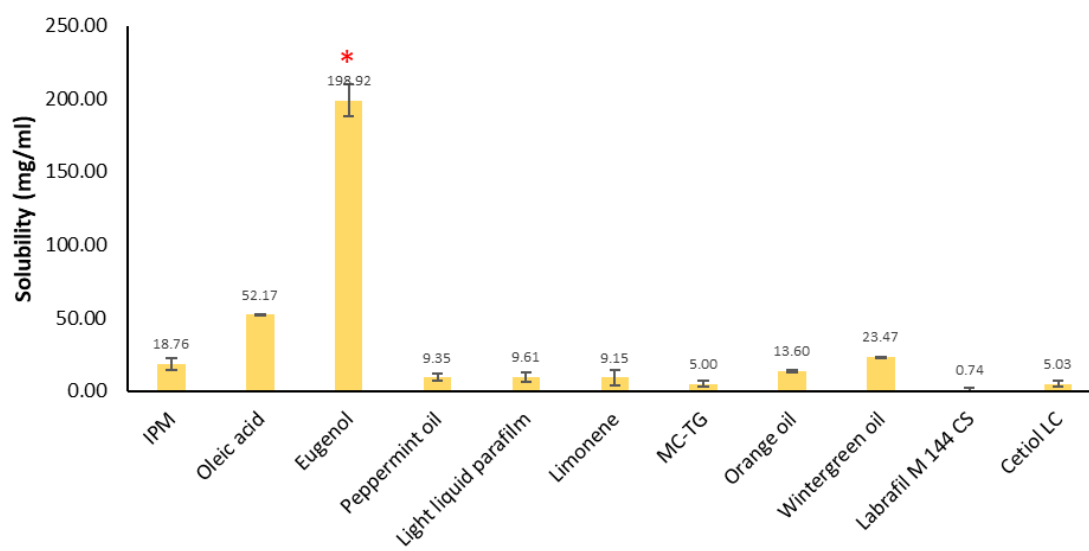
Solubility of fluconazole

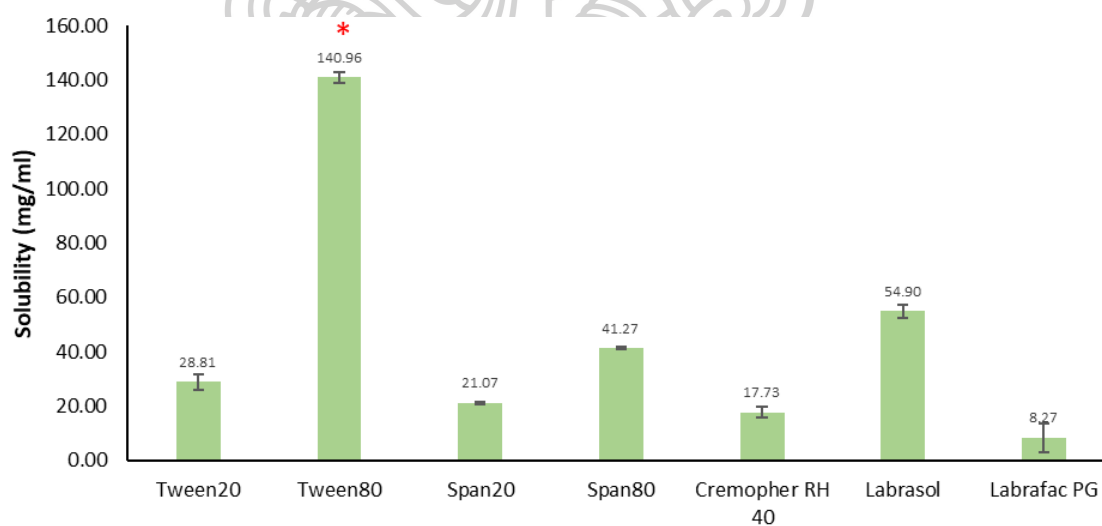**Figure 45:** Solubility of FLUZ in different types of oil

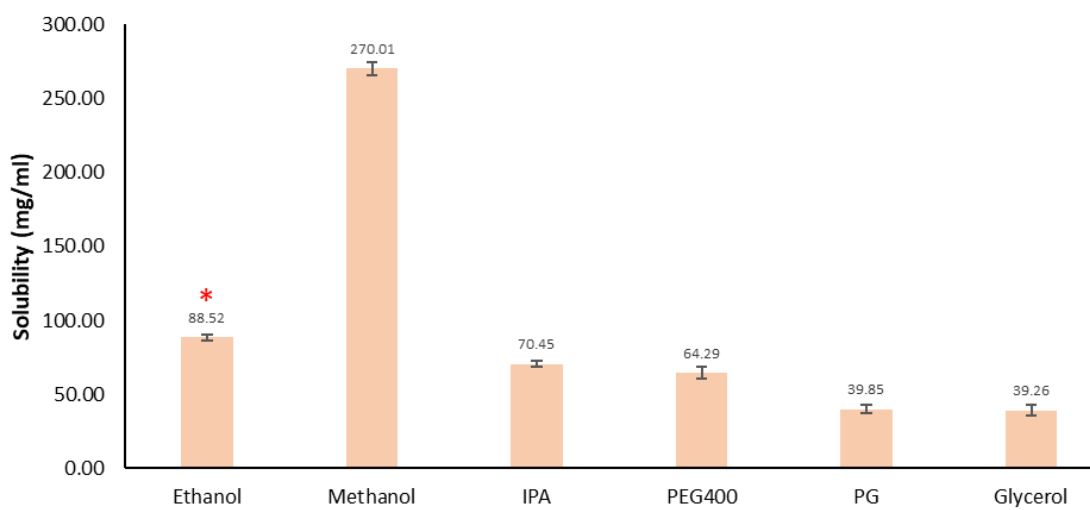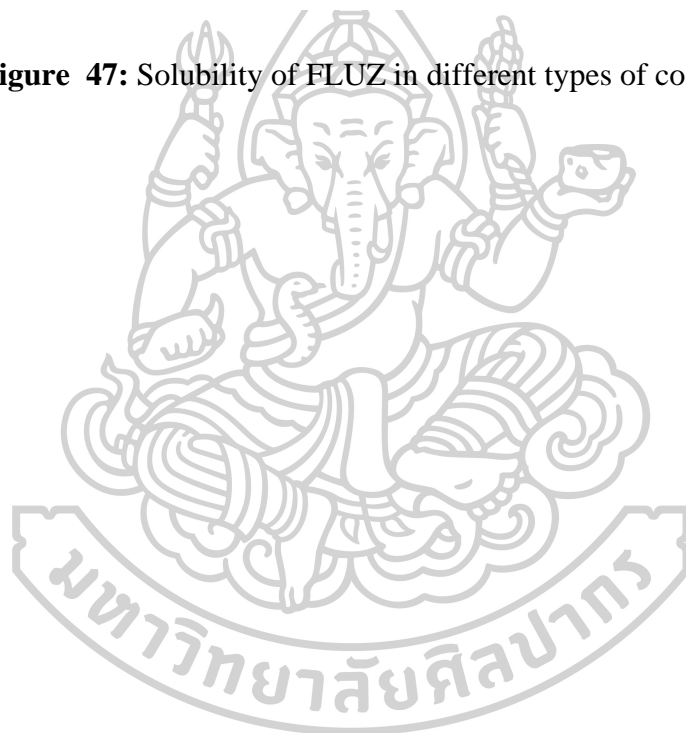**Figure 46:** Solubility of FLUZ in different types of surfactant

Figure 47: Solubility of FLUZ in different types of co-surfactant

Calculation of Ternary Plot Instructions

Table 25: Ternary plot of S_{mix} at the weight ratio of 1:1

								CALCULATED				
		ENTER DATA HERE						**Raw Data**			**Transformed Data**	
Zone	**Sample ID**	**Raw Data**						**Normalized to 100**			**X**	**Y**
		Top	**Left**	**Right**	**SUM**	**TOP**	**LEFT**	**RIGHT**	**SUM**		**=RIGHT+(TOP/2)**	**=TOP**
Upper	A	1.0	0.00	0.0	1.00	100.0	0.0	0.0	100.00		50.00	100.00
Upper	B	0.9	0.04	0.1	1.04	86.5	3.8	9.6	100.00		52.88	86.54
Upper	C	0.8	0.07	0.2	1.07	74.8	6.5	18.7	100.00		56.07	74.77
Upper	D	0.7	0.09	0.3	1.09	64.2	8.3	27.5	100.00		59.63	64.22
Lower	E	0.6	0.13	0.4	1.13	53.1	11.5	35.4	100.00		61.95	53.10
Lower	F	0.5	0.17	0.5	1.17	42.7	14.5	42.7	100.00		64.10	42.74
Lower	G	0.4	0.19	0.6	1.19	33.6	16.0	50.4	100.00		67.23	33.61
Lower	H	0.3	0.20	0.7	1.20	25.0	16.7	58.3	100.00		70.83	25.00
Lower	I	0.2	0.20	0.8	1.20	16.7	16.7	66.7	100.00		75.00	16.67
Lower	J	0.1	5.00	0.9	6.00	1.7	83.3	15.0	100.00		15.83	1.67
Lower	K	0.0	10000.00	1.0	#######	0.0	100.0	0.0	100.00		0.01	0.00

Table 26: Ternary plot of S_{mix} at the weight ratio of 1:2

								CALCULATED				
		ENTER DATA HERE						**Raw Data**			**Transformed Data**	
Zone	**Sample ID**	**Raw Data**						**Normalized to 100**			**X**	**Y**
		Top	**Left**	**Right**	**SUM**	**TOP**	**LEFT**	**RIGHT**	**SUM**		**=RIGHT+(TOP/2)**	**=TOP**
Upper	A	1.0	0.00	0.0	1.00	100.0	0.0	0.0	100.00		50.00	100.00
Upper	B	0.9	0.05	0.1	1.05	85.7	4.8	9.5	100.00		52.38	85.71
Upper	C	0.8	0.08	0.2	1.08	74.1	7.4	18.5	100.00		55.56	74.07
Upper	D	0.7	0.11	0.3	1.11	63.1	9.9	27.0	100.00		58.56	63.06
Lower	E	0.6	0.16	0.4	1.16	51.7	13.8	34.5	100.00		60.34	51.72
Lower	F	0.5	0.21	0.5	1.21	41.3	17.4	41.3	100.00		61.98	41.32
Lower	G	0.4	0.24	0.6	1.24	32.3	19.4	48.4	100.00		64.52	32.26
Lower	H	0.3	0.20	0.7	1.20	25.0	16.7	58.3	100.00		70.83	25.00
Lower	I	0.2	0.20	0.8	1.20	16.7	16.7	66.7	100.00		75.00	16.67
Lower	J	0.1	0.20	0.9	1.20	8.3	16.7	75.0	100.00		79.17	8.33
Lower	K	0.0	10000.00	1.0	#######	0.0	100.0	0.0	100.00		0.01	0.00

Table 27: Ternary plot of S_{mix} at the weight ratio of 2:1

								CALCULATED				
		ENTER DATA HERE						**Raw Data**			**Transformed Data**	
Zone	**Sample ID**	**Raw Data**						**Normalized to 100**			**X**	**Y**
		Top	**Left**	**Right**	**SUM**	**TOP**	**LEFT**	**RIGHT**	**SUM**		**=RIGHT+(TOP/2)**	**=TOP**
Upper	A	1.0	0.00	0.0	1.00	100.0	0.0	0.0	100.00		50.00	100.00
Upper	B	0.9	0.04	0.1	1.04	86.5	3.8	9.6	100.00		52.88	86.54
Upper	C	0.8	0.06	0.2	1.06	75.5	5.7	18.9	100.00		56.60	75.47
Upper	D	0.7	0.08	0.3	1.08	64.8	7.4	27.8	100.00		60.19	64.81
Lower	E	0.6	0.11	0.4	1.11	54.1	9.9	36.0	100.00		63.06	54.05
Lower	F	0.5	0.13	0.5	1.13	44.2	11.5	44.2	100.00		66.37	44.25
Lower	G	0.4	0.16	0.6	1.16	34.5	13.8	51.7	100.00		68.97	34.48
Lower	H	0.3	0.17	0.7	1.17	25.6	14.5	59.8	100.00		72.65	25.64
Lower	I	0.2	0.20	0.8	1.20	16.7	16.7	66.7	100.00		75.00	16.67
Lower	J	0.1	5.00	0.9	6.00	1.7	83.3	15.0	100.00		15.83	1.67
Lower	K	0.0	100000.00	1.0	#######	0.0	100.0	0.0	100.00		0.00	0.00

Table 28: Ternary plot of S_{mix} at the weight ratio of 3:1

							CALCULATED					
		ENTER DATA HERE					Raw Data				Transformed Data	
Zone	Sample ID	Raw Data					Normalized to 100				X	Y
		Top	Left	Right	SUM	TOP	LEFT	RIGHT	SUM		=RIGHT+(TOP/2)	=TOP
Upper	A	1.0	0.00	0.0	1.00	100.0	0.0	0.0	100.00		50.00	100.00
Upper	B	0.9	0.03	0.1	1.03	87.4	2.9	9.7	100.00		53.40	87.38
Upper	C	0.8	0.06	0.2	1.06	75.5	5.7	18.9	100.00		56.60	75.47
Upper	D	0.7	0.07	0.3	1.07	65.4	6.5	28.0	100.00		60.75	65.42
Lower	E	0.6	0.09	0.4	1.09	55.0	8.3	36.7	100.00		64.22	55.05
Lower	F	0.5	0.13	0.5	1.13	44.2	11.5	44.2	100.00		66.37	44.25
Lower	G	0.4	0.15	0.6	1.15	34.8	13.0	52.2	100.00		69.57	34.78
Lower	H	0.3	0.20	0.7	1.20	25.0	16.7	58.3	100.00		70.83	25.00
Lower	I	0.2	0.95	0.8	1.95	10.3	48.7	41.0	100.00		46.15	10.26
Lower	J	0.1	5.00	0.9	6.00	1.7	83.3	15.0	100.00		15.83	1.67
Lower	K	0.0	100000.00	1.0	#######	0.0	100.0	0.0	100.00		0.00	0.00

Analysis data of fluconazole microemulsion
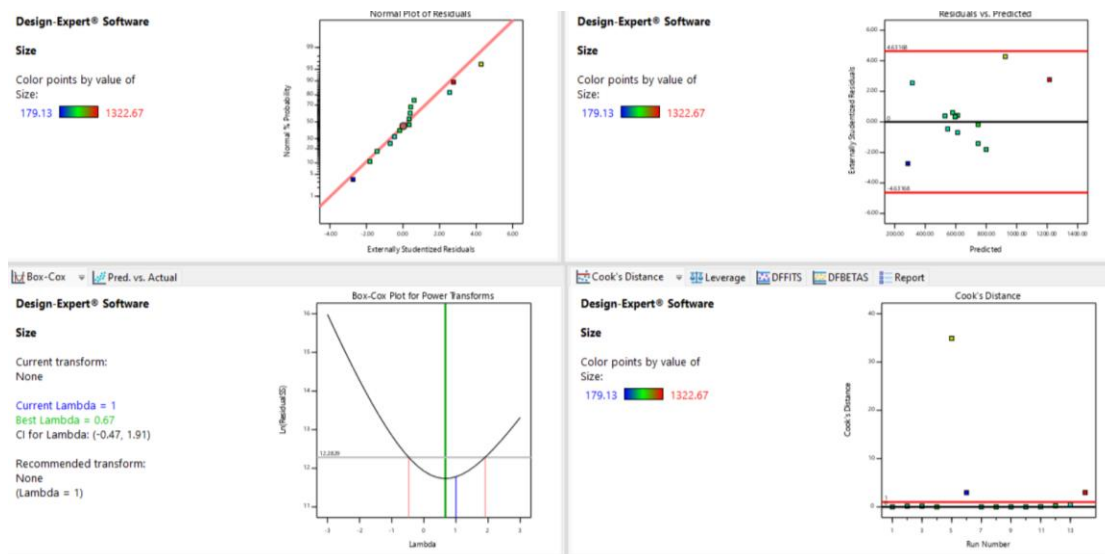
Figure 48: Analysis data of droplet size of MEs-FLUZ
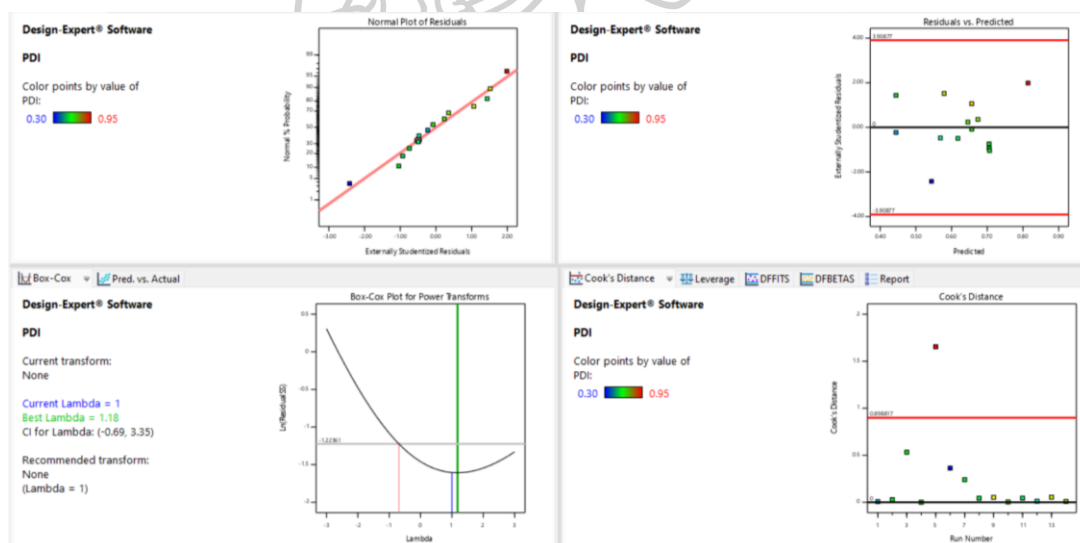
Figure 49: Analysis data of PDI of MEs-FLUZ
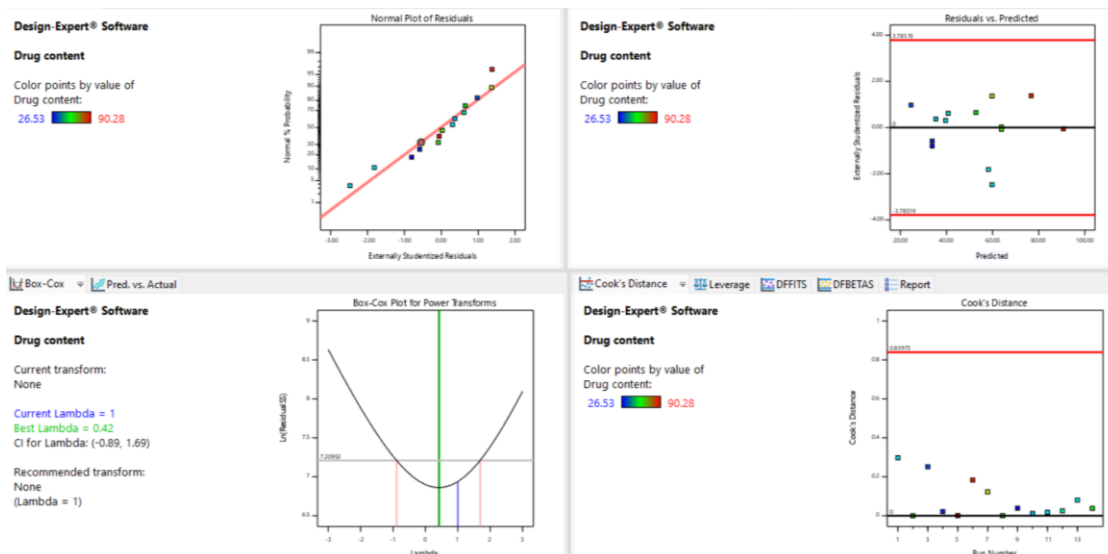
Figure 50: Analysis data of drug content of MEs-FLUZ
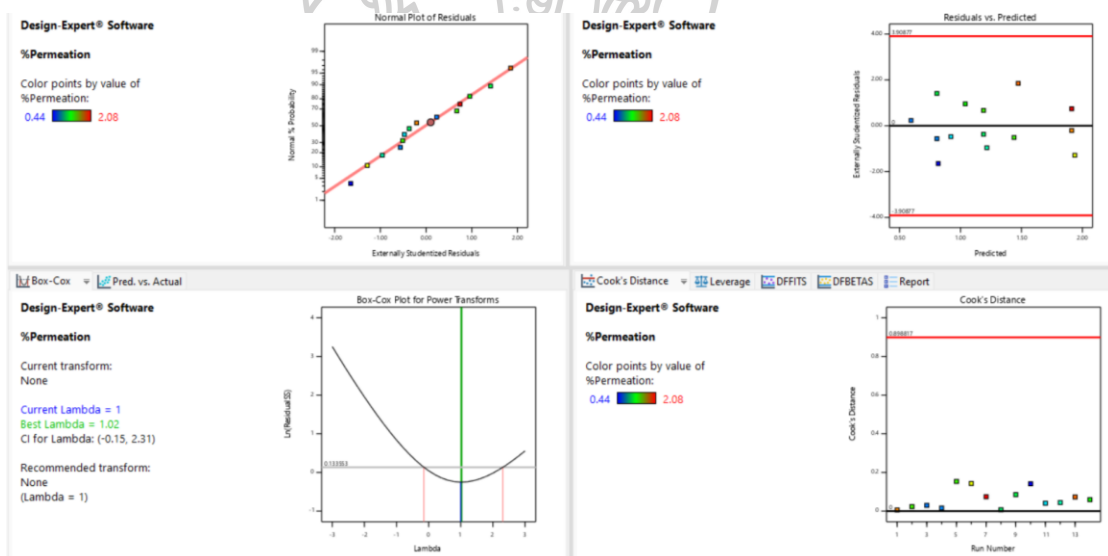
Figure 51: Analysis data of the drug permeation over 8 h of MEs-FLUZ

APPENDIX B

138
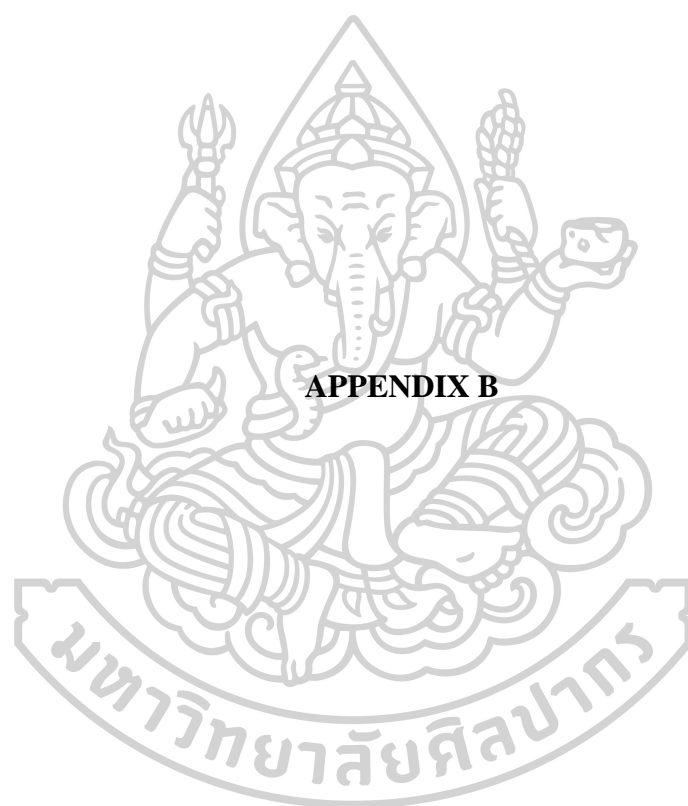
Table 29: Independent and dependent variables of MNs in 3^k factorial design of 3% Chitosan and 20% PVA

Formulation code	Independent variables (weight ratio)		Dependent variables	
	X_1: 3% Chitosan	X_2: 20% PVA	Y_1: Mechanical strength (N)	Y_2: MNs Height (μm)
C-P_MNs 1	1	1	29.79	590.50
C-P_MNs 2	1	3	43.39	642.32
C-P_MNs 3	1	5	38.09	601.30
C-P_MNs 4	3	1	24.67	550.20
C-P_MNs 5	3	3	31.20	578.10
C-P_MNs 6	3	3	30.04	585.10
C-P_MNs 7	3	3	28.11	595.40
C-P_MNs 8	3	3	34.01	583.10
C-P_MNs 9	3	5	33.38	550.20
C-P_MNs 10	5	1	20.07	530.70
C-P_MNs 11	5	3	18.16	540.40
C-P_MNs 12	5	5	27.97	543.60
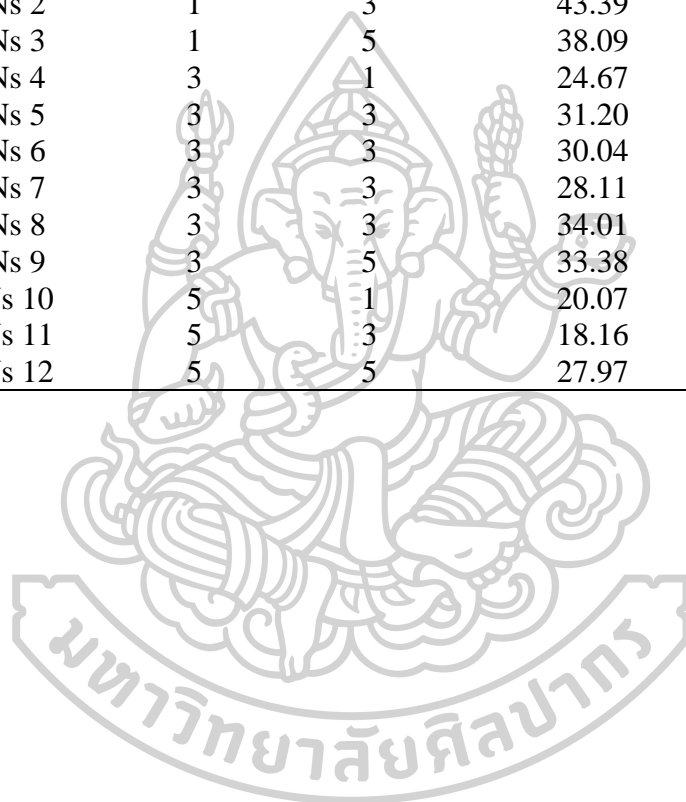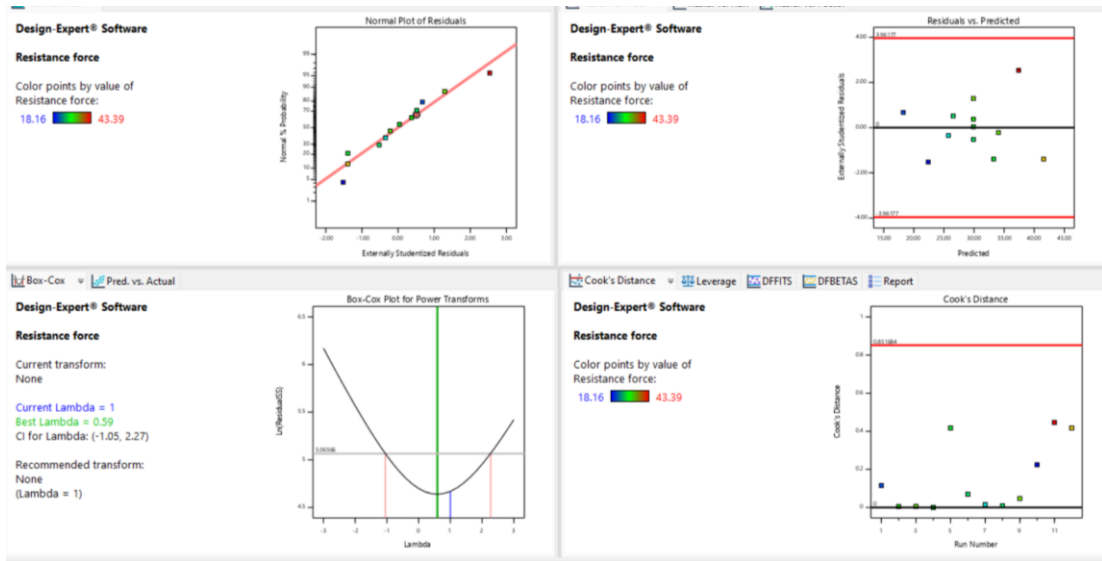
Figure 52: Analysis data of mechanical strength of 3% Chitosan and 20%PVA
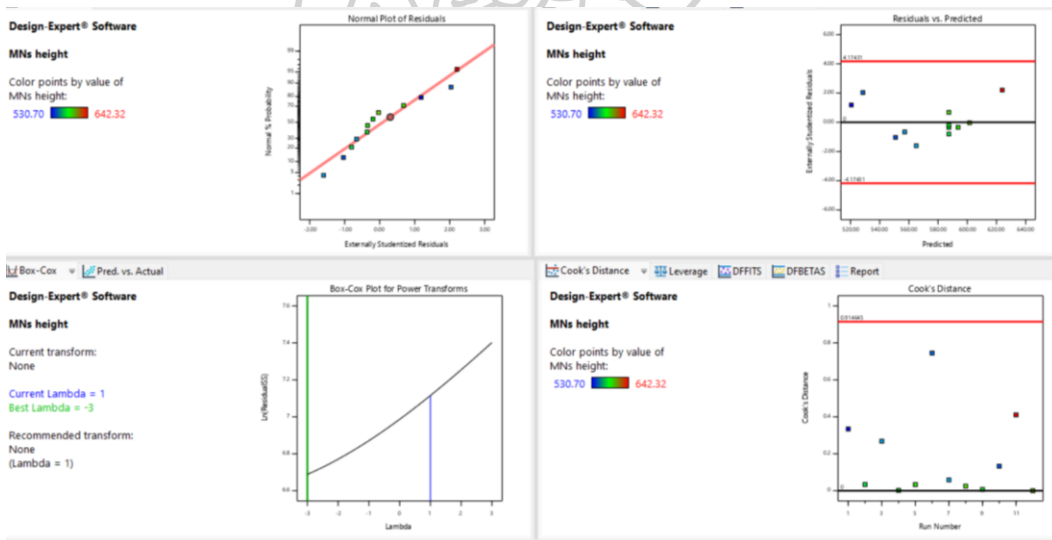
Figure 53: Analysis data of MNs height of 3% Chitosan and 20%PVA

Table 30: Independent and dependent variables of MNs in 3^k factorial design of 30%Gantrez® S-97 and 5%HA

Formulation code	Independent variables (weight ratio)		Dependent variables	
	X_1: 30%Gantrez® S-97	X_2: 5%HA	Y_1: Mechanical strength (N)	Y_2: Needles height (μm)
G-H_MNs 1	1	1	22.39	599.50
G-H_MNs 2	1	3	24.19	602.32
G-H_MNs 3	1	5	28.09	601.23
G-H_MNs 4	3	1	24.67	600.20
G-H_MNs 5	3	3	25.20	602.10
G-H_MNs 6	3	3	26.04	605.10
G-H_MNs 7	3	3	28.11	595.40
G-H_MNs 8	3	3	24.01	593.30
G-H_MNs 9	3	5	30.18	590.20
G-H_MNs 10	5	1	24.07	599.70
G-H_MNs 11	5	3	28.16	600.32
G-H_MNs 12	5	5	35.97	603.60
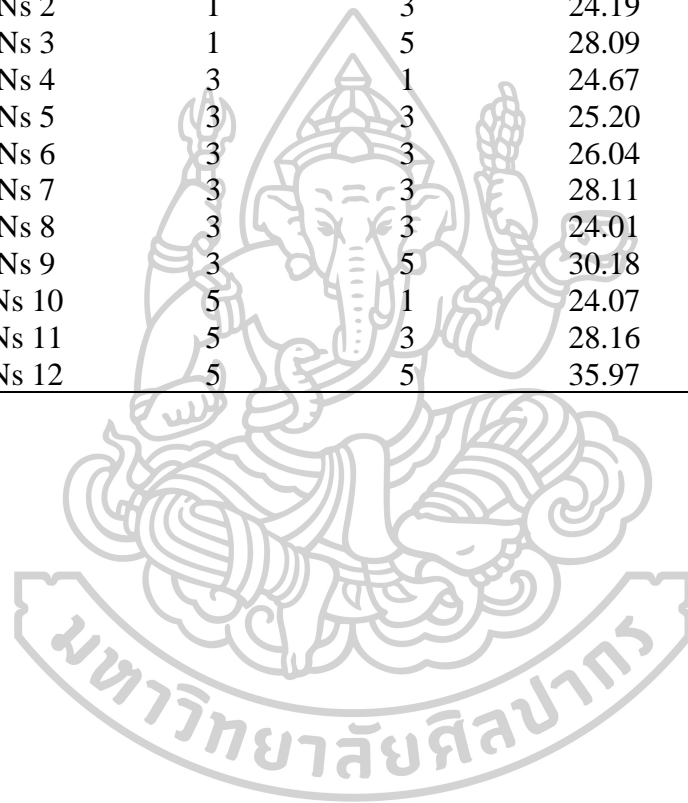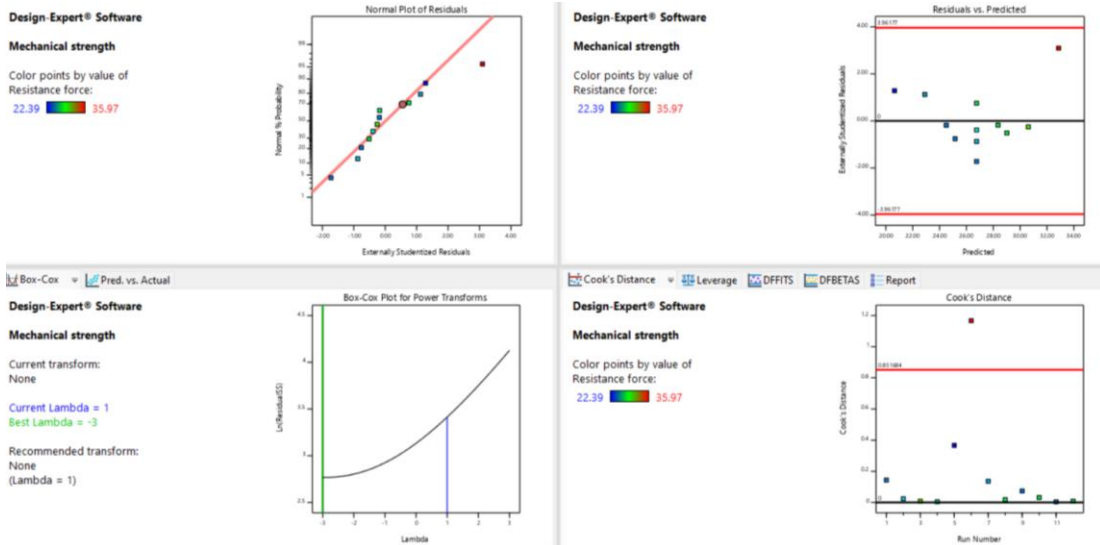
Figure 54: Analysis data of mechanical strength of 30%Gantrez® S-97 and 5%HA
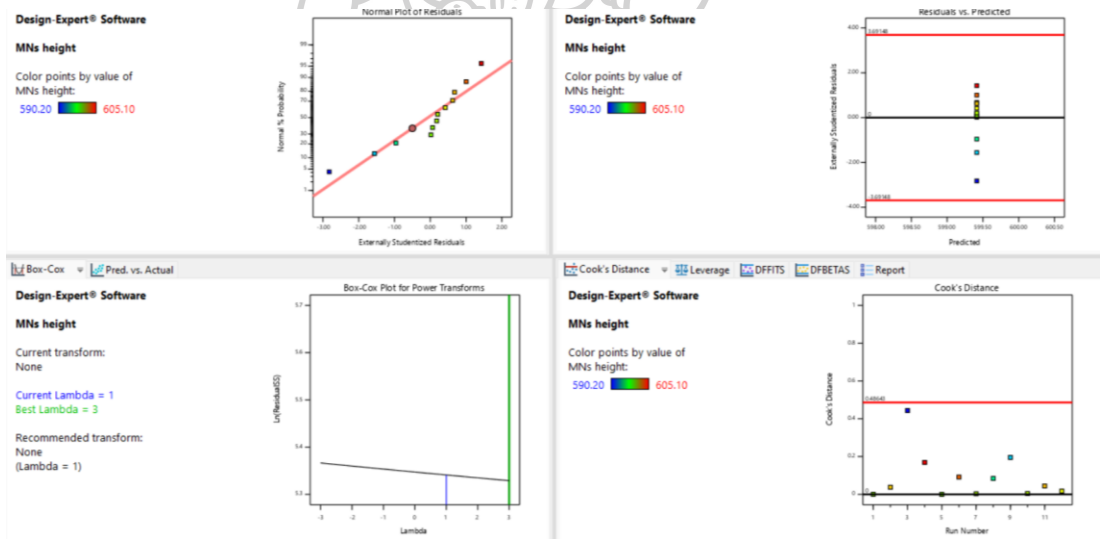
Figure 55: Analysis data of MNs height of 30%Gantrez® S-97 and 5%HA

Table 31: Independent and dependent variables of MNs in 3^k factorial design of 20%PVA-5%HA

Formulation code	Independent variables (weight ratio)		Dependent variables	
	X_1: 20%PVA	X_2: 5%HA	Y_1: Mechanical strength (N)	Y_2: Needles height (μm)
P-H_MNs 1	1	1	19.20	559.76
P-H_MNs 2	1	3	32.03	540.85
P-H_MNs 3	1	5	36.89	607.51
P-H_MNs 4	3	1	12.81	486.59
P-H_MNs 5	3	3	20.03	548.50
P-H_MNs 6	3	3	25.68	564.79
P-H_MNs 7	3	3	22.99	564.79
P-H_MNs 8	3	3	19.32	590.22
P-H_MNs 9	3	5	33.32	574.14
P-H_MNs 10	5	1	20.94	460.46
P-H_MNs 11	5	3	23.49	447.36
P-H_MNs 12	5	5	29.65	503.48
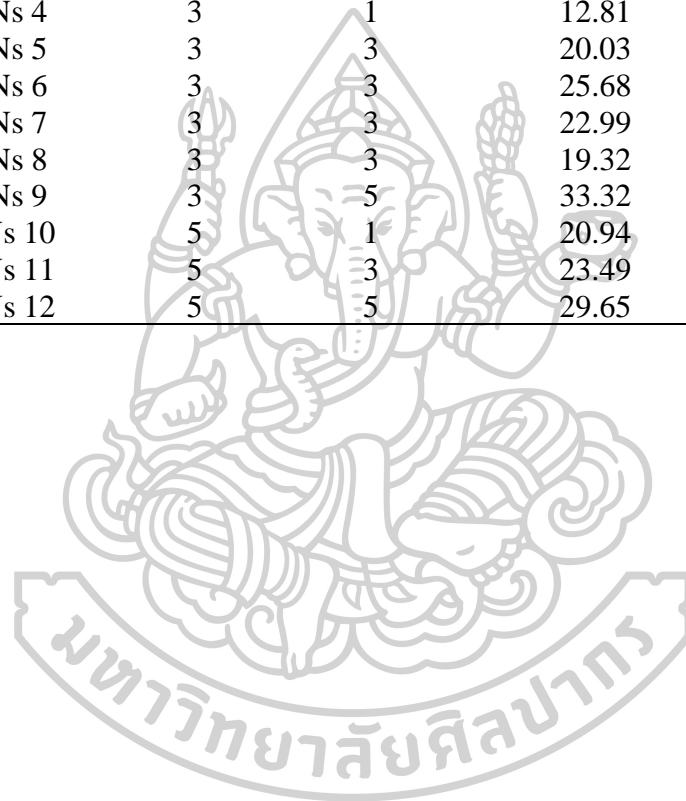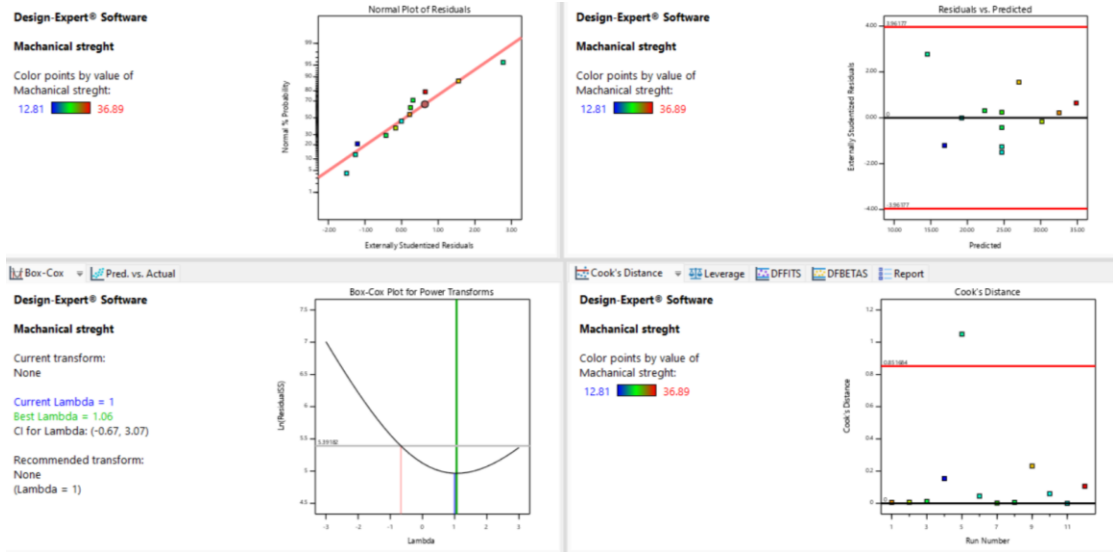
Figure 56: Analysis data of mechanical strength of 20%PVA and 5%HA
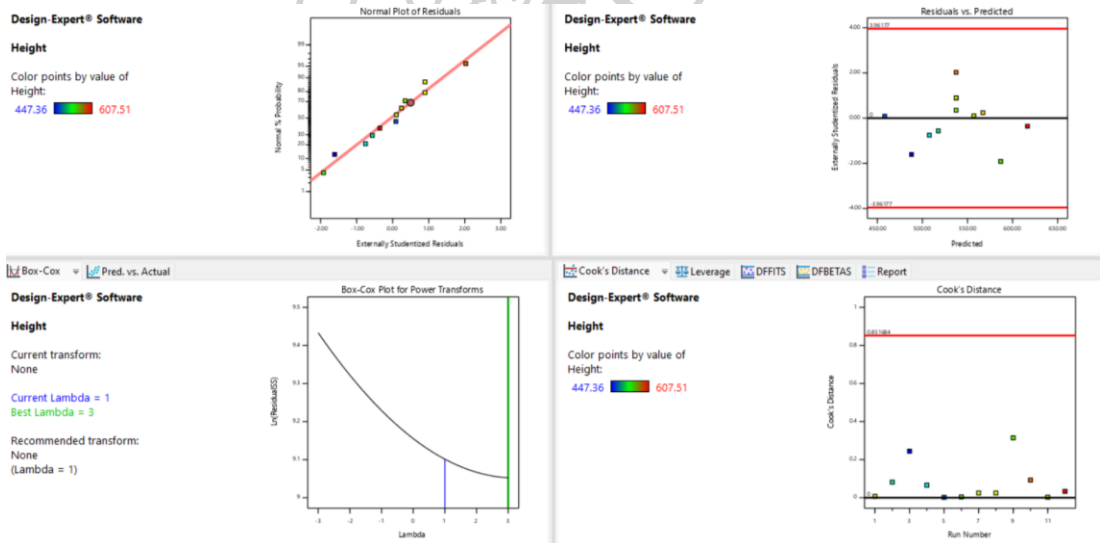
Figure 57: Analysis data of MNs height of 20%PVA and 5%HA
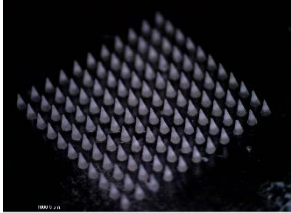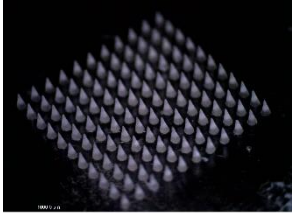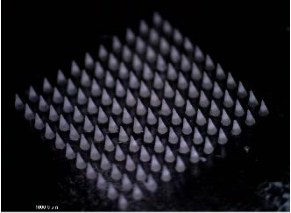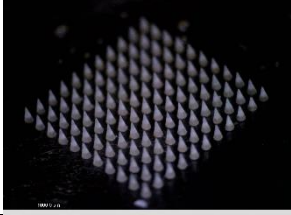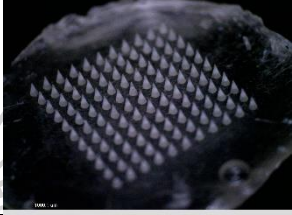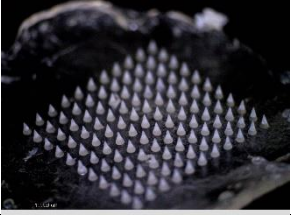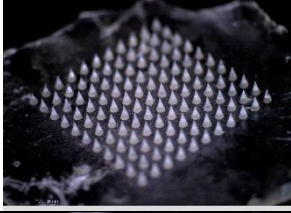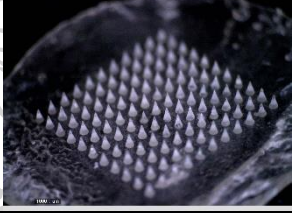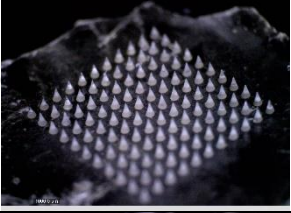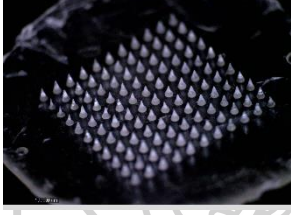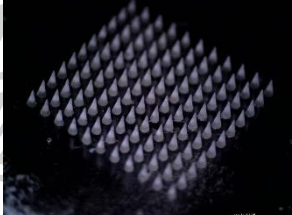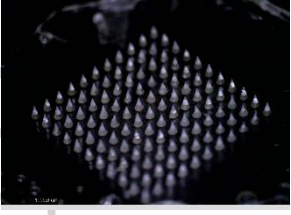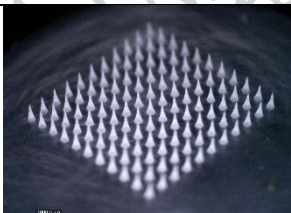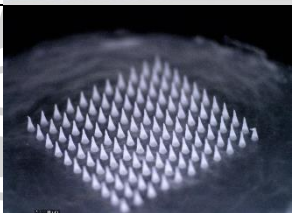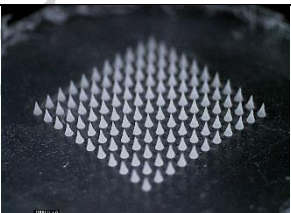
Table 32: The mechanical strength stability of MEs-FLUZ-loaded two-layered dissolving MNs after being stored at 4, 25, and 40 °C for 0, 1, 2, 3, and 6 months. Each value represented the mean ± SD (n=3)

MEs-FLUZ-loaded two-layered dissolving MNs	T (°C)	Mechanical strength (N)
0 month		27.66±1.54
1 month	4	28.96±1.06
	25	25.91±2.02
	40	17.17±0.52
2 months	4	29.07±1.96
	25	26.19±3.53
	40	16.57±2.10
3 months	4	31.83±1.39
	25	27.36±2.30
	40	14.86±1.82
6 months	4	29.17±0.86
	25	27.41±1.75
	40	15.68±1.18

Table 33: The %drug content stability of MEs-FLUZ-loaded two-layered dissolving MNs after being stored at 4, 25, and 40 °C for 0, 1, 2, 3, and 6 months. Each value represented the mean ± SD (n=3)

MEs-FLUZ-loaded two-layered dissolving MNs	T (°C)	%drug contents' stability (%)
0 month		100.00±0.00
1 month	4	96.00±5.16
	25	92.18±10.21
	40	95.99±6.40
2 months	4	99.69±12.70
	25	102.77±11.02
	40	93.58±4.25
3 months	4	94.91±3.40
	25	101.79±12.71
	40	107.07±9.59
6 months	4	99.02±1.71
	25	110.54±10.12
	40	107.24±1.25

Table 34: The physical appearance stability of MEs-FLUZ-loaded two-layered dissolving MNs after being stored at 4, 25, and 40 °C for 0, 1, 2, 3, and 6 months.

Condition	4 °C	25 °C	40 °C
0 month			
1 month			
2 months			
3 months			
6 months			

REFERENCES

1.   Collier S, Gronostaj M, MacGurn A, Cope J, Awsumb K, Yoder J, et al. Estimated Burden of Keratitis - United States, 2010. MMWR Morbidity and mortality weekly report. 2014;63:1027-30.

2.   Thomas PA. Fungal infections of the cornea. Eye. 2003;17(8):852-62.

3.   Thakkar R, Patil A, Mehraj T, Dudhipala N, Majumdar S. Updates in Ocular Antifungal Pharmacotherapy: Formulation and Clinical Perspectives. Current Fungal Infection Reports. 2019;13(2):45-58.

4.   Moustafa MA, Elnaggar YSR, El-Refaie WM, Abdallah OY. Hyalugel-integrated liposomes as a novel ocular nanosized delivery system of fluconazole with promising prolonged effect. Int J Pharm. 2017;534(1-2):14-24.

5.   Fetih G. Fluconazole-loaded niosomal gels as a topical ocular drug delivery system for corneal fungal infections. Journal of Drug Delivery Science and Technology. 2016;35:8-15.

6.   Pathak MK, Chhabra G, Pathak K. Design and development of a novel pH triggered nanoemulsified in-situ ophthalmic gel of fluconazole: Ex-vivo transcorneal permeation, corneal toxicity and irritation testing. Drug Development and Industrial Pharmacy. 2013;39:780 - 90.

7.   You X, Li J, Li S, Shi W. Effects of Lamellar Keratectomy and Intrastromal Injection of 0.2% Fluconazole on Fungal Keratitis. Journal of ophthalmology. 2015;2015:656027.

8.   Mahdy RA, Nada WM, Wageh MM. Topical amphotericin B and subconjunctival injection of fluconazole (combination therapy) versus topical amphotericin B (monotherapy) in treatment of keratomycosis. J Ocul Pharmacol Ther. 2010;26(3):281-5.

9.   ElMeshad AN, Mohsen AM. Enhanced corneal permeation and

antimycotic activity of itraconazole against Candida albicans via a novel nanosystem vesicle. Drug Deliv. 2016;23(7):2115-23.

10.   Mannermaa E, Vellonen KS, Urtti A. Drug transport in corneal epithelium and blood-retina barrier: emerging role of transporters in ocular pharmacokinetics. Adv Drug Deliv Rev. 2006;58(11):1136-63.

11.   Järvinen K, Järvinen T, Urtti A. Ocular absorption following topical delivery. Advanced Drug Delivery Reviews. 1995;16(1):3-19.

12.   Gaudana R, Jwala J, Boddu SH, Mitra AK. Recent perspectives in ocular drug delivery. Pharm Res. 2009;26(5):1197-216.

13.   Lang JC. Ocular drug delivery conventional ocular formulations. Advanced Drug Delivery Reviews. 1995;16(1):39-43.

14.   Soliman OAE, Mohamed EA, Khatera NAA. Enhanced ocular bioavailability of fluconazole from niosomal gels and microemulsions: formulation, optimization, and in vitro-in vivo evaluation. Pharm Dev Technol. 2019;24(1):48-62.

15.   Elkasabgy NA. Ocular supersaturated self-nanoemulsifying drug delivery systems (S-SNEDDS) to enhance econazole nitrate bioavailability. Int J Pharm. 2014;460(1-2):33-44.

16.   Hegde RR, Bhattacharya SS, Verma A, Ghosh A. Physicochemical and pharmacological investigation of water/oil microemulsion of non-selective beta blocker for treatment of glaucoma. Curr Eye Res. 2014;39(2):155-63.

17.   Kumar R, Sinha VR. Preparation and optimization of voriconazole microemulsion for ocular delivery. Colloids Surf B Biointerfaces. 2014;117:82-8.

18.   Silva-Cunha A, da Silva GR, de Castro WV, Fialho SL. Evaluation of the pharmacokinetics and ocular tolerance of a microemulsion containing tacrolimus. J Ocul Pharmacol Ther. 2014;30(1):59-65.

19.   Tiwari R, Dubey V, Kesavan K. Ocular Self-Microemulsifying Drug

Delivery System of Prednisolone Improves Therapeutic Effectiveness in the Treatment of Experimental Uveitis. Ocul Immunol Inflamm. 2019;27(2):303-11.

20.   Üstündag-Okur N, Gökçe EH, Eğrilmez S, Özer Ö, Ertan G. Novel ofloxacin-loaded microemulsion formulations for ocular delivery. J Ocul Pharmacol Ther. 2014;30(4):319-32.

21.   Abser N. Solid Silicon Microneedles for Safe and Effective Drug Delivery to Human Eye. Journal of Electrical Engineering-elektrotechnicky Casopis. 2011;36:28-34.

22.   Jiang J, Gill HS, Ghate D, McCarey BE, Patel SR, Edelhauser HF, et al. Coated microneedles for drug delivery to the eye. Invest Ophthalmol Vis Sci. 2007;48(9):4038-43.

23.   Patel SR, Berezovsky DE, McCarey BE, Zarnitsyn V, Edelhauser HF, Prausnitz MR. Targeted administration into the suprachoroidal space using a microneedle for drug delivery to the posterior segment of the eye. Invest Ophthalmol Vis Sci. 2012;53(8):4433-41.

24.   Suriyaamporn P, Opanasopit P, Ngawhirunpat T, Rangsimawong W. Computer-aided rational design for optimally Gantrez® S-97 and hyaluronic acid-based dissolving microneedles as a potential ocular delivery system. Journal of Drug Delivery Science and Technology. 2021;61:102319.

25.   Amer M, Chen R. Hydrogel-Forming Microneedle Arrays for Sustained and Controlled Ocular Drug Delivery. Journal of Engineering and Science in Medical Diagnostics and Therapy. 2020;3.

26.   Roy G, Galigama RD, Thorat VS, Mallela LS, Roy S, Garg P, et al. Amphotericin B containing microneedle ocular patch for effective treatment of fungal keratitis. Int J Pharm. 2019;572:118808.

27.   Ramalheiro A, Paris JL, Silva BFB, Pires LR. Rapidly dissolving microneedles for the delivery of cubosome-like liquid crystalline nanoparticles with

sustained release of rapamycin. International Journal of Pharmaceutics. 2020;591:119942.

28.   Abdelghany S, Tekko IA, Vora L, Larrañeta E, Permana AD, Donnelly RF. Nanosuspension-Based Dissolving Microneedle Arrays for Intradermal Delivery of Curcumin. Pharmaceutics. 2019;11(7).

29.   Permana AD, Paredes AJ, Volpe-Zanutto F, Anjani QK, Utomo E, Donnelly RF. Dissolving microneedle-mediated dermal delivery of itraconazole nanocrystals for improved treatment of cutaneous candidiasis. European Journal of Pharmaceutics and Biopharmaceutics. 2020;154:50-61.

30.   Olver J, Cassidy L, Jutley G, Crawley L. Ophthalmology at a Glance2014.

31.   Thakur Singh RR, Tekko I, McAvoy K, McMillan H, Jones D, Donnelly RF. Minimally invasive microneedles for ocular drug delivery. Expert Opin Drug Deliv. 2017;14(4):525-37.

32.   Hiral J Shah JNS. Nanoparticulate Transscleral Ocular Drug Delivery. Journal of Biomolecular Research & Therapeutics. 2014;03(03).

33.   Ghate D, Edelhauser HF. Ocular drug delivery. Expert Opin Drug Deliv. 2006;3(2):275-87.

34.   Note A. EYE ANATOMY (LABELED) 2018 [Available from: https://www.anatomynote.com/human-anatomy/ophthalmology-eye-anatomy/eye-anatomy-labeled/.

35.   Cholkar K, Dasari SR, Pal D, Mitra AK. 1 - Eye: anatomy, physiology and barriers to drug delivery. In: Mitra AK, editor. Ocular Transporters and Receptors: Woodhead Publishing; 2013. p. 1-36.

36.   Fischbarg J. The Biology of the Eye. Burlington: Elsevier; 2006.

37.   Rowsey TG, Karamichos D. The role of lipids in corneal diseases and

dystrophies: a systematic review. Clinical and Translational Medicine. 2017;6(1):30.

38.   Huang D, Chen YS, Rupenthal ID. Overcoming ocular drug delivery barriers through the use of physical forces. Adv Drug Deliv Rev. 2018;126:96-112.

39.   Liaw J, Rojanasakul Y, Robinson JR. The effect of drug charge type and charge density on corneal transport. International Journal of Pharmaceutics. 1992;88(1):111-24.

40.   Bachman WG, Wilson G. Essential ions for maintenance of the corneal epithelial surface. Invest Ophthalmol Vis Sci. 1985;26(11):1484-8.

41.   Sasaki H, Ichikawa M, Yamamura K, Nishida K, Nakamura J. Ocular membrane permeability of hydrophilic drugs for ocular peptide delivery. J Pharm Pharmacol. 1997;49(2):135-9.

42.   Rabinovich-Guilatt L, Couvreur P, Lambert G, Dubernet C. Cationic vectors in ocular drug delivery. J Drug Target. 2004;12(9-10):623-33.

43.   Malhotra M, Majumdar DK. Permeation through cornea. Indian J Exp Biol. 2001;39(1):11-24.

44.   Pirie A. The biochemistry of the eye. Proc Nutr Soc. 1960;19:73-8.

45.   Olsen TW, Aaberg SY, Geroski DH, Edelhauser HF. Human sclera: thickness and surface area. Am J Ophthalmol. 1998;125(2):237-41.

46.   Boote C, Sigal IA, Grytz R, Hua Y, Nguyen TD, Girard MJA. Scleral structure and biomechanics. Progress in Retinal and Eye Research. 2020;74:100773.

47.   Achouri D, Alhanout K, Piccerelle P, Andrieu V. Recent advances in ocular drug delivery. Drug Dev Ind Pharm. 2013;39(11):1599-617.

48.   Candiello J, Balasubramani M, Schreiber EM, Cole GJ, Mayer U, Halfter W, et al. Biomechanical properties of native basement membranes. Febs j.

2007;274(11):2897-908.

49.   Patil A, Lakhani P, Taskar P, Wu KW, Sweeney C, Avula B, et al. Formulation Development, Optimization, and In Vitro-In Vivo Characterization of Natamycin-Loaded PEGylated Nano-Lipid Carriers for Ocular Applications. J Pharm Sci. 2018;107(8):2160-71.

50.   Tuft SJ, Tullo AB. Fungal keratitis in the United Kingdom 2003-2005. Eye (Lond). 2009;23(6):1308-13.

51.   Chandrasekar P. Management of invasive fungal infections: a role for polyenes. J Antimicrob Chemother. 2011;66(3):457-65.

52.   Reddy PR, Reddy PS, Reddy AR, Saboo NK. A comparative evaluation of Nystatin, Amphotericin-B and Miconazole in keratomycosis. Indian J Ophthalmol. 1982;30(4):249-50.

53.   Lombardi A, Ouanounou A. Fungal infections in dentistry: Clinical presentations, diagnosis, and treatment alternatives. Oral Surg Oral Med Oral Pathol Oral Radiol. 2020;130(5):533-46.

54.   O'Day DM, Head WS, Robinson RD, Clanton JA. Corneal penetration of topical amphotericin B and natamycin. Curr Eye Res. 1986;5(11):877-82.

55.   Goldblum D, Rohrer K, Frueh BE, Theurillat R, Thormann W, Zimmerli S. Ocular distribution of intravenously administered lipid formulations of amphotericin B in a rabbit model. Antimicrob Agents Chemother. 2002;46(12):3719-23.

56.   Méndez J, Herrera ML. Métodos de susceptibilidad antifúngica: revisión metodológica. Revista Médica del Hospital Nacional de Niños Dr Carlos Sáenz Herrera. 2001;36:37-44.

57.   O'Day DM, Foulds G, Williams TE, Robinson RD, Allen RH, Head WS. Ocular uptake of fluconazole following oral administration. Arch Ophthalmol. 1990;108(7):1006-8.

58.   Mahdy RA, Nada WM, Wageh MM, Kader MA, Saleh MM, Alswad MM. Assessment safety and efficacy of a combination therapy of topical amphotericin B and subconjunctival fluconazole for the treatment of fungal keratitis. Cutan Ocul Toxicol. 2010;29(3):193-7.

59.   Peyton L, Gallagher S, Hashemzadeh M. Triazole antifungals: A review. Drugs of today (Barcelona, Spain : 1998). 2015;51:705-18.

60.   Patil A, Majumdar S. Echinocandins in Ocular Therapeutics. J Ocul Pharmacol Ther. 2017;33(5):340-52.

61.   Agarwal PK, Roy P, Das A, Banerjee A, Maity PK, Banerjee AR. Efficacy of topical and systemic itraconazole as a broad-spectrum antifungal agent in mycotic corneal ulcer. A preliminary study. Indian J Ophthalmol. 2001;49(3):173-6.

62.   Lei G, Dan H, Jinhua L, Wei Y, Song G, Li W. Berberine and Itraconazole Are not Synergistic in Vitro against Aspergillus fumigatus Isolated from Clinical Patients. Molecules (Basel, Switzerland). 2011;16:9218-33.

63.   Al-Badriyeh D, Neoh CF, Stewart K, Kong DC. Clinical utility of voriconazole eye drops in ophthalmic fungal keratitis. Clin Ophthalmol. 2010;4:391-405.

64.   Thiel MA, Zinkernagel AS, Burhenne J, Kaufmann C, Haefeli WE. Voriconazole concentration in human aqueous humor and plasma during topical or combined topical and systemic administration for fungal keratitis. Antimicrob Agents Chemother. 2007;51(1):239-44.

65.   Al-badriyeh D, Neoh C, Stewart K, Kong D. Clinical utility of voriconazole eye drops in ophthalmic fungal keratitis. Clinical ophthalmology (Auckland, NZ). 2010;4:391-405.

66.   Torres HA, Hachem RY, Chemaly RF, Kontoyiannis DP, Raad, II. Posaconazole: a broad-spectrum triazole antifungal. Lancet Infect Dis. 2005;5(12):775-

85.

67.   Cuenca-Estrella M, Gomez-Lopez A, Mellado E, Buitrago MJ, Monzon A, Rodriguez-Tudela JL. Head-to-head comparison of the activities of currently available antifungal agents against 3,378 Spanish clinical isolates of yeasts and filamentous fungi. Antimicrob Agents Chemother. 2006;50(3):917-21.

68.   Soysal A. Prevention of invasive fungal infections in immunocompromised patients: The role of delayed-release posaconazole. Infection and drug resistance. 2015;8:321-31.

69.   Turner MS, Drew RH, Perfect JR. Emerging echinocandins for treatment of invasive fungal infections. Expert Opin Emerg Drugs. 2006;11(2):231-50.

70.   Goldblum D, Frueh BE, Sarra GM, Katsoulis K, Zimmerli S. Topical caspofungin for treatment of keratitis caused by Candida albicans in a rabbit model. Antimicrob Agents Chemother. 2005;49(4):1359-63.

71.   Mojumder DK, Concepcion FA, Patel SK, Barkmeier AJ, Carvounis PE, Wilson JH, et al. Evaluating retinal toxicity of intravitreal caspofungin in the mouse eye. Invest Ophthalmol Vis Sci. 2010;51(11):5796-803.

72.   Letscher V, Herbrecht R. Caspofungin: The first representative of a new antifungal class. The Journal of antimicrobial chemotherapy. 2003;51:513-21.

73.   Yanni S, Augustijns P, Benjamin D, Brouwer K, Annaert P. In Vitro Investigation of the Hepatobiliary Disposition Mechanisms of the Antifungal Agent Micafungin in Humans and Rats. Drug metabolism and disposition: the biological fate of chemicals. 2010;38:1848-56.

74.   Gote V, Sikder S, Sicotte J, Pal D. Ocular Drug Delivery: Present Innovations and Future Challenges. Journal of Pharmacology and Experimental Therapeutics. 2019;370(3):602.

75.   Patel A, Cholkar K, Agrahari V, Mitra AK. Ocular drug delivery

systems: An overview. World J Pharmacol. 2013;2(2):47-64.

76.   Gupta H, Aqil M. Contact lenses in ocular therapeutics. Drug Discov Today. 2012;17(9-10):522-7.

77.   Kim J, Chauhan A. Dexamethasone transport and ocular delivery from poly(hydroxyethyl methacrylate) gels. Int J Pharm. 2008;353(1-2):205-22.

78.   Bourges JL, Bloquel C, Thomas A, Froussart F, Bochot A, Azan F, et al. Intraocular implants for extended drug delivery: therapeutic applications. Adv Drug Deliv Rev. 2006;58(11):1182-202.

79.   Del Amo EM, Urtti A. Current and future ophthalmic drug delivery systems. A shift to the posterior segment. Drug Discov Today. 2008;13(3-4):135-43.

80.   Hughes PM, Olejnik O, Chang-Lin JE, Wilson CG. Topical and systemic drug delivery to the posterior segments. Adv Drug Deliv Rev. 2005;57(14):2010-32.

81.   Yasin MN, Thakur SS, Rupenthal ID. Penetration Routes to Retina and Posterior Segment. Drug Delivery for the Retina and Posterior Segment Disease: Springer Cham; 2018. p. 69-81.

82.   Sugibayashi K, editor Skin Permeation and Disposition of Therapeutic and Cosmeceutical Compounds. Springer Japan; 2017.

83.   Watkinson AC, Brain KR. BASIC MATHEMATICAL PRINCIPLES IN SKIN PERMEATION. Journal of Toxicology: Cutaneous and Ocular Toxicology. 2002;21(4):371-402.

84.   Mitragotri S, Anissimov YG, Bunge AL, Frasch HF, Guy RH, Hadgraft J, et al. Mathematical models of skin permeability: an overview. Int J Pharm. 2011;418(1):115-29.

85.   Hoar TP, Schulman JH. Transparent Water-in-Oil Dispersions: the Oleopathic Hydro-Micelle. Nature. 1943;152(3847):102-3.

86.   Vandamme TF. Microemulsions as ocular drug delivery systems: recent developments and future challenges. Prog Retin Eye Res. 2002;21(1):15-34.

87.   Lawrence MJ, Rees GD. Microemulsion-based media as novel drug delivery systems. Adv Drug Deliv Rev. 2000;45(1):89-121.

88.   Üstündağ Okur N, Çağlar E, Siafaka PI. Novel Ocular Drug Delivery Systems: An Update on Microemulsions. J Ocul Pharmacol Ther. 2020;36(6):342-54.

89.   Du X, Lucia LA, Ghiladi RA. A Novel Approach for Rapid Preparation of Monophasic Microemulsions That Facilitates Penetration of Woody Biomass. ACS Sustainable Chemistry & Engineering. 2016;4(3):1665-72.

90.   Ita K. Microemulsions. Transdermal Drug Delivery2020. p. 97-122.

91.   Talegaonkar S, Azeem A, Ahmad FJ, Khar RK, Pathan SA, Khan ZI. Microemulsions: a novel approach to enhanced drug delivery. Recent Pat Drug Deliv Formul. 2008;2(3):238-57.

92.   Kale SN, Deore SL. Emulsion Micro Emulsion and Nano Emulsion: A Review. Systematic Reviews in Pharmacy. 2016;8(1):39-47.

93.   Singh K, Iqubal MK, Shukla VK, Shuaib M. Review Article Microemulsions: Current Trends in Novel Drug Delivery Systems. 2014;1:39-5139.

94.   Ghosh PK, Murthy RS. Microemulsions: a potential drug delivery system. Curr Drug Deliv. 2006;3(2):167-80.

95.   Aboofazeli R, Patel N, Thomas M, Lawrence MJ. Investigations into the formation and characterization of phospholipid microemulsions. IV. Pseudo-ternary phase diagrams of systems containing water-lecithin-alcohol and oil; The influence of oil. International Journal of Pharmaceutics. 1995;125(1):107-16.

96.   Lawrence MJ. Surfactant systems: microemulsions and vesicles as vehicles for drug delivery. Eur J Drug Metab Pharmacokinet. 1994;19(3):257-69.

97.   Shinoda K, Lindman B. Organized surfactant systems: microemulsions. Langmuir. 1987;3(2):135-49.

98.   Tenjarla S. Microemulsions: an overview and pharmaceutical applications. Crit Rev Ther Drug Carrier Syst. 1999;16(5):461-521.

99.   Pape WJ, Pfannenbecker U, Argembeaux H, Bracher M, Esdaile DJ, Hagino S, et al. COLIPA validation project on in vitro eye irritation tests for cosmetic ingredients and finished products (phase I): the red blood cell test for the estimation of acute eye irritation potentials. Present status. Toxicol In Vitro. 1999;13(2):343-54.

100.   Azad S, Nagul M, Chinna B, Ravi K, Vasu N. Micro Emulsions: An Overview And Pharmaceutical Applications. World Journal of Current Medical and Pharmaceutical Research. 2020;2(2):201-5.

101.   Ruth HS, Attwood D, Ktistis G, Taylor CJ. Phase studies and particle size analysis of oil-in-water phospholipid microemulsions. International Journal of Pharmaceutics. 1995;116:253-61.

102.   Schuerer N, Stein E, Inic-Kanada A, Pucher M, Hohenadl C, Bintner N, et al. Implications for Ophthalmic Formulations: Ocular Buffers Show Varied Cytotoxic Impact on Human Corneal-Limbal and Human Conjunctival Epithelial Cells. Cornea. 2017;36(6):712-8.

103.   Shafiq-un-Nabi S, Shakeel F, Talegaonkar S, Ali J, Baboota S, Ahuja A, et al. Formulation development and optimization using nanoemulsion technique: a technical note. AAPS PharmSciTech. 2007;8(2):E12-28.

104.   Hegde RR, Verma A, Ghosh A. Microemulsion: new insights into the ocular drug delivery. ISRN Pharm. 2013;2013:826798.

105.   Mehta SK, Kaur G. Microemulsions as carriers for therapeutic molecules. Recent Pat Drug Deliv Formul. 2010;4(1):35-48.

106.   Acharya DP, Hartley PG. Progress in microemulsion characterization.

Current Opinion in Colloid & Interface Science. 2012;17(5):274-80.

107. Gradzielski M. Recent developments in the characterisation of microemulsions. Current Opinion in Colloid & Interface Science. 2008;13:263-9.

108. Üstündağ Okur N, Çağlar E, Pekcan A, Okur M, Ayla S. Preparation, optimization and in vivo anti-inflammatory evaluation of hydroquinone loaded microemulsion formulations for melasma treatment. 2019;23:662-70.

109. Rhee YS, Choi JG, Park ES, Chi SC. Transdermal delivery of ketoprofen using microemulsions. Int J Pharm. 2001;228(1-2):161-70.

110. Urtti A. Challenges and obstacles of ocular pharmacokinetics and drug delivery. Adv Drug Deliv Rev. 2006;58(11):1131-5.

111. Richman JB, Tang-Liu DD. A corneal perfusion device for estimating ocular bioavailability in vitro. J Pharm Sci. 1990;79(2):153-7.

112. Kalia YN, Naik A, Garrison J, Guy RH. Iontophoretic drug delivery. Advanced drug delivery reviews. 2004;56 5:619-58.

113. Marro D, Kalia YN, Begoña Delgado-Charro M, Guy RH. Contributions of Electromigration and Electroosmosis to Iontophoretic Drug Delivery. Pharmaceutical Research. 2004;18:1701-8.

114. Suen W-LL, Jiang J, Wong HS, Qu JY, Chau Y. Examination of Effects of Low-Frequency Ultrasound on Scleral Permeability and Collagen Network. Ultrasound in medicine & biology. 2016;42 11:2650-61.

115. Albadr AA, Tekko IA, Vora LK, Ali AA, Laverty G, Donnelly RF, et al. Rapidly dissolving microneedle patch of amphotericin B for intracorneal fungal infections. Drug Deliv Transl Res. 2021;12(4):931-43.

116. Kim YC, Grossniklaus HE, Edelhauser HF, Prausnitz MR. Intrastromal delivery of bevacizumab using microneedles to treat corneal neovascularization. Invest

Ophthalmol Vis Sci. 2014;55(11):7376-86.

117.   Bhatnagar S, Saju A, Cheerla KD, Gade SK, Garg P, Venuganti VVK. Corneal delivery of besifloxacin using rapidly dissolving polymeric microneedles. Drug Deliv Transl Res. 2018;8(3):473-83.

118.   Than A, Liu C, Chang H, Duong PK, Cheung CMG, Xu C, et al. Self-implantable double-layered micro-drug-reservoirs for efficient and controlled ocular drug delivery. Nat Commun. 2018;9(1):4433.

119.   Roy G, Galigama RD, Thorat VS, Garg P, Venuganti VVK. Microneedle ocular patch: fabrication, characterization, and ex-vivo evaluation using pilocarpine as model drug. Drug Dev Ind Pharm. 2020;46(7):1114-22.

120.   Palakurthi NK, Correa ZM, Augsburger JJ, Banerjee RK. Toxicity of a biodegradable microneedle implant loaded with methotrexate as a sustained release device in normal rabbit eye: a pilot study. J Ocul Pharmacol Ther. 2011;27(2):151-6.

121.   Gilger BC, Abarca EM, Salmon JH, Patel S. Treatment of acute posterior uveitis in a porcine model by injection of triamcinolone acetonide into the suprachoroidal space using microneedles. Invest Ophthalmol Vis Sci. 2013;54(4):2483-92.

122.   Roy G, Garg P, Venuganti VV. Microneedle scleral patch for minimally invasive delivery of triamcinolone to the posterior segment of eye. International Journal of Pharmaceutics. 2021:121305.

123.   Song HB, Lee KJ, Seo IH, Lee JY, Lee SM, Kim JH, et al. Impact insertion of transfer-molded microneedle for localized and minimally invasive ocular drug delivery. J Control Release. 2015;209:272-9.

124.   Kim YC, Edelhauser HF, Prausnitz MR. Targeted delivery of antiglaucoma drugs to the supraciliary space using microneedles. Invest Ophthalmol Vis Sci. 2014;55(11):7387-97.

125.   Guillot AJ, Cordeiro AS, Donnelly RF, Montesinos MC, Garrigues TM, Melero A. Microneedle-Based Delivery: An Overview of Current Applications and Trends. Pharmaceutics. 2020;12(6).

126.   Ahmed Saeed Al-Japairai K, Mahmood S, Hamed Almurisi S, Reddy Venugopal J, Rebhi Hilles A, Azmana M, et al. Current trends in polymer microneedle for transdermal drug delivery. International Journal of Pharmaceutics. 2020;587:119673.

127.   Lee KJ, Jeong SS, Roh DH, Kim DY, Choi H-K, Lee EH. A practical guide to the development of microneedle systems – In clinical trials or on the market. International Journal of Pharmaceutics. 2020;573:118778.

128.   Thakur RR, Fallows SJ, McMillan HL, Donnelly RF, Jones DS. Microneedle-mediated intrascleral delivery of in situ forming thermoresponsive implants for sustained ocular drug delivery. J Pharm Pharmacol. 2014;66(4):584-95.

129.   Kim YC, Grossniklaus HE, Edelhauser HF, Prausnitz MR. Intrastromal delivery of bevacizumab using microneedles to treat corneal neovascularization. Investigative ophthalmology & visual science. 2014;55(11):7376-86.

130.   Jiang J, Moore JS, Edelhauser HF, Prausnitz MR. Intrascleral drug delivery to the eye using hollow microneedles. Pharm Res. 2009;26(2):395-403.

131.   Patel SR, Lin AS, Edelhauser HF, Prausnitz MR. Suprachoroidal drug delivery to the back of the eye using hollow microneedles. Pharm Res. 2011;28(1):166-76.

132.   Thakur RR, Tekko IA, Al-Shammari F, Ali AA, McCarthy H, Donnelly RF. Rapidly dissolving polymeric microneedles for minimally invasive intraocular drug delivery. Drug Deliv Transl Res. 2016;6(6):800-15.

133.   Donnelly RF, Singh TRR, Garland MJ, Migalska K, Majithiya R, McCrudden CM, et al. Hydrogel-Forming Microneedle Arrays for Enhanced

Transdermal Drug Delivery. Adv Funct Mater. 2012;22(23):4879-90.

134.   Amer M, Chen RK. Hydrogel-Forming Microneedle Arrays for Sustained and Controlled Ocular Drug Delivery. Journal of Engineering and Science in Medical Diagnostics and Therapy. 2020;3(4).

135.   Li J, Liu B, Zhou Y, Chen Z, Jiang L, Yuan W, et al. Fabrication of a Ti porous microneedle array by metal injection molding for transdermal drug delivery. PLoS One. 2017;12(2):e0172043.

136.   Li J, Zhou Y, Yang J, Ye R, Gao J, Ren L, et al. Fabrication of gradient porous microneedle array by modified hot embossing for transdermal drug delivery. Materials Science and Engineering: C. 2019;96:576-82.

137.   Gholami S, Mohebi M-M, Hajizadeh-Saffar E, Ghanian M-H, Zarkesh I, Baharvand H. Fabrication of microporous inorganic microneedles by centrifugal casting method for transdermal extraction and delivery. International Journal of Pharmaceutics. 2019;558:299-310.

138.   González-Vázquez P, Larrañeta E, McCrudden MTC, Jarrahian C, Rein-Weston A, Quintanar-Solares M, et al. Transdermal delivery of gentamicin using dissolving microneedle arrays for potential treatment of neonatal sepsis. J Control Release. 2017;265:30-40.

139.   Yang J, Liu X, Fu Y, Song Y. Recent advances of microneedles for biomedical applications: drug delivery and beyond. Acta Pharmaceutica Sinica B. 2019;9(3):469-83.

140.   Jamaledin R, Di Natale C, Onesto V, Taraghdari ZB, Zare EN, Makvandi P, et al. Progress in Microneedle-Mediated Protein Delivery. J Clin Med. 2020;9(2).

141.   Vecchione R, Coppola S, Esposito E, Casale C, Vespini V, Grilli S, et al. Electro-Drawn Drug-Loaded Biodegradable Polymer Microneedles as a Viable Route to Hypodermic Injection. Adv Funct Mater. 2014;24.

142.   Johnson A, Procopio A. Low cost additive manufacturing of microneedle masters. 3D Printing in Medicine. 2019;5.

143.   Cordeiro AS, Tekko IA, Jomaa MH, Vora L, McAlister E, Volpe-Zanutto F, et al. Two-Photon Polymerisation 3D Printing of Microneedle Array Templates with Versatile Designs: Application in the Development of Polymeric Drug Delivery Systems. Pharmaceutical Research. 2020;37(9):174.

144.   Bhatnagar S, Gadeela PR, Thathireddy P, Venuganti VVK. Microneedle-based drug delivery: materials of construction. Journal of Chemical Sciences. 2019;131(9).

145.   Gill HS, Prausnitz MR. Coated microneedles for transdermal delivery. J Control Release. 2007;117(2):227-37.

146.   Jiang J, Moore JS, Edelhauser HF, Prausnitz MR. Intrascleral drug delivery to the eye using hollow microneedles. Pharmaceutical research. 2009;26(2):395-403.

147.   Suriyaamporn P, Opanasopit P, Ngawhirunpat T, Rangsimawong W. Computer-aided rational design for optimally Gantrez® S-97 and hyaluronic acid-based dissolving microneedles as a potential ocular delivery system. Journal of Drug Delivery Science and Technology. 2021;61.

148.   Lee Y, Park S, Kim SI, Lee K, Ryu W. Rapidly Detachable Microneedles Using Porous Water-Soluble Layer for Ocular Drug Delivery. Advanced Materials Technologies. 2020;5(5).

149.   Zamboulis A, Nanaki S, Michailidou G, Koumentakou I, Lazaridou M, Ainali NM, et al. Chitosan and its Derivatives for Ocular Delivery Formulations: Recent Advances and Developments. Polymers (Basel). 2020;12(7):1519.

150.   Chen M-C, Ling M-H, Lai K-Y, Pramudityo E. Chitosan Microneedle Patches for Sustained Transdermal Delivery of Macromolecules. Biomacromolecules.

2012;13(12):4022-31.

151.   Sharma S, Hatware K, Bhadane P, Sindhikar S, Mishra DK. Recent advances in microneedle composites for biomedical applications: Advanced drug delivery technologies. Materials Science and Engineering: C. 2019;103:109717.

152.   Dugam S, Tade R, Dhole R, Nangare S. Emerging era of microneedle array for pharmaceutical and biomedical applications: recent advances and toxicological perspectives. Future Journal of Pharmaceutical Sciences. 2021;7(1):19.

153.   Vora LK, Donnelly RF, Larrañeta E, González-Vázquez P, Thakur RRS, Vavia PR. Novel bilayer dissolving microneedle arrays with concentrated PLGA nano-microparticles for targeted intradermal delivery: Proof of concept. J Control Release. 2017;265:93-101.

154.   Cheng Z, Lin H, Wang Z, Yang X, Zhang M, Liu X, et al. Preparation and characterization of dissolving hyaluronic acid composite microneedles loaded micelles for delivery of curcumin. Drug Deliv Transl Res. 2020;10(5):1520-30.

155.   Permana AD, Tekko IA, McCrudden MTC, Anjani QK, Ramadon D, McCarthy HO, et al. Solid lipid nanoparticle-based dissolving microneedles: A promising intradermal lymph targeting drug delivery system with potential for enhanced treatment of lymphatic filariasis. Journal of Controlled Release. 2019;316:34-52.

156.   Zu Q, Yu Y, Bi X, Zhang R, Di L. Microneedle-Assisted Percutaneous Delivery of a Tetramethylpyrazine-Loaded Microemulsion. Molecules. 2017;22(11).

157.   Kelchen MN, Brogden NK. In Vitro Skin Retention and Drug Permeation through Intact and Microneedle Pretreated Skin after Application of Propranolol Loaded Microemulsions. Pharm Res. 2018;35(12):228.

158.   Mojeiko G, de Brito M, Salata GC, Lopes LB. Combination of microneedles and microemulsions to increase celecoxib topical delivery for potential application in chemoprevention of breast cancer. Int J Pharm. 2019;560:365-76.

159.   Gill HS, Prausnitz MR. Does needle size matter? J Diabetes Sci Technol. 2007;1(5):725-9.

160.   Prausnitz MR. Engineering Microneedle Patches for Vaccination and Drug Delivery to Skin. Annu Rev Chem Biomol Eng. 2017;8:177-200.

161.   McCrudden MT, Alkilani AZ, Courtenay AJ, McCrudden CM, McCloskey B, Walker C, et al. Considerations in the sterile manufacture of polymeric microneedle arrays. Drug Deliv Transl Res. 2015;5(1):3-14.

162.   González García LE, MacGregor MN, Visalakshan RM, Ninan N, Cavallaro AA, Trinidad AD, et al. Self-sterilizing antibacterial silver-loaded microneedles. Chem Commun (Camb). 2018;55(2):171-4.

163.   Bezerra MA, Santelli RE, Oliveira EP, Villar LS, Escaleira LA. Response surface methodology (RSM) as a tool for optimization in analytical chemistry. Talanta. 2008;76(5):965-77.

164.   Vera Candioti L, De Zan MM, Cámara MS, Goicoechea HC. Experimental design and multiple response optimization; Using the desirability function in analytical methods development. Talanta. 2014;124:123-38.

165.   S NP, Colombo P, Colombo G, D MR. Design of experiments (DoE) in pharmaceutical development. Drug Dev Ind Pharm. 2017;43(6):889-901.

166.   Fukuda IM, Pinto CFF, Moreira CdS, Saviano AM, Lourenço FR. Design of Experiments (DoE) applied to Pharmaceutical and Analytical Quality by Design (QbD). Brazilian Journal of Pharmaceutical Sciences. 2018;54(spe).

167.   Gorman JW, Hinman JE. Simplex Lattice Designs for Multicomponent Systems. Technometrics. 1962;4(4):463-87.

168.   Patel MM, Patel RJ. Linagliptin loaded Solid-SMEEDS for enhanced solubility and dissolution: Formulation development and optimization by D-optimal design. 2019;9(2):47-56.

169. Danaei M, Dehghankhold M, Ataei S, Hasanzadeh Davarani F, Javanmard R, Dokhani A, et al. Impact of Particle Size and Polydispersity Index on the Clinical Applications of Lipidic Nanocarrier Systems. Pharmaceutics [Internet]. 2018; 10(2).

170. Lim LT, Ah-Kee EY, Collins CE. Common eye drops and their implications for pH measurements in the management of chemical eye injuries. Int J Ophthalmol. 2014;7(6):1067-8.

171. Sanchez I, Martin R, Ussa F, Fernandez-Bueno I. The parameters of the porcine eyeball. Graefes Arch Clin Exp Ophthalmol. 2011;249(4):475-82.

172. Müller GG, Kara-José N, Castro RSd. Antifungals in eye infections: drugs and routes of administration. 2013;72(2):132-41.

173. Hassan HA, Geniady MM, Abdelwahab SF, Abd-Elghany MI, Sarhan HA, Abdelghany AA, et al. Topical Eugenol Successfully Treats Experimental Candida albicans-Induced Keratitis. Ophthalmic Res. 2018;60(2):69-79.

VITA

NAME	Phuvamin Suriyaamporn
DATE OF BIRTH	21 November 1993
PLACE OF BIRTH	Nakhon Pathom
INSTITUTIONS ATTENDED	2018-Present: Doctor of Philosophy, Ph.D. in Pharmaceutical Technology, Faculty of Pharmacy, Silpakorn University, Thailand.
	2012-2018: Bachelor of Pharmacy, (1st class honors), Pharmaceutical Sciences, Faculty of Pharmacy, Ubon Ratchathani University
HOME ADDRESS	22/1 Malaiman road, Sanam Chandra sub-district, Mueang District, Nakhon Pathom 73000 Thailand Tel 082-7876126
PUBLICATION	International publication

1. Suriyaamporn P., Kasemsawat T., Sirilert B., Apiromrak K. Patrojanasophon P., Myat Y.Y., et al. Development and Evaluation of Hydroxypropyl Methylcellulose Patches Containing, Clindamycin for Topical Application. Key Engineering Materials. 2019;819:240-5.

2. Suriyaamporn P., Rangsimawong W., Opanasopit P., Ngawhirunpat T. Development and Characterization of Gantrez® S-97 and Hyaluronic Acid Microneedles for Transdermal Fluorescein Sodium Delivery. Key Engineering Materials. 2020;859:125-31.

3. Suriyaamporn P., Opanasopit P., Ngawhirunpat T., Rangsimawong W. Computer-aided rational design for optimally Gantrez® S-97 and hyaluronic acid-based dissolving microneedles as a potential ocular delivery system Journal of Drug Delivery Science and Technology. 2021;61

4. Tansathien K., Suriyaaumporn P., Charoenputtakhun P., Ngawhirunpat T., Opanasopit P., Rangsimawong W. Development of Sponge Microspicule Cream as a Transdermal Delivery System for Protein and Growth Factors from Deer Antler Velvet Extract. Biol Pharm Bull. 2019;42(7):1207-15.

5. Suriyaamporn P., Sukma M., Rangsimawong W. Design and Investigation of Optimal Dissolving Polymeric Microneedles for Ocular Application by Using Three-Level Factorial Design. Key Engineering Materials. 2022;914:63-8.

6. Aumklad P., Suriyaamporn P., Patrojanasophon P. Formulation and Optimization of Progesterone Microemulsion Using Simplex Lattice Mixture Design. Key Engineering Materials. 2022;914:75-80.

7. Suriyaamporn P., Opanasopit P., Rangsimawong W., Ngawhirunpat T. Optimal Design of Novel Microemulsions-Based Two-Layered Dissolving Microneedles for Delivering Fluconazole in Treatment of Fungal Eye Infection. Pharmaceutics. 2022;14(3):472.

8. Tansathien K., Suriyaamporn P., Ngawhirunpat T., Opanasopit P., Rangsimawong W. A Novel Approach for Skin Regeneration by a Potent Bioactive Placental-Loaded Microneedle Patch: Comparative Study of Deer, Goat, and Porcine Placentas. Pharmaceutics [Internet]. 2022; 14(6).

9. Suriyaamporn P., Opanasopit P., Ngawhirunpat T., Rangsimawong W. Development and evaluation of a fast dissolving effervescent microneedles patch for transdermal application. Science, Engineering and Health Studies, 2022;16: 22050010.

10. Aumklad P., Suriyaamporn P., Sukma M., Akkaramongkolporn P., Nattapulwat N., Opanasopit P. Optimization of Fluorescein Sodium-Loaded Dissolving Microneedles for Ocular Drug Delivery Using a Computational Design Strategy. Advances in Science and Technology. 2022;121:33-8.

Proceeding
1. Suriyaamporn P., Rangsimawong W., Ngawhirunpat T. Development of dissolving polymeric microneedles as an applicator for ocular drug delivery system. International Conference of Pharmaceutical Sciences and Medicines. 2019;17(2): 64-71.

2. Suriyaamporn P., Rangsimawong W., Ngawhirunpat T. Fabrication of dissolvable hyaluronic acid microneedle patches for intraocular fluorescein sodium delivery. The 6th Current Drug Development (CDD) International Conference. 2020.

Academic article
1. Suriyaamporn P., Rangsimawong W., Ngawhirunpat T. Microneedles for ocular drug delivery. Center for continuing Pharmaceutical Education. 2020;859:125-31. ISSD:1006-1000-002-04-2562.

2. Suriyaamporn P., Rangsimawong W., Ngawhirunpat T. Mucoadhesive polymers for ocular drug delivery. Center for continuing Pharmaceutical Education. 2020:859:125-31. ISSD:1006-1-000-003-05-2563.

3. Suriyaamporn P., Rangsimawong W., Ngawhirunpat T. The use of design and analysis of experiments in pharmaceutical products. Center for continuing Pharmaceutical Education. 2022:859:125-31. ISSD: 1006-1-000-003-03-2565.

AWARD RECEIVED   Poster presentation

1. First Place Poster Presentation: Development of dissolving polymeric microneedles as a model ocular drug delivery system, The 6th International Conference on Advanced Pharmaceutical Research (ICAPH 2019) "Sustainable Life through Pharmaceutical Research & Innovation, Rangsit university (28th - 29th March 2019).

2. Best poster presentation award (Gold Medal): Effect of Terpenes on Skin Permeability of Curcumin-liposome loaded Gel Formulation: Natural Penetration Enhancers, The 2nd International Conference on Herbal and Traditional Medicine (HTM2017), Khon Kaen University (25-27 January 2017)